Development of Biomechanical Microtools for Investigating Live Cell Mechanobiology

Jasmine Jin

A thesis submitted in fulfilment of the requirements for the degree of Master of Philosophy

The research reported in this thesis was supported by the award of a Research Training Program scholarship to the MPhil Candidate.

Supervisor:

Prof. Lining (Arnold) Ju

School of Biomedical Engineering

Faculty of Engineering

The University of Sydney

2025

To my foundation – my family and friends

Authorship Attribution Statement

This thesis contains published material in: *Journal of Visualised Experiments*: **Jin Jasmine**, Wang Jerry Haoqing, Chen Catherine Yiyao, Russell Blake, Sun Allan, Wang Yao, Ju Lining Arnold Fluorescence Micropipette Aspiration Assay to Investigate Red Blood Cell Mechanosensing. JoVE (2024). DOI: 10.3791/66265. This publication forms Section 2.5. of "Chapter 2: Literature Review". I am the principal author of the following publication as I performed the major literature research, wrote, formatted and prepared the draft and final manuscript.

This thesis contains published material in: *Biosensors*: Wang Yao, **Jin Jasmine**, Wang Jerry Haoqing, Ju Lining Arnold Acoustic Force-Based Cell-Matrix Avidity Measurement in High Throughput. Biosensors (2023). DOI: https://doi.org/10.3390/bios13010095. This publication forms Section 3.2. of "Chapter 3: Establishing the Acoustics Force-Based Cell Avidity Analyzer". I led and performed the z-Movi experiments and data analysis. I carried out the data interpretation and related results incorporated in the manuscript alongside other co-authors.

In addition to the statements above, in cases where I am not the corresponding author of a published item, permission to include the published material has been granted by the corresponding author.

Student Name: Jasmine Jin

Signature

Date: 11/07/2025

As the supervisor for the candidature upon which this thesis is based, I can confirm that the authorship attribution statements above are correct. In cases where I served as the corresponding author of a published item, permission to include the published material has been granted to Miss Jasmine Jin for her thesis

Supervisor Name: Lining Arnold Ju

Signature

Date: 11/07/2025

Declaration of Originality

I declare that the research detailed in this thesis is original and was independently written and prepared by the author. The following declarations can be affirmed:

- The work presented in this thesis has not been submitted to any other institution for the award of a degree nor used to meet the requirements of any other qualifications.
- All experiments, analysis, and manuscript preparations were conducted and prepared by the author. Refer to Sections 2.5. and 3.1. for details regarding specific contributions in publications.
- This thesis includes experimental data that forms part of a larger research project which is incorporated in unpublished manuscripts. Refer to Sections 3.3. and 4.2. for details regarding specific contributions.
- All externally sourced information and literature have been fully acknowledged through referencing and appropriate citations throughout the thesis.
- All content presented in this thesis was not produced by any generative AI tools and the preparation of this thesis was done by the author.

All experimental data collected for this thesis has been carried out at the Ju Lab — Mechanobiology and Biomechanics Laboratory (MBL) at Building J03 Level 6– School of Biomedical Engineering, University of Sydney.

This declaration is made with the complete understanding of academic integrity policies held by the University of Sydney. Violation of these policies could result in serious disciplinary actions.

Student Name: Jasmine Jin

Signature

Date: 06/05/2025

Acknowledgments

Reaching the end of my Master of Philosophy degree, I write this with the profound realisation that this two-year endeavour has allowed me to uncover my own capabilities. Through the highs and lows of research, I found the strength to persevere, embracing the unknown. Built on a collaborative foundation, the research environment has instilled in me a sense of purpose, propelling my research career forward. I am fortunate to be able to share this experience with the some of the brightest minds at Ju Lab – Mechanobiology and Biomechanics Laboratory (MBL) and the School of Biomedical Engineering, Building J03 Level 6.

First and foremost, I would like to acknowledge my supervisory team, Prof. Lining Arnold Ju and Dr. Yao Wang. Without your mentorship, I would not be where I am today. With your guidance and support, you gave me the opportunity the develop myself as both a researcher and on a personal level. I deeply appreciate your patience as taught me what it means to be a researcher and how to adopt good habits. To highlight, I am most thankful for the consistent transparency you have shown me. The countless discussions about ongoing projects, research directions and even my future, has always provided me immense comfort. I look forward to our future endeavours.

To Ju Lab members, you have all greatly influenced my approach in research. The collective motivation and hard-working nature you all possess has propelled me to be a better researcher. The overall collaborative environment is inspiring, and I am very fortunate to be a part of such a brilliant group. Thank you for helping me finish all the stress baked goodies and celebrating all the wins, small and big.

I want to thank the Ju Lab long-term collaborator Dr Charles Cox lab at the Victor Chang Cardiac Research Institute for developing a supportive and collaborative atmosphere that encourages growth. Your generosity and diligence have provided me better understanding of what research entails and the critical role teamwork plays in successful Piezo1 related cell line regeneration.

To my dear friends - Anna Ong, Cindy Chen, and Elyssa Herzog, I am forever grateful for your presence in my life. Thank you for the endless support and guidance

throughout my research endeavour. Without the endless discussions, riddled with anxiety, about our futures, I would still be left pondering about my career.

Finally, to my beautiful family, thank you for being my foundation. You grounded me when I was unsteady, and you propelled me forward where I got lost. Thank you for being my greatest supporter. I hope I can continue to make you proud.

List of Publications, Presentations and Grants

Publications Arising from this Thesis

Biosensors: Wang Yao, **Jin Jasmine**, Wang Jerry Haoqing, Ju Lining Arnold Acoustic Force-Based Cell-Matrix Avidity Measurement in High Throughput. Biosensors (2023). DOI: https://doi.org/10.3390/bios13010095.

Journal of Visualised Experiments: **Jin Jasmine**, Wang Jerry Haoqing, Chen Catherine Yiyao, Russell Blake, Sun Allan, Wang Yao, Ju Lining Arnold Fluorescence Micropipette Aspiration Assay to Investigate Red Blood Cell Mechanosensing. JoVE (2024). DOI: 10.3791/66265.

Other Publications Related to this Thesis

Nature Communications: Wang Jerry Haoqing, Wang Yao, Mirjavadi Seyed Sajad, Andersen Tomas, Moldovan Laura, Vatankhah Parham, Russell Blake, **Jin Jasmine**, Zhou Zijing, Li Qing, Cox Charles D., Su Qian Peter, Ju Lining Arnold Microscale geometrical modulation of PIEZO1 mediated mechanosensing through cytoskeletal redistribution. Nat Commun (2024). DOI: https://doi.org/10.1038/s41467-024-49833-6

Advanced Materials: Jiang Fengtao, Zhang Yingqi, Fang Guocheng, Wang Yao, Dupuy Alexander, **Jin Jasmine**, Shen Yi, Lim Khoon S, Wang Yinyan, Zhang Yu Shrike, Cho Ann-Na, Lu Hongxu, Ju Lining Arnold Intravasation-On-μDevice (INVADE): Engineering Dynamic Vascular Interfaces to Study Cancer Cell Intravasation. Adv. Mater (2025). DOI: https://doi.org/10.1002/adma.202501466

National and International Conferences

Jin Jasmine, Wang Yao, Wang Haoqing Jerry, Ju Lining Arnold, Cell-Extracellular Matrix Avidity Measurement Using Acoustic Force. The 2023 Single-cell and Spatial Biology Symposium (2023)

Jin Jasmine, Wang Yao, Wang Haoqing Jerry, Ju Lining Arnold, Cell-Extracellular Matrix Avidity Measurement Using Acoustic Force. LUMICKS Visit (2023)

Jin Jasmine, Wang Yao, Ju Lining Arnold, Application of z-Movi and relative data analysis protocol. FEBS Mechanics in Biology: From Molecules to Cells to Tissues (2023)

Jin Jasmine, Sun Allan, Ju Lining Arnold, Application of z-Movi and Acoustic Force Spectroscopy (AFS). Glasgow-Sydney Symposium (2024)

Awards, Grants and Funding Sources

2023 Sydney-Glasgow Ignition Grant (**Student Participation**) A$40,000

2023 Golden Chip Award from LUMICKS representing Ju Lab and USYD BME

Table of Contents

List of Figures

List of Tables

List of Abbreviations

3D	Three-Dimensional
AFS	Acoustic Force Spectroscopy
ANO2	Anoctamin 2
BCMA	B-Cell Maturation Antigen
BFP	Biomembrane Force Probe
Ca	Calcium
CAM	Cell Adhesion Molecule
CAR	Chimeric Antigen Receptor
CD	Cluster of Differentiation
CFM	Centrifuge Force Microscopy
CMF488	CellMask Green 488
CMO55	CellMask Orange
COS	CV-1 Origin Simian
DDR	Discoidin Domain Receptor
DEG	Degenerin
DFS	Dynamic Force Spectroscopy
DMEM	Dulbecco's Modified Eagle Medium
DNA	Deoxyribonucleic Acid
dsDNA	Double-Stranded DNA
ECD	Extracellular Domain
ECM	Extracellular Matrix
EGTA	Ethylene glycol-bis(2-aminoethylether)-N,N,N',N'-tetraacetic acid
ENaC	Epithelial Sodium Channel
ERK	Extracellular Signal-Regulated Kinase
FA	Focal Adhesions
FBS	Foetal Bovine Serum
FDA	Food and Drug Administration
fMPA	Fluorescence Micropipette Aspiration
FN	Fibronectin
FOV	Field of View
$GdCl_3$	Gadolinium Chloride
GsMTx4	Grammostola Mechanotoxin #4
HEK	Human Embryonic Kidney
HER	Human Epidermal Growth Factor Receptor
JFX554	Janelia Fluor®
LINC	Linker of Nucleoskeleton and Cytoskeleton
MAPK	Mitogen-Activated Protein Kinase
MCF-7	Michigan Cancer Foundation-7
MDA-MB	M D Anderson–Metastatic Breast
MT	Magnetic Tweezers
mβCD	Methyl-β-cyclodextrin

NaOH	Sodium Hydroxide
NF-κB	Nuclear Factor Kappa-Light-Chain-Enhancer of Activated B Cells
OT	Optical Tweezers
P1KO	Piezo1 Knockout
P1KO-Mutant-Halo	Piezo1 Knockout-Mutant-Halo
P1OE	Piezo1 Overexpressed-Halo
PBS	Phosphate-Buffered Saline
PCBA	Printed Circuit Board Assembly
PECAM	Platelet Endothelial Cell Adhesion Molecule
Pha488	Phalloidin 488
PLL	Poly-L-Lysine
PS	Penicillin-Streptomycin
RBC	Red Blood Cell
RNA	Ribonucleic Acid
ROI	Region of Interest
scFv	Single Chain Variable Fragment
TAZ	Transcriptional Coactivator with PDZ-Binding Motif
TDMS	Technical Data Management System
TFM	Traction Force Microscopy
TME	Tumour Microenvironment
TRP	Transient Receptor Potential
TRPM4	Transient Receptor Potential Cation Channel Subfamily M member 4
VE	Vascular Endothelial
WLC	Worm-Like Chain
WNT	Wingless-Related Integration Site
WT	Wild Type
YAP	Yes-Associated Protein

Abstract

This thesis investigates the fundamental role of mechanical forces in cellular biology, with a specific focus on the mechanosensitive ion channel Piezo1 in regulating cell-matrix and cell-cell interactions. Using two complementary acoustic force-based platforms—the z-Movi cell avidity analyser and Acoustic Force Spectroscopy (AFS)—this research provides quantitative insights into cellular mechanobiology at both population and single-cell levels. The z-Movi studies for cell-matrix interactions revealed that Piezo1 significantly enhances cell adhesion to fibronectin during the initial attachment phase in both transformed (HEK293T) and tumor (MCF-7) cells, with overexpression enhancing adhesion and knockout or pharmacological inhibition reducing adhesion strength. Additionally, for cell-cell interactions, z-Movi analysis demonstrated the superior binding capacity of CD19-CAR T cells compared to HER2-CAR T cells and validated a novel bispecific adaptor approach to redirect CD19-CAR T cells to target HER2-expressing solid tumours. Further investigations using AFS elucidated Piezo1's critical role in cellular mechanoprotection, showing that beyond its ion channel function, Piezo1 structurally reinforces cell membrane integrity under mechanical stress. This work advances our understanding of mechanobiology in health and disease, offering insights into potential therapeutic strategies targeting mechanical signalling pathways in cancer and immunotherapy applications.

Chapter 1: Introduction

What if the secret to understanding disease wasn't just in our genes, but in the way our cells feel? Beyond the traditional views of cellular processes being dictated by chemical signals and genetic makeup, emerging research has uncovered the remarkable ability of cells to sense and respond to mechanical stimuli within their surrounding microenvironment. This dynamic responsiveness lies within the emerging field of mechanobiology, elucidating the complex interplay between mechanical forces, cell signaling and biological processes [1]. This leads to greater understanding of the influence of mechanical stimuli within cellular processes including cell behaviour, tissue development, and disease [2]. By unravelling the complexities of such cellular processes, a deeper understanding of varying medical diseases such as cancer can be achieved.

Within the context of mechanobiology, cells are continuously exposed to several biomechanical cues within their microenvironment. These biomechanical cues include matrix stiffness, tension, compression, fluid shear stress and surface dynamics [3], [4]. Through the employment of mechanosensors like cell adhesion molecules, cells are able to sense and convert mechanical stimuli into biochemical signals. It is important to note that cells rarely exist in isolation and the capacity for cells to sense and respond to these biomechanical cues are acutely influenced by the cellular communication between surrounding cells and extracellular matrix (ECM) [5]. Cell-cell and cell-matrix interactions establish the junction through which biomechanical signals are transmitted and translated to manipulate cell function and tissue organisation [6], [7]. By comprehending the cellular communication involved within the microenvironment of cells, it provides the avenue to improve current therapeutics for several diseases and disease progressions including tumour metastasis [8], [9], [10], [11].

Elucidated in recent mechanobiology studies focussed on cellular mechanosensing, there are specialised molecular structures that possess the ability to detect and respond to mechanical stimuli in the cellular microenvironment. Piezo1, a mechanosensitive ion channel is a critical example that has been shown to have the capacity to sense and translate mechanical stimuli into key cellular responses. The structure of Piezo1 is that of a large transmembrane protein, configured as a trimeric ion

channel. When the Piezo1 ion channel is activated upon sensing mechanical stimuli such as membrane tension, substrate stiffness and fluid shear stress, the flow of cations, especially calcium ions, in and out of the permeable structure is mediated. The facilitation of calcium influx into the cell is especially critical in triggering downstream signalling pathways which regulate various cellular processes such as cell adhesion, migration and differentiation. Whilst the role of Piezo1 in mechanotransduction has been signified, a comprehensive understanding of Piezo1's capacity in other cellular mechanobiology investigations such as cell-cell and cell-matrix interactions remain to be fully explored.

With an emerging focus endowed upon the field of mechanobiology, there is an increased demand for technology that is capable and effective in applying and measuring forces on cellular and subcellular scales. Several model systems and conventional methods have been developed and employed to study mechanobiology including fixed-cell imaging-based *in vitro* adhesion seeding assays [12], optical tweezers-based traction force microscopy [13], and traditional wash assays [14]. Although instrumental in identifying the key elements of the mechanobiology process, these techniques are often non-standardised and heavily reliant on manual operation, rendering them unsuitable for high-throughput applications patient and large-scale drug stratification [15], [16], [17].

In light of the drawbacks of current technology, this thesis brings forth a novel proposal to overcome these limitations, employing two complementary acoustic-force based platforms – the z-Movi cell avidity analyser and Acoustic Force Spectroscopy (AFS). These platforms facilitate high-throughput measurements of cell-cell and cell-matrix interactions, enabling quantitative investigations on both population and single-cell levels. Specifically, this thesis aims to investigate the role of Piezo1 in cellular mechanobiology in the context of two primary focusses: (1) the influence of Piezo1 on cell-matrix adhesion during the initial attachment phase, and (2) the function of Piezo1 in cellular mechanoprotection beyond its ion channel activity. Furthermore, the wider utility of acoustic force-based technologies in biomedical research and clinical therapy is explored through its use in evaluating the efficacy of chimeric antigen receptor (CAR) T-cell therapies.

This thesis is divided into four aims:

- Aim 1: Detailed in Chapter 3.3, the main objective is to establish the commercialised cell avidity analyser, z-Movi. Designed for immunotherapeutic screening, the z-Movi platform was initially employed to screen for CAR T cells that exhibited the highest killing capacity through correlating the binding avidity to tumour cells expressing the target antigen. In collaboration with the Peter MacCallum Cancer Centre, the efficacy of constructed cluster of differentiation (CD)-19-CAR and human epidermal growth factor receptor 2 (HER2)-CAR T cells were examined through interactions between haematological cancers and breast cancers. Additionally, with the low efficacy rates of CAR T cell therapy on solid tumours, this research explores the potential of a novel adaptor that leverages the CD19 CAR T cells to target solid tumours.
- Aim 2: Following the conventional application of z-Movi, Chapter 3.4. presents the expansion of the z-Movi platform to investigate cell-matrix interactions. This novel approach is motivated by the need to understand the cell adhesion process on the ECM, with particular emphasis on the initial stages of cell adhesion. The assay studies transformed Human Embryonic Kidney (HEK)-293T cell lines expressing different levels of the mechanosensitive ion channel, Piezo1, to explore its role during the initial stages of cell adhesion. Through characterising the impacting of Piezo1 within the initial cell adhesion process, this research can elucidate the fundamental mechanisms involved in mechanobiology at the biomolecular level.

- Aim 3: The focus of Chapter 4.1., is the development and characterisation of an acoustic force spectroscopy (AFS) platform designed for real-time investigation of distinct binding events in living cells under mechanical stimulation. The development of AFS was driven by the limitations held by z-Movi which is AFS-based. To elaborate, the z-Movi was preconfigured to only perform a single force ramp to measure the total binding strength between two subjects. To counter the limitation, AFS was established and optimised to produce a maximum of eight times the acoustic force output with different force modes.

- Aim 4: In conjunction with Aim 3, Chapter 4.2. aims to employ the established AFS to investigate the impact of Piezo1 on membrane integrity. Beyond its traditional role as a mechanosensitive ion channel, it is hypothesised that Piezo1 plays a broader role in cellular mechanotransduction. This work aims to showcase that through the activation of Piezo1, intracellular signalling is initiated, driving integrins into a higher-affinity state which ultimately strengthens ECM interactions. Motivated by the capabilities of Piezo1, these findings present a mechanoprotective pathway with regard to cellular adhesion strengthening.

By integrating advanced biophysical approaches with cellular and molecular analyses, this thesis contributes to our understanding of how cells sense, respond to, and withstand mechanical forces, with potential implications for developing therapeutics that target mechanical signalling pathways in disease.

Chapter 2: Literature Review

2.1. The Importance of Mechanobiology

Mechanobiology is the study of the interactions between mechanical stimuli and cellular biology [1]. The multidisciplinary field elucidates how cells sense, transduce and respond in regard to mechanical stimuli as well as the classification of cellular mechanical properties. Mechanical forces are a crucial factor that dictates cell behaviours and tissues homeostasis[18]. It has been correlated with significant biological events such as stem cell differentiation, cell fate switching and tissue development. All physiological features directly depend on the cells' capacity to sense and respond to mechanical cues [19].

2.1.1. Mechanotransduction

Mechanotransduction is defined to be the fundamental physiological process wherein cells convert mechanical stimuli from their adjacent environments and subsequently translate them into biochemical signals, resulting in specific cellular responses that in turn can promote structural remodelling [3], [4]. This process is also known to facilitate mechanolransduction which refers to the biological process that cells undertake to convert mechanical energy into electrical or chemical signals [20], [21]. There are three main phases within the process of mechanotransduction: mechanocoupling, cell-cell communication and the effector response [3], [22]. Mechanocoupling refers to the initial phase where an applied mechanical stimulus generates a physical perturbation, either directly or indirectly, to the cell [23]. The cell-cell communication phase, also denoted as the signal propagation phase, is the enlistment of cell signalling pathways for biochemical transfiguration and conduction of the transmitted mechanical stimulus between cells [24], [25]. There are several signalling pathways that incorporate a torrent of prospective cytosolic mediators to convey these biochemical signals from the surface of the cell to, ultimately, the effector endpoint [26]. The last phase, the effector response, involves the cellular reaction to the applied mechanical stimulus, that is, where the cellular biology begins to undergo modification. These changes are referred to as the cell's ultimate response to the mechanical cues that were sensed and translated [4], [21]. An example of this would be if the designated

endpoint were the effector cells, the cellular response may lead to changes in the adhesive properties of the cells, cytoskeletal reorganization or even lead to apoptosis, otherwise known as cell death [3].

2.1.2. Biomechanical Cues

In the context of mechanobiology, within the cell microenvironment, cells are constantly exposed to a variety of biomechanical cues that influence cell behaviour [27], [28], [29]. These biomechanical cues are categorised into five key distinct types of physical forces and structural features [10]: ECM stiffness [30], [31], tension (stretching force) [32], [33], compression (pushing force) [34], [35], [36], fluid shear stress [37], [38], and surface topography [39].

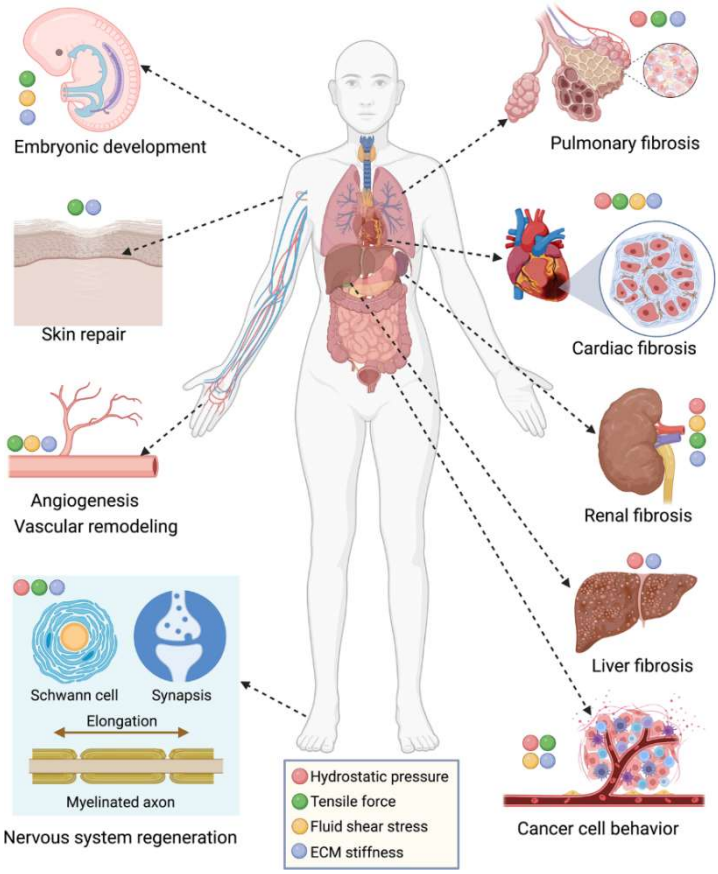

Figure 2.1 Overview of biomechanical cues and associated physiological processes [4].

2.1.2.1. ECM Stiffness

Often denominated by the Young's modulus, stiffness refers to a substrate's threshold to resist elastic deformation under an applied force [1]. ECM stiffness, a critical mechanical cue influencing cell behaviour, is recognized by the cell through integrin-

based focal adhesions. These focal adhesions operate as mechanical nexuses between the ECM and actomyosin cytoskeleton[18]. With stiffer substrates, cells are typically observed to achieve accelerated spreading, leading to the increased development of mature focal adhesions and overall higher traction forces [30], [31]. Due to these chain responses, activation of mechanosensitive pathways, like yes-associated protein (YAP) and the transcriptional coactivator with PDZ-binding motif (TAZ), is possible [5]. These signalling pathways are capable of translocating to the nucleus to dominate the gene expression correlated with cell differentiation and proliferation as well as the production of ECM [40]. In juxtaposition, softer substrates tend to exhibit globular cell morphology and predispose stem cell differentiation down particular lineages.

2.1.2.2. Tension

Tension is generally described as the pulling or stretching force with the capacity to deform cells and tissue [41]. Increased tension can be exhibited by cells through various manners such as cell-cell adhesions, cytoskeletal contractility and communications with the ECM. The employment of tension can incite cytoskeletal remodelling and the orientation of cells, an example being the configuration and differentiation of vascular smooth muscle cells when experiencing cyclic stretching [42], [43]. To note, integrins, involved in cell-ECM junctions, and cadherins, involved in cell-cell junctions, are principal mechanosensors with regard to tension[44].

2.1.2.3. Compression

Categorised as a pushing force, compression condenses the volume of a substrate [34]. Cell surface receptors are employed to sense compressive forces and can result in cell morphology changes, cytoskeletal remodelling and intracellular pressure fluctuations. Pathological modifications in tissues, such as cartilage, can be exhibited with a sustained discharge of compressive mechanical force [45]. Additionally, under static and dynamic floe, compression force can be mediated by cell-cell collisions [36]. Contrary to this, when compression forces are controlled with precision, it can influence tissue growth and homeostasis. Various other mechanosensors that act in response to compressive forces include mechanically-gated ion channels and certain signalling pathways such as the canonical Wingless-related integration site (Wnt) pathway (Wnt/β-catenin) [46].

2.1.2.4. Shear Stress

Shear stress refers to forces that operate in parallel to a surface, resulting in the relative motion of several layers of fluid in the context of cell environment. This biomechanical cue is highly relevant for several physiological processes where cells experience fluid flow, an example being that of endothelial cells that line blood vessels [38]. In response to shear stress, endothelial cells configure in the direction of the fluid flow, resulting in changes to their gene expression profile as well as controlling processes such as vascular reconstruction and inflammation[37]. Mechanosensors for shear stress involve Platelet Endothelial Cell Adhesion Molecule (PECAM)-1, Vascular Endothelial (VE)-cadherin, and mechanically-gated ion channels [47]. Several signalling pathways can be triggered through shear stress such as the Mitogen-Activated Protein Kinase (MAPK)/Extracellular Signal-Regulated Kinase (ERK) and Nuclear Factor kappa-light-chain-enhancer of activated B cells (NF-κB) which influences cell survival and proliferation[48], [49].

2.1.2.5. Topography

Topography, referring to the surface and geometrical dynamics of the ECM or other biological substrates, is a pivotal biomechanical cue that has the potential to dictate cell adhesion, spreading, migration and differentiation [39]. To initiate mechanotransduction pathways alongside cytoskeletal remodelling, mechanosensors like integrin interact with the surface structures of cells [50]. For instance, by linearly arranging nanofibers, it can promote osteogenic differentiation. By sensing the geometry of their microenvironment, especially coalesced with other mechanical cues, it can affect the cells morphology and configuration of focal adhesions [39].

2.1.3. Mechanosensitive Molecular Mechanisms

Mechanosensors are pivotal for cells to sense and translate mechanical stimuli within their microenvironment into biochemical signals. In response to such mechanical stimuli, these sensors exhibit physiological changes, activating downstream signalling pathways.

2.1.3.1. Cell Adhesion Molecules and Associated Complexes

Cell adhesion molecules (CAMs) refer to proteins localised on the surface of the cell that support cell-cell and cell-matrix interactions [51]. Integrins, a key mechanosensor, are transmembrane receptors that bind the ECM to the cytoskeleton and are particularly sensitive to the stiffness and tension of the ECM [52]. The application of force onto integrins can trigger conformational changes, clustering, and the recruitment of signaling biomolecules to focal adhesions[53]. These modifications can consolidate protein-protein interactions (catch bonds), uncover obscure binding sites, or reveal locations for post-translational alterations [53]. Additionally, cadherins are transmembrane proteins that facilitate cell-cell adhesions through adherens junctions [54]. Cadherins are known to operate as a mechanosensor for tension located between cell-cell interactions. Forces applied on cadherins can enhance the linkage between actin and catenins, manipulating cell behaviour [19], [55]. Involved in the cellular response to both external and internal forces, focal adhesions and adherens junctions are multimolecular clusters that composite of several mechanosensor proteins. It is important to note that focal adhesion dynamics is essential for identifying ECM rigidity and dictating cell migration [56], [57].

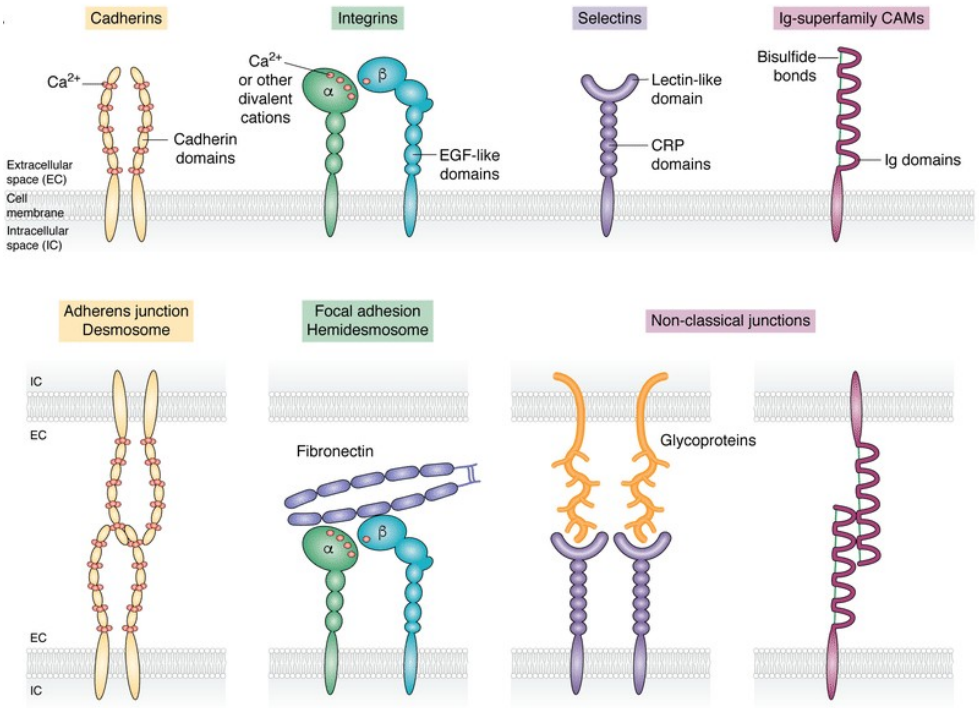

Figure 2.2. Schematic of the structure for four classifications of cell adhesion molecules: Cadherins, Integrins, Selectins and Ig-superfamily CAMs [58].

2.1.3.2. Mechanically-Gated Ion Channels

Mechanosensitive ion channels are transmembrane proteins that produce pores throughout biological membranes. As these channels are force-dependent, their activity fluctuates between open and closed states, where an increase in mechanical stimuli results in the likelihood of the gate opening [20]. Examples of mechanosensitive ion channels include Piezo1 and Piezo2, which are cation channels that are essential for the sensing of mechanical stimuli. Piezo1, regulated by cytoskeletal proteins and the stiffness of the ECM, senses the bilayer tension [59]. Other key mechanosensitive ion channels are the Transient Receptor Potential (TRP) channels, Bacterial channels such as MscL and MscS, and the Epithelial Sodium Channel (ENaC)/Degenerin (DEG) [60].

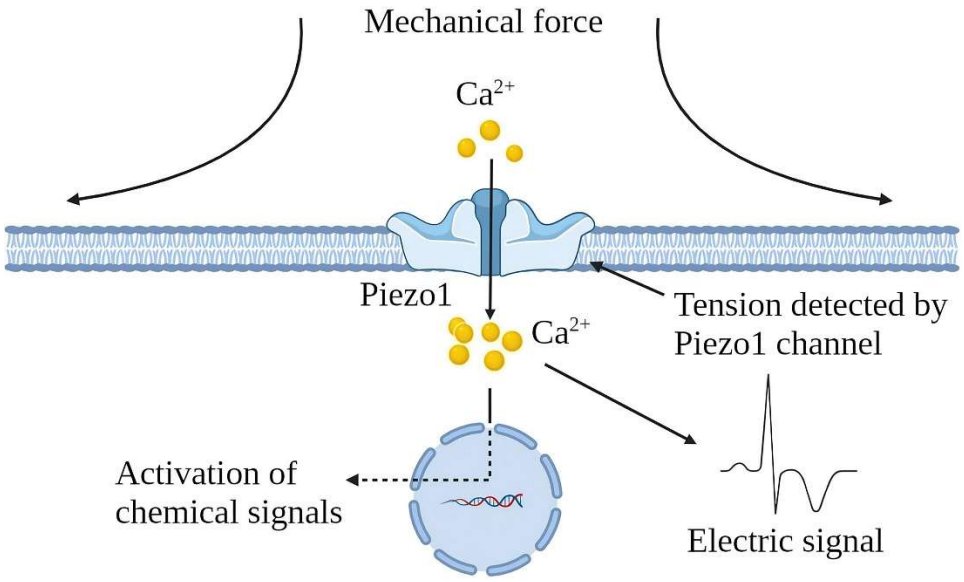

Figure 2.3 Schematic of the mechanosensory function of Piezo1 [61].

There are two main models that theorise the activation of mechanically-gated ion channels: the Tethered Model (force-through-filament) and the Bilayer Model (force-through-lipid) [62]. The Tethered Model proposes that the channel's gate and the proteins localised in the ECM or cytoskeleton are directly linked to each other. To elaborate, if the channel, relative to the proteins, were to be shifted, it would cause the gate to either open or close [63]. For instance, for auditory hair cells, when the stereocilia is displaced, 'tip links' joined to the channel's gate are stretched, causing the gate to open [64]. The Bilayer Model proposes that the tension culminated within the lipid bilayer is inherently accountable for the channel gating. In instances where the membrane tension is increased, resulting in conformational changes within the mechanosensitive ion

channel, the gate can be prompted to open [65]. An example that supports this model would be when purified bacterial mechanosensitive ion channels are reconstructed in a lipid bilayer and can still function as an ion channel, demonstrating that protein linkers are not essential [64].

Table 2-1. Functions of the Mechanically-gated ion channels, Piezo1 and Piezo2, with regard to cellular mechanotransduction [4].

Type	Target	Mechanical stimulation	Mechanism	Reference
Piezo1	Vascular endothelium development	Shear stress	Ca^{2+}influx→MTP-MMP signaling→focal adhesion and endothelial cell sprout formation;	[66]
	Vascular tone	Shear stress	Ca^{2+}influx→G-coupled endothelial adrenomedullin receptor→cAMP→ eNOS→NO; Ca^{2+}influx→ATP→PI3K/AKT→eNOS→NO	[67], [68], [69]
	Vascular remodeling	Stretch	Ca^{2+}influx→transglutaminase →ECM remodeling	[70]
	Erythrocytes	Shear stress	Ca^{2+}influx→K^{+} efflux→red blood cells dehydration	[71]
	Erythrocytes	Shear stress	Ca^{2+}influx→pannexin-1→ATP release	[72]
	Nervous system	Traction force	Ca^{2+}influx→neural differentiation →neuron-astrocyte interaction	[73], [74]
	Gastric mucosa	Antrum distension	Activated G cells→gastrin secretion	[75]
	Lung endothelium	Shear stress	Ca^{2+}influx→calpain→Src cleavage→stabilization of adherens junctions	[76]
	Lung endothelium	Hydrostatic pressure	Ca^{2+}influx→calpain→disruption of adherens junctions	[77]
	Aoveoli	Stretch	Ca^{2+}influx→Bcl-2 pathway→type II epithelial cells apoptosis	[78]
	Urinary bladder	Stretch	Ca^{2+}influx→ATP→attenuate storage disorders	[79]
	Tumor	ECM stiffness	YAP-Piezo1→proliferation; Ca^{2+}influx→AKT/mTOR phosphorylation→proliferation; Piezo1–mitochondrial calcium uniporter–HIF-1α–VEGF axis→metastasis	[80], [81], [82]
Piezo2	Gastrointestinal epithelium	Mucosal force	5-HT pathway→mucosal secretion	[83]
	Airway	Stretch	Ablation of *Piezo2*→Airway-innervating sensory neurons→ respiratory distress and death in newborn mice	[84], [85]
	Urinary bladder	Stretch	Sensory neuron→bladder filling sensation	[86]
Piezo1/2	Baroreceptor reflex	Shear stress	Elevated blood pressure→Piezo1/2 →nodose-petrosal-jugular-ganglion complex→ decreased blood pressure and heart rate	[87], [88], [89]
	Chondrocyte anabolic and biosynthesis	Mechanical stress	GsMTx4→Piezo1/2 inhibition→ alleviate chondrocyte injury	[90], [91]

Acronyms: Calcium ion (Ca^{2+}), matrix metalloproteinase (MMP), microsomal triglyceride transfer protein (MTP), extracellular matrix (ECM), nitric oxide (NO), phosphoinositide 3-kinase (PI3K), protein kinase B (AKT), endothelial nitric oxide synthase (eNOS), adenosine triphosphate (ATP), cyclic adenosine monophosphate (cAMP), transglutaminase (TG), 5-hydroxytryptamine (5-HT), Yes-associated protein (YAP), mechanistic target of rapamycin (mTOR), vascular endothelial growth factor (VEGF), hypoxia-inducible factor 1-alpha (HIF-1α), phosphatidylinositol 3-kinase (PI3K), proto-oncogene tyrosine-protein kinase (Src), Grammostola Mechanotoxin #4 (GsMTx4).

2.1.3.3. Cytoskeleton and Nucleus

The cytoskeleton, composed of a network of protein filaments, plays a significant role in the sending and translating of mechanical cues [92]. Linked to cell adhesion molecules, integrin and cadherin, the cytoskeleton can undergo remodelling due to mechanical forces, modifying the cellular contractility and stiffness. Mechanical stimuli applied to the cytoskeleton can potentially stabilise particular constructs of mechanosensors [93]. Connected to the cytoskeleton through the linker of nucleoskeleton and cytoskeleton (LINC) complexes and nuclear envelope proteins, the nucleus can dictate force transmission. In response to mechanical force, the nucleus can experience deformation which triggers the opening of signalling molecules such as YAP that can alter gene expression [94], [95].

2.1.4. Cell-Matrix Interactions

Cell-ECM interactions refer to the constant communication that occur between cells and ECM proteins. The ECM microenvironment composites of various macromolecules including collagens, elastin, and glycoproteins such as fibronectin and laminins [96]. It supports the cell through mechanical and structural means and controls the cellular phenotype and behaviour. Cell-ECM interactions are formed either by direct or indirect regulation through cell surface receptors [2]. Direct regulation ensues when the ECM interacts with particular cell surface receptors like integrins [4], syndecans [97], CD44 (a receptor for hyaluronan) [98], and the discoidin domain receptor (DDR) group for collagens [99]. Indirect regulation refers to when the ECM is collaborating with multiple receptor molecules as well as growth factors [100]. The physical properties of the ECM can also dictate cell adhesion and mechanotransduction, particularly the elasticity (linear, non-linear, or viscoelastic) and microarchitecture of the ECM [5]. As previously mentioned, when mechanotransduction is initiated by cell-ECM interactions, the ensued effector responses include modifications of the gene expression due to YAP/TAZ activation, the remodelling of the cytoskeleton, cell adhesion, migration, proliferation, differentiation, and apoptosis [101]. For example, as the ECM stiffness is known to regulate cell behaviour and can direct cell differentiation, when cells sense the stiffness of the resident tissue, it is likely for the cells to then differentiate into the resident tissues' cells [34]. Another example would be when cells reorganise the

cytoskeleton, reinforcing stress fibres, within a stiff microenvironment to maintain the tensional equilibrium with the ECM [11], [102].

2.1.5. Cell-Cell Interactions

Cell-cell interactions refer to the physical communication between that of two or more cells. These interactions are mediated by several biomolecules such as proteins, ligands, integrins, and receptors [7]. Cell-cell interactions, crucial for the organisation of cellular activities like tissue assembly, cellular differentiation, and preservation of tissue integrity, can be either structural via cell adhesion molecules or involve biochemical signals to generate an intracellular effect [51]. These interactions can activate downstream signalling in the receiver cells leading to modified transcription factor activity and gene expression [103]. As previously mentioned, cell-cell interactions play a substantial role in the collective cell migration in which cells coordinate their movement, cell proliferation, and apoptosis [104]. For instance, in cardiac tissues, cell-cell interactions conducted through ion channels are crucial when synchronising the tissue contraction [2]. It is also important to note that deviations to cell-cell adhesions can be attributed to the signalling caused by cell-ECM interactions which can facilitate processes like cancer cell invasion [105], [106].

2.2. Dynamic Force Spectroscopy

Dynamic Force Spectroscopy (DFS) techniques are prominently used to investigate molecular interactions between biomolecules through the implementation of force ramps [107]. By evaluating the cellular responses to such mechanical stimuli over time, characterisation and visualisation of mechanical force-dependent adhesion kinetics for individual molecules or molecular assemblies are possible [108]. Alongside these binding kinetics, DFS can be used to investigate the mechanical forces involved during cell rupture and deformation [109]. Studying the interplay of force and biological function is pivotal to further consolidate the comprehension of phenomena such as molecular recognition, protein folding, cellular adhesion, and mechanotransduction.

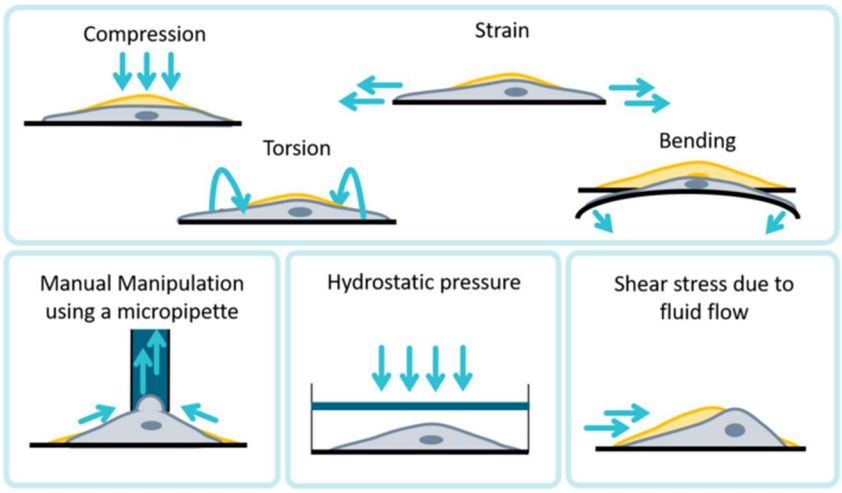

Figure 2.4. Representative image of types of externally applied forces with the corresponding forces [110].

2.2.1. Principles of DFS

Conventionally, DFS executes a force application upon a working system at a molecular level and by reading the relative feedback, precise measurements can be achieved. To elaborate, depending on the type of force, DFS can measure the force required to subsequently break or alter the binding interaction between two biomolecules, such as proteins [111], ligands [112], and nucleic acids (deoxyribonucleic acid (DNA)/ ribonucleic acid (RNA)) [113]. The force protocol that DFS follows can be categorised by several crucial parameters, that is, the ramping of force, rate of force application as well as the direction and form of the force application [114]. Depending on the particular direction of which the force is applied, the behaviour of the molecular interaction can be interpreted.

2.2.1.1. Force Ramp

The most common types of force ramps can be delineated as either linear or exponential [115]. The force ramp is often set as continuous, that is, the applied force will steadily increase until it reaches the predefined event, for example, when a bond rupture occurs.

For a linear force ramp, the applied force increases at a constant rate over time and is more commonly implemented due to the direct relationship between force and

time, enabling more predictable and reliable measurements within the linear region. Mathematically, the linear force ramp $F(t)$ is given by:

$$F(t) = F_0 + k \cdot t$$

where $F(t)$ represents the force applied at time t, F_0 is the initial force, and $\dot{F}$ is the constant increasing rate of force [116].

In scenarios involving rapid force applications to study the biomolecular interaction, an exponential force ramp is more suitable than linear force ramp. Using an exponential force ramp enables a progressively accelerated increase in force over time. Mathematically, the exponential force ramp $F(t)$ is given by:

$$F(t) = F_0 \cdot e^{\alpha t}$$

where $F(t)$ represents the force applied at time t, F_0 is the initial force and α is the exponential growth constant [117].

2.2.1.2. Loading Rate

The loading rate, denoted as $\dot{F}$, refers to the rate at which the force is applied to the molecular system. The loading rate is generally expressed in SI units as pN/s (piconewtons per second), indicating the rate of change in force per unit of time.

Depending on the set loading rate, the rupture force and particular mechanical responses of the cellular interaction can be studied [113]. A high loading rate generates a higher rupture force as the time taken for the molecule or cell to equilibrate during the force application is reduced. In contrast, a low loading rate provides more time for the cell or molecule to adjust, exhibiting a lower rupture force [118]. Kinetic parameters such as the binding and unbinding rates of these cellular interactions depend on the loading rate to determine the rupture process.

2.2.1.3. Direction of Force

The force direction applied to the system has implications on the interaction between the cellular bonds when force is applied as well as the force cessation when the threshold force is attained. Stretching refers to the tensile force that is applied along the

natural elongation axis of the cell or molecule. This configuration allows for the study of protein unfolding, DNA unzipping and bond rupture. In addition, compression, where the force is pushing in the opposing direction, is applied to observe protein folding or molecular assembly processes [119].

2.2.2. Model Systems of DFS

To quantitively analyse the mechanical forces at the single-molecule and single-cell levels, DFS incorporates a suite of sophisticated techniques. To address the inherent heterogeneity tendency of biological systems, various force spectroscopy techniques have been developed and optimised to target either in-depth single-cell investigation or high-throughput parallel analysis. These platforms investigate the fundamental biophysical principles underlying biological processes such as cellular adhesion and mechanotransduction [120].

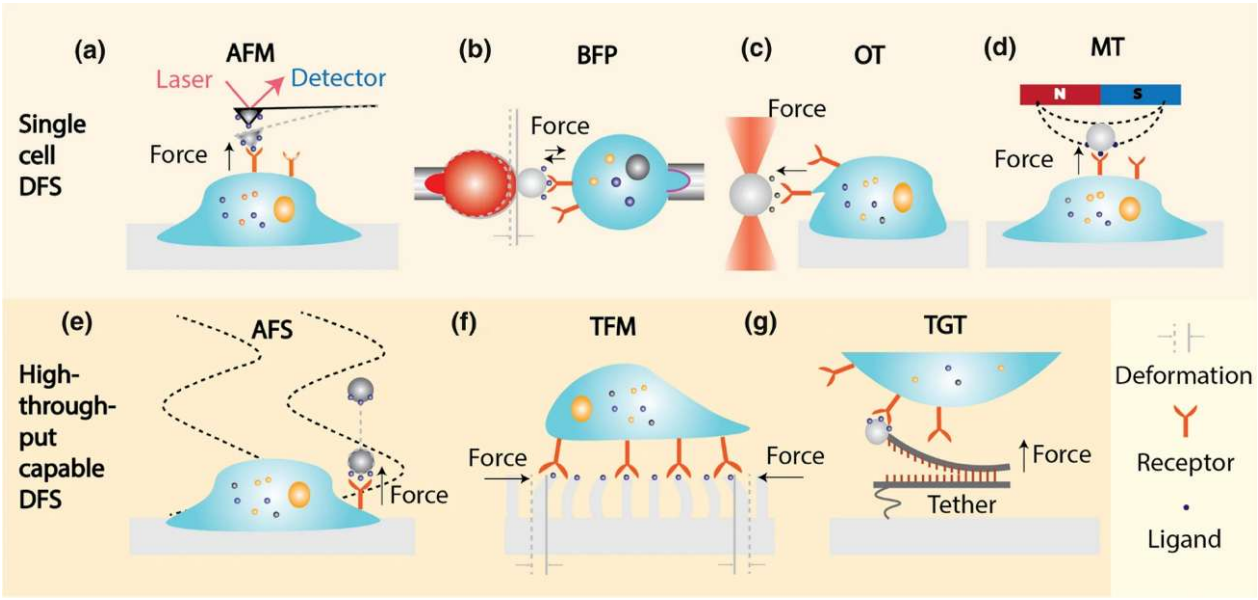

Figure 2.5. Representative image of the variety of DFS applications. Categorised as either 'Single-cell' (top row) or 'High-throughput' (bottom row) [15].

2.2.2.1. Single-Cell DFS Application

Single-cell force spectroscopy represents an important set of established techniques, utilised for probing the mechanical environment of individual living cells, revealing the nuanced behaviours within cell populations. *Atomic Force Microscopy (AFM)* is a noteworthy, versatile technique that has the ability to manipulate and evaluate

forces at the single-cell level [121]. It utilises a sharp tip on a micro-fabricated cantilever to indent cell surfaces and map the cell's mechanical properties such as elasticity. This facilitates the identification of subcellular structures, for instance the cytoskeleton, and the quantitative measurement of cellular moduli across various cell types and conditions [122]. In contrast, *micropipette-based assays* offer alternative approaches through both single and dual micropipette techniques as well as the advanced *Biomembrane Force Probe (BFP).* By applying controlled pressures, micropipette aspiration is capable of manipulating cells to measure the viscoelastic properties and membrane tension of the cell body [15]. Typically, BFP employs a red blood cell as a piconewton force sensor to precisely characterise two-dimensional (2D) ligand-receptor binding kinetics on individual live cells. It facilitates in identifying the association and dissociation rates as well as the bond lifetime and stiffness of the cells [123]. These techniques have the capability to be coupled with fluorescence imaging to correlate mechanical events with intracellular signaling pathways [124].

To study threshold forces required for detachment and tethering formation, *Optical Tweezers (OT),* with its ability for three-dimensional (3D) manipulation, can precisely control these cell interactions. OT uses a non-invasive approach by directing a focused laser beam to trap and exploit single cells or protein-coated beads. The distance between the restrained bead or live cell and the focus of the laser beam can be calculated to determine the piconewton-range forces involved in cellular mechanics and adhesion [125]. Similarly, *Magnetic Tweezers (MT),* a biocompatible and selective approach, involves magnetic beads bound to the surface of the cell before a magnetic field gradient is applied. By modulating the gradient, the displacement of the cell is then recorded and mapped [126]. In recent, Single-Molecule Force-Clamp Spectroscopy has been an emerging application that can be integrated with DFS techniques such as AFM and OT. It maintains a continuous force on a single cell or molecule to study the dynamic response, revealing kinetic details on force-dependent cellular processes such as morphological remodelling or adhesion [127].

2.2.2.2. High-throughput DFS Application

With significant developments in the field of single-molecular and single-cell biomechanics, high-throughput force spectroscopy has facilitated in addressing the

limitations of traditional approaches by increasing the quantity of events for simultaneous investigation. Through the implementation of acoustic fields, *Acoustic Force Spectroscopy (AFS)* is a salient tool in applying forces in the sub-piconewton to thousands of piconewtons range upon large populations of biomolecules or cells in parallel. Traditionally, it uses a piezo element that is operated by an oscillating voltage to prompt a levelled acoustic standing wave within a microfluidic chip [128]. Additionally, *Centrifuge Force Microscopy (CFM),* another notable high-throughput approach, is capable of applying centrifugal force onto thousands of tethered beads to visualise and manipulate single molecules simultaneously [129].

Designed for high-content measurements of cellular forces, *Traction Force Microscopy (TFM)* uses flexible substrates that are embedded with markers like beads or micropillars in which cells adhere to. The traction forces exerted by the cells during the adhesion and migration process are then measured and plotted. The dimensions of the deformation produced on the markers, typically ranging between 2 – 20 μm in size, are recorded and computed to quantify the traction force [130]. Incorporating the use of a double-stranded DNA, the *Tension Gauge Tether* is an alternative platform for high-throughput experimental applications. The platform operates on short, double-stranded DNA segments that irreparably dissociate in response to shear-stretch, functioning as sensors to measure the tension levels that are transmitted across cell membrane receptors. The upper strand of the DNA is covalently conjugated to a ligand and then bonded to respective cell receptors. The magnitude of the force required to achieve dissociation is dependent on the DNA strand length as well as sequence [131].

2.3 Acoustic Force Spectroscopy

The pivotal platform, Acoustic Force Spectroscopy (AFS), is categorised as a high-throughput DFS that utilizes acoustic forces for the molecular and cellular study of structural, mechanical, and kinetic properties.

2.3.1. Principle of AFS

The fundamental principle of AFS involves the employment of an acoustic field within a microfluidic chamber and the ensuing interaction between the field and the suspended particle, that is, either live cells or protein-coated beads. The core of an AFS

platform incorporates a piezoelectric element that generates an acoustic standing wave in the planar direction within a fluid-filled microfluidic chip. This acoustic field is driven by an oscillating voltage at the resonant frequency of the piezoelectric device. The planar acoustic standing wave generates a spatially fluctuating pressure map with regions of high pressure (antinodes) and low pressure (nodes) [128], [132], [133].

By introducing a particle in the acoustic domain, an acoustic radiation force is subsequently imparted on it. This is due to the scattering and absorption of the acoustic waves experienced by the particle [134]. This mechanism is dictated by the acoustic contrast factor, which is determined by the differences in the density and compressibility between the particle and the circumambient medium. For AFS assays that require the use of beads, the typical material composition of these beads is either polystyrene or silica, suspended in an aqueous medium. In such cases, the acoustic contrast factor is positive and consequently the beads are propelled toward the acoustic pressure nodes of the planar standing waves [135].

According to the Rayleigh regime, which refers to the event where the particles are significantly smaller than the acoustic wavelength it is interacting with, the Gor'kov theory presents the framework to understanding the acoustic radiation force [136]. The Gor'kov theory stipulates that the acoustic radiation force can be quantified through the negative gradient of an acoustic potential. This acoustic potential is dependent on the time-averaged squared acoustic pressure and velocity fields as well as the acoustic contrast factors relative to the compressibility and density ratios between the particle and the surrounding medium [136]. The mathematical delineation of the acoustic radiation force imparted on a small particle, according to Gor'kov's theory is given by:

$$F(r,t) = -\frac{4\pi}{3}a^3\nabla\left[\frac{1}{2}Re[f_1]\kappa_0\langle p^2\rangle - \frac{3}{4}Re[f_2]\rho_0\langle v^2\rangle\right]$$

where $F(r,t)$ represents the acoustic radiation force as a function of the spatial coordinate r and time t, a is the particle radius, $f_1 = 1 - \frac{\kappa_p}{\kappa_0}$, $f_2 = \frac{2(\rho_p - \rho_0)}{2\rho_p - \rho_0}$, κ_0 is the comprehensibility of the fluid, κ_p is the comprehensibility of the particle, ρ_0 is the equilibrium fluid density, ρ_p is the equilibrium particle density, ρ is the fluid density, $v =$

$|v|$ is the absolute value of the velocity, and the notation $Re[\cdot]$ is the real part of the complex variable [134], [136].

The acoustic radiation force is used to apply a controlled tensile force on the particle, either a protein-coated bead or live cell, which is tethered to the surface of the microfluidic flow cell. By analysing the positional changes of the particle under the influence of the acoustic field, the forces applied to study the molecular unfolding, binding interactions and conformational changes can be accurately calculated [137].

2.3.2. Applications of AFS

As mentioned previously, AFS can be utilised to study the structural and mechanochemical characteristics of single biomolecules alongside assessing the adhesion forces and kinetics of live cells. There are several potential applications involving AFS which can be categorised as either biomolecular or cellular studies.

2.3.2.1. Biomolecular Applications

Regarding the biomolecular applications of AFS, studies can be performed to investigate DNA-related events as well as protein-DNA and protein-protein interactions. With a tuneable force range between sub-piconewton to thousands of piconewton, investigating the mechanical properties of DNA such as torsionally constrained and unconstrained molecules, can be implemented [132]. AFS can also examine the characteristics of singular double-stranded DNA (dsDNA) molecules post-protein-filament assembly and the real-time localisation of viral particles surrounding a DNA template. By determining the force-extension behaviour of the dsDNA, comparisons can be done with models, for example the extensible worm-like chain (WLC) model [128]. In conjunction to this, AFS has also established a distance-clamp mode that can be utilised to concurrently probe several rupture events on the same construct, elucidating key information such as DNA hairpin disruption, the overstretching of DNA, and protein unfolding [132], [138].

2.3.2.2. Cellular Applications

In the context of cellular applications, AFS has demonstrated its capabilities in discriminating between cells hinged on their adhesion properties. AFS can be employed

to investigate both cell-ECM interactions and cell-cell interactions[139]. For example, AFS has been previously utilised to investigate the binding kinetics of CD4+ T lymphocytes to the ECM protein, fibronectin, as an *in-vitro* model for CD4+-endothelium invasion. Further insights can be achieved through cell-cell interactions, that is, immune cells interacting with endothelial cells before introducing acoustic force [133]. The AFS platform also has potential in diagnostic development and drug screening by identifying the T cell adhesion changes associated with pathologies. Alongside these applications, AFS has also shown promise in probing the viscoelastic properties of red blood cells (RBCs) as a function of multiple drug treatments [140].

2.3.2.3. Emerging Technological Advancements

AFS is a versatile technique that is emerging as a fundamental technique to study biomolecules and live cells with high-throughput capacity. As of recent, there have been several advancements in the platform's configuration, including the development of transparent piezo elements. By allowing transillumination, AFS can be combined with low-light fluorescence detection, for example confocal, super-resolution, or total internal reflection fluorescence microscopy, to obtain high quality images of the tethered particles. By utilising modelling tools such as the 1D MATLAB model, the AFS microfluidic flow cell design can be enhanced for particular force profiles [128], [132]. With the ability to shape these force profiles, large length changes of biomolecules can be calculated.

2.4 Microfluidic Systems

Operating in the microscale, microfluidic systems incorporate a controlled milieu for the manipulation of fluids and biological particles. It functions under the principle of laminar flow to achieve precise applications of shear stress. Typically, these systems leverage channels with dimensions that range up to hundreds of micrometres.

2.4.1. Principle of Microfluidics

Known as Stokes flow, low Reynolds number hydrodynamics determines the behaviour of fluids. The Reynolds number is a dimensionless number that represents the ratio of inertial forces to viscous forces which is defined by the equation:

$$Re = \frac{\rho D v}{\mu}$$

where Re represents the Reynold number, ρ is the density of the fluid, D is the diameter of the channel, v is the velocity of the fluid and μ is the viscosity of the fluid [141].

Due to the small channel diameter and low fluid velocities, the derived Reynolds number is often calculated to be less than 1 meaning the viscous forces govern inertial forces, resulting in laminar flow where the adjacent fluid layers begin moving at parallel with negligent mixing caused by turbulence [142]. The laminar flow is time-symmetric whereby reversing the applied pressure will reverse the fluid motion. It is important to note that the flow profile is determined by the range that the Reynolds value lies within. To elaborate, if Re is less than or equal to 2,000, the velocity profile takes on a parabolic shape, if Re is within 2,000 and 4,000, the velocity profile is within the transition region, and if Re is greater than 4,000, the velocity profile is in the turbulent flow area and is substantially flat [141], [142]. By evaluating the Re value, the flow velocity pattern and boundary conditions can be defined. The shear stress experienced in the flow cell that is caused by the turbulence of fluid layers moving at varying velocities, is directly proportional to the shear rate. The shear rate is given by the gradient of the flow velocity respective to the direction which is perpendicular to the flow [143].

2.4.2. Application of Microfluidics

Microfluidic systems use hydrodynamic forces to precisely manipulate fluid flow and apply defined shear stresses for a wide range of biological studies such as cellular mechanics, adhesion and mechanotransduction. Laminar Flow-based Shear devices are designed to employ shear stress within the flow cell by defining the shear rate through exact dimensions of the channel and a pre-determined flow rate. By incorporating narrower channels and higher flow rates, proportional to these values, the shear stress will subsequently increase [144], [145]. Another model of a microfluidic system is the Parallel Plate Flow Chamber, designed to mimic flow conditions that are comparable to blood vessels. With the shear stress proportional to the viscosity of the fluid and flow rate, the flow chamber is used to study the endothelial cellular response to shear force, similar to that exerted by blood flow [146]. Utilising these devices can provide insights into the signaling pathways, changes to cell morphology and gene expression in response

to shear stress. Alongside applications in cell adhesion and mechanotransduction studies, microfluidics has emerged in the drug delivery field as well. For example, a study has demonstrated the potential of microfluidics through implementing shear-induced nanoparticles for targeted drug delivery to impede blood vessels [147].

2.5 Micropipette Aspiration

Micropipette aspiration is a prominent technique used to study mechanobiology, specifically the mechanical properties of individual living cells. The platform involves generating a controlled negative suction pressure within a finely pulled borosilicate glass micropipette and aspirating single cells. The magnitude of the cellular deformation exhibited, respective to the aspiration pressure, allows for the quantification of certain mechanical properties including membrane tension, elastic modulus, and stiffness.

2.5.1. Fluorescence Micropipette Aspiration Assay to Investigate Red Blood Cell Mechanosensing

Jasmine Jin is the principal author of the following publication, which forms the part of this thesis submitted for the examination for the Master of Philosophy. The corresponding author below provides their consent for the inclusion of the following publication in this thesis and accept the following candidate statement of contribution for this publication.

Journal of Visualised Experiments: Jin Jasmine, Wang Jerry Haoqing, Chen Catherine Yiyao, Russell Blake, Sun Allan, Wang Yao, Ju Lining Arnold Fluorescence Micropipette Aspiration Assay to Investigate Red Blood Cell Mechanosensing. JoVE (2024). DOI: 10.3791/66265

Candidate contribution:

This is the method paper to explain and demonstrate the recent advances in utilising micropipette to study the single cell mechanobiology. The manuscript was written, formatted, and prepared by Jasmine Jin. This author designed the paper, and all co-authors did the literature research.

Corresponding Author	Signature	Date
Lining Arnold Ju		11/07/2025

jove

Fluorescence-coupled Micropipette Aspiration Assay to Investigate Red Blood Cell Mechanosensing

Jasmine Jin [1], **Haoqing Jerry Wang** [1,2,3], **Yiyao Catherine Chen** [1], **Blake Russell** [1], **Allan Sun** [1,2,3,4], **Yao Wang** [1], **Lining Arnold Ju**1,2,3,4

1 School of Biomedical Engineering, The University of Sydney2Charles Perkins Centre, The University of Sydney [3] Heart Research Institute [4] The University of Sydney Nano Institute (Sydney Nano), The University of Sydney

Corresponding Author

Lining Arnold Ju
arnold.ju@sydney.edu.au

Citation

Jin, J., Wang, H.J., Chen, Y.C., Russell, B., Sun, A., Wang, Y., Ju, L.A. Fluorescence-coupled Micropipette Aspiration Assay to Investigate Red Blood Cell Mechanosensing. ***J. Vis. Exp.*** (203), e66265, doi:10.3791/66265 (2024).

Date Published

January 12, 2024

DOI

10.3791/66265

URL

jove.com/video/66265

Abstract

Micropipette aspiration assays have long been a cornerstone for the investigation of live-cell mechanics, offering insights into cellular responses to mechanical stress. This paper details an innovative adaptation of the fluorescence-coupled micropipette aspiration (fMPA) assay. The fMPA assay introduces the capability to administer precise mechanical forces while concurrently monitoring the live- cell mechanotransduction processes mediated by ion channels. The sophisticated setup incorporates a precision-engineered borosilicate glass micropipette connected to a finely regulated water reservoir and pneumatic aspiration system, facilitating controlled pressure application with increments as refined as ± 1 mmHg. A significant enhancement is the integration of epi-fluorescence imaging, allowing for the simultaneous observation and quantification of cell morphological changes and intracellular calcium fluxes during aspiration. The fMPA assay, through its synergistic combination of epi-fluorescence imaging with micropipette aspiration, sets a new standard for the study of cell mechanosensing within mechanically challenging environments. This multifaceted approach is adaptable to various experimental setups, providing critical insights into the single-cell mechanosensing mechanisms.

Introduction

The unfolding discoveries in the world of cellular behaviors have accentuated the role of mechanical stimuli, such as tension, fluid shear stress, compression, and substrate stiffness, in dictating dynamic cellular activities such as adhesion, migration, and differentiation. These mechanobiological aspects are of paramount importance in elucidating how cells interact with and respond to their physiological environments, impacting various biological processes1,2.

Over the past decade, micropipette-based aspiration assays have stood out as a versatile tool in studying diverse cellular responses to mechanical stimuli. This technique offers valuable insights into the intrinsic mechanical properties

of living cells at the single-cell level, including cellular elastic modulus, stiffness, and cortical tension. These assays enable the measurement of various mechanical parameters, such as cell membrane tension, pressure exerted on the cell membrane, and cortical tension (summarized in **Table 1**). Studying the aspirational forces has enriched our understanding of how they influence cellular functions and processes, particularly in the realm of membrane dynamics, including fragmentation, elongation, and budding3,4.

Mechanical Parameter	Description	Seminal Approaches
Cell Stiffness	Measurement of a cell's mechanical rigidity and elasticity.	Aspiration of the cell membrane and analysis of deformation response to the negative pressure20,21.
Adhesion Strength	Evaluation of how strongly cells adhere to surfaces.	Application of controlled suction to detach adhered cells from a substrate2,22.
Membrane Tension	Assessment of the tension or stress within cell membranes.	Measurement of the membrane deformation in response to applied pressure23,24.
Viscoelastic Properties	Characterization of a cell's combined viscous and elastic behavior.	Analysis of the time-dependent deformation response to aspiration23,25
Deformability	Determination of how easily a cell can change shape.	Evaluation of the extent of deformation under controlled suction20,24.
Surface Tension	Measurement of the tension at the cell's surface.	Assessment of the pressure required to form a micropipette membrane protrusion26.
Cell-Material Interaction	Study of interactions between cells and materials or substrates.	Aspiration of cells in contact with different materials and observation of interactions2,24.
Cell-Cell Interaction	Examination of interactions between neighboring cells.	Aspiration of a group of cells and analysis of their intercellular forces27.

Table 1: Mechanical parameters characterized by the micropipette aspiration assay.

The micropipette-based aspiration technique has been widely used to study red blood cells (RBCs), assessing the deformability and various mechanical characteristics of RBCs, which is essential in understanding their function in the circulatory system. RBCs exhibit remarkable adaptability, preserving their mechanical versatility against deformation when navigating through the intricate capillary network and inter-endothelial clefts5,6. During this journey, RBCs must traverse through passages as narrow as 0.5-1.0 µm, subjecting themselves to a multitude of mechanical forces, including tension and compression7,8,9. They also have high sensitivity to the shear stress generated by blood flow during circulation10. These processes promote the activation of regulatory mechanisms involving calcium influx, a crucial signaling event with well-established roles in cellular responses to mechanical stimuli11,12. The complex mechanisms governing the calcium-mediated mechanosensing remain compelling subjects of ongoing investigation.

In this context, the fMPA stands as an effective approach to reveal the extent of calcium mobilization under precisely controlled mechanical forces, allowing for the simultaneous application of mechanical modulation (using the micropipette aspiration system) and visualization of calcium intensity (using fluorescent indicators). It particularly mimics the physiological scenario when the RBC travels through narrowing blood vessels. It is worth noting that the fMPA system we developed can generate pressure with a resolution of 1 mmHg. The implemented high-speed camera can achieve a temporal resolution of 100 ms and a spatial resolution at the submicron-meter level. These configurations ensure the precise application of mechanical forces to live cells and simultaneously capture the resulting cellular signaling. Moreover, due to the integrative engineered nature of this setup, the micropipette aspiration assay can be readily adapted to complement other equipment or techniques, enabling further exploration of the intricacies of cell mechanics. This versatility stands as an additional advantage of this approach.

Protocol

This protocol follows the guidelines of and has been approved by the Human Research Ethics Committee of the University of Sydney. Informed consent was obtained from the donors for this study.

1. Human RBC isolation

NOTE: Step 1.1 should be performed by a trained phlebotomist using a protocol that has been approved by the Institutional Review Board.

1. Withdraw 5 mL of blood from the median cubital vein using a 19 G butterfly needle.
2. Transfer the collected blood into a 15 mL tube containing 1:200 enoxaparin to prevent clotting.
3. Dilute 5 µL of enoxaparin-anticoagulated blood in 1 mL of carbonate/bicarbonate buffer (C-buffer, pH = 8.5-9; **Table of Materials**). Centrifuge the diluted blood sample
4. at 900 × ***g*** for 1 min
   to sediment the RBCs. Carefully decant the supernatant without disturbing the pellet.
5. Perform two washes of the RBC pellet with 1 mL of C-buffer (**Table of Materials**), centrifuging each time at 900 × ***g*** for 1 min.
6. Subsequently, wash the RBC pellet 2x with 1 mL of Tyrode's buffer using the same centrifugation conditions

and then resuspend the final pellet in 1 mL of Tyrode's buffer to obtain the washed stock RBC suspension.

2. Calcium indicator loading

1. Adjust the concentration of the washed stock RBC solution to 10 × 106 cells/mL in Tyrode's buffer, based on the cell count obtained using an automatic cell counter (**Table of Materials**).
2. Label the calcium inside the RBCs by incubating with 16.67 µM Cal-520 AM, a calcium-sensitive dye, while agitating on a rotary tube mixer for 1 h.
3. Dilute the RBCs in Tyrode's buffer containing 0.5% bovine serum albumin (BSA) at a 1:50 ratio. The cells are now ready for experimental use.

3. Micropipette fabrication

1. Mount the borosilicate glass capillary tube (1 mm outer diameter x 0.6 mm inner diameter) onto the P-1000 micropipette puller to produce two corresponding micropipettes with closed tips at the pulling site using the preset pulling program. For this setup, use the following pulling program values**: heat 516, pull 150, velocity 75, time 250,** and **pressure 500**. NOTE: Heating and pulling parameters set in the pulling program can be customized and are dependent on the desired settings of the experimental design12. **CHECKPOINT** (see **Supplemental Table S1**).
2. Open the closed tip by mounting one of the close-ended micropipettes procured after pulling onto the micropipette cutter. Adjust the heating temperature to approximately 50-60 °C.
3. Locate the micropipette using a 10x eyepiece. Move the micropipette close to the borosilicate glass bead by using the knobs for adjustment.
4. Change the eyepiece to 30x before positioning the micropipette as close to the borosilicate glass bead as possible without bending the pipette tip.
5. Soften the borosilicate glass bead using heat by stepping onto the heating pedal. Gently insert the raw closed micropipette tip into the softened bead until the desired endpoint, the opening diameter, has been reached.
6. Release the foot pedal and let the glass bead cool down. Make sure the tip of the micropipette always remains inside the bead.
   NOTE: Inserting the tip further leads to larger opening diameters.
7. Gently extract the micropipette, leading to a clear straight cut on the closed micropipette. Confirm that the final diameter of the capillary is 1 µm.
   NOTE: **CHECKPOINT** (see **Supplemental Table S1**)

4. Cell chamber preparation

1. Use a diamond pencil to divide a standard 40 mm x 22 mm x 0.17 mm glass coverslip into three equal strips.
2. Adhere one piece of the cut glass coverslip to the bottom of a homemade chamber holder with vacuum grease.
   NOTE: The chamber holder consists of two metal (copper/aluminum) squares that are linked by a curved handle. The distance between the metal blocks must span less than 40 mm for the cut coverslip to adhere to the holder to form a parallel chamber.
3. Adhere the second piece of the cut glass coverslip to the top of the homemade chamber holder with vacuum grease .

NOTE: **CHECKPOINT** (see **Supplemental Table S1**)

4. Inject 200 µL of the labeled RBC suspension between two coverslips using a 200 µL pipette gun (**Figure 1**).

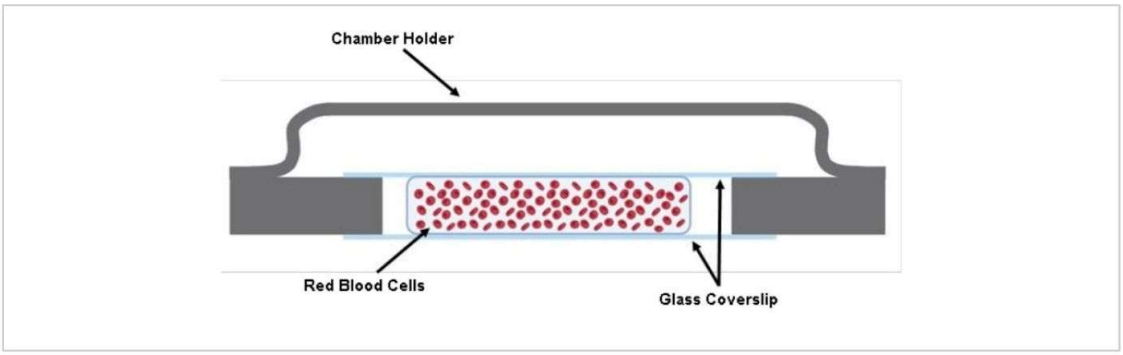

Figure 1: Illustration of the cell chamber. Two cut pieces of a 40 mm x 22 mm x 0.17 mm glass cover slip are adhered to the chamber holder using grease. Between the two cut glass coverslips, approximately 200 µL of the cell solution in Tyrode's Buffer is seeded. Please click here to view a larger version of this figure.

5. Micropipette aspiration assembly

1. Mount the cell chamber onto the holder stage present on the microscope platform. Adjust the position so that the cell chamber is directly above the objective (**Figure 2B**).
2. Lower the micropipette holder to below the fluid level of the connected water reservoir.
3. Inject either demineralized water or Tyrode's buffer into the fabricated micropipette and carefully remove all air bubbles using a syringe coupled with a 34 G needle (**see Table of Materials**).
4. Unscrew the end of the micropipette holder halfway and allow the water to drip from the micropipette holder for a few seconds.
   NOTE: **CHECKPOINT** (see **Supplemental Table S1**)
5. Insert the micropipette into the holder tip. Tighten the holder screw to ensure the micropipette is fixed.
6. Insert the micropipette into the cell chamber and locate the micropipette and RBCs under the microscope. Use the micromanipulator to adjust the position.
7. Lower the micropipette tip further to ensure the tip is leveled with the located RBC.
   NOTE: **CHECKPOINT** (see **Supplemental Table S1**)
8. Zero the hydraulic pressure at the micropipette tip by adjusting the height of the water reservoir. Then, slightly raise the water reservoir to generate a subtle positive pressure at the tip.

6. Perform the fluorescence-coupled micropipette aspiration assay

1. Turn on the 488 nm fluorescent excitation light source. Do not switch on the fluorescence shutter at this stage to avoid photobleaching (**Figure 2C**). Turn on the fluorescence camera and the transmitted camera.

NOTE: Both cameras are operated using the appropriate software (see **Table of Materials**).

2. Set up the desired **exposure time** (**100 ms** for both cameras in this study), region of interest (ROI), binning size (none for this study) for both cameras in the software. Open up the **multi-dimension acquisition panel** to set up the **acquisition frame number, 2,000 for this study**, and saving directory.
   NOTE: The acquisition frame number is dependent on the desired number of aspiration events that are to be recorded. For 1 aspiration event, the range of the acquisition number should be set within 100-500, which is approximately 10-50 s.

3. Find the micropipette under the field of view using the micromanipulator.

4. Turn on the pneumatic pressure clamp, including the control box and the clamp system (**Figure 2A**). Make sure the **control box** is in the **EXTRNL mode**. Compensate any offset pressure inside the system by slowly rotating the knob.

5. Turn on the separate software that controls the pneumatic clamp. The software has an electrical control panel to control the discrete analog input to the clamp system. The pressure is controlled with a 20 mV/mmHg conversion factor.

6. Zero the pressure inside the system. Carefully relocate the micropipette close to the RBCs. Adjust the water reservoir position until a subtle positive pressure is noticed at the micropipette tip.

7. Start the acquisition in the camera-operating software. Switch on the **fluorescence shutter**.

8. Aspirate an RBC by typing in the calculated voltage magnitude into the control panel to reach the desired pressure. NOTE: The pressure for aspirating an RBC is typically in the range of Δp = **-5 to -40 mmHg.** There should be a noticeable tongue elongation within the micropipette tip (**Figure 2D**).

9. Hold the pressure for a preset period; then, release the pressure.

10. Move the micropipette to pick up the next cell and repeat the experiment.

7. Fluorescence intensity analysis

1. Load the saved fluorescence images into the analysis software.

2. Adjust the **intensity threshold** using the **display adjustment** tab. Do this by either manually inputting the values or using the slider to ensure the fluorescence images show a clear contrast of the cell in the analysis software (see **Supplemental File 1-Supplemental Figure S1**).

3. Scroll to the timeline at the bottom of the software. Locate the designated aspiration event.

4. Click **Add new surfaces**. Define the analysis ROI.
   NOTE: The software provides a guided five-step process to adjust and complete the segmentation (see **Supplemental File 1-Supplemental Figure S2** and **Supplemental Figure S3**).
   NOTE: Keep the ROI as small as possible to save computational resources.

5. Use the background subtraction slider and adjust the segmentation threshold using the slider to obtain the best segmentation outcome.

NOTE: This means that apart from the aspiration event, the background should be segmented as accurately as possible (see **Supplemental File 1-Supplemental Figure S4** and **Supplemental Figure S5**).

6. Add an **area** filter to exclude background noises (see **Supplemental File 1-Supplemental Figure S6**).
   NOTE: This is completed in the post process stage.

7. Select the **statistics** tab | **detailed** tab | **average values** tab. Scroll to find and select the intensity mean (see **Supplemental File 1-Supplemental Figure S7**).

8. Export the fluorescence signal trace over time to a .csv file.

9. Open the exported csv file. Subtract the background signals, ***F***b, from all measurements.

10. Calculate the calcium intensity change, ***ΔF***max, using equation (**1**):

$$\Delta F_{\max} = \frac{F_{\max}}{F_0} = \frac{F_{\max,\text{absolute}} - F_b}{F_{0,\text{absolute}} - F_b} \quad (1)$$

Where ***ΔF***max is the maximum calcium intensity change, ***F***b, is the background intensity, and ***F***0 is the resting intensity.

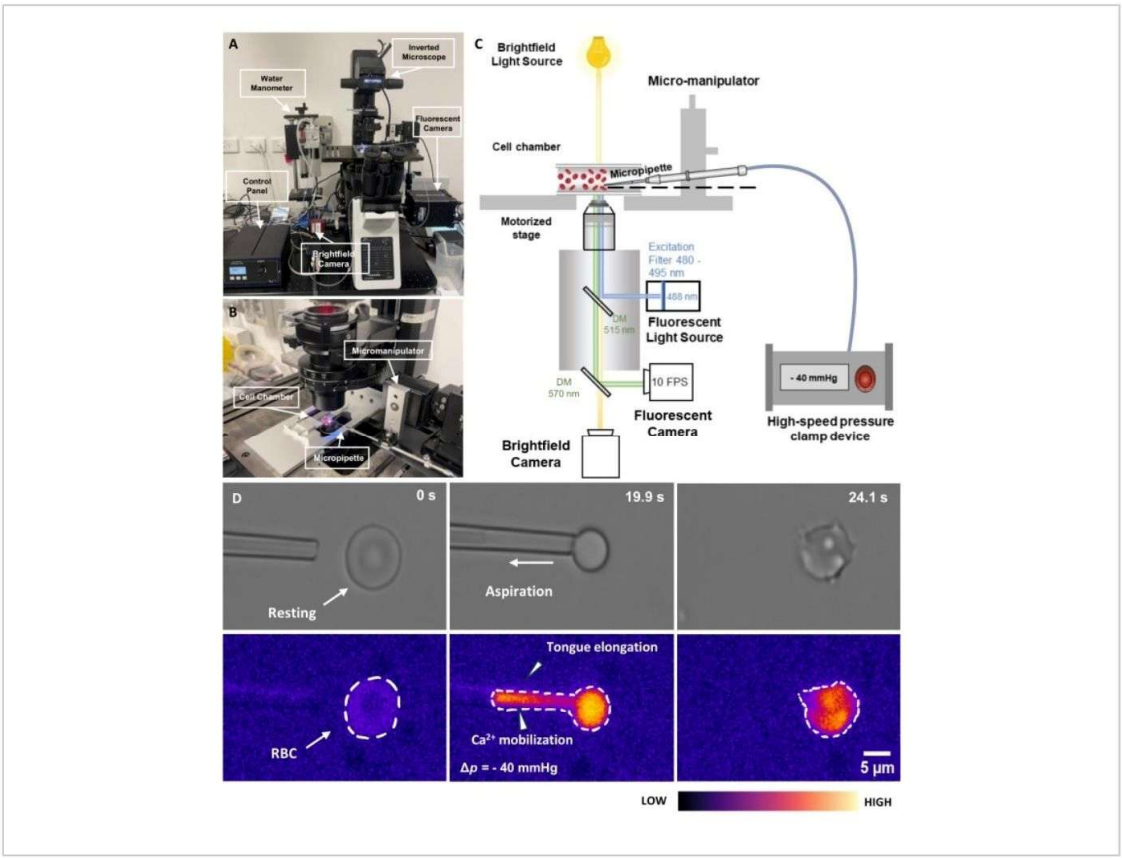

Figure 2: Fluorescence-coupled micropipette aspiration assembly. (**A**) An overview of the fMPA hardware system incorporating the inverted microscope combined with the brightfield and fluorescence cameras. The left side of the image depicts the homemade water manometer and the control box that allows to precisely tune the pressure of the pneumatic pressure pump. (**B**) The microscope stage depicting the experiment cell chamber and micromanipulator system with a single micropipette. (**C**) Schematic of the fMPA system setup. Concurrent imaging of brightfield (yellow) and fluorescence (blue emission, green excitation) signals utilizing two dichroic mirrors to direct the light paths from the fluorescence light source (blue) to the target, then to the cameras for imaging (green). (**D**) The top row depicts the brightfield images whereas the bottom row demonstrates the fluorescence images. The left represents the position of the micropipette before aspiration when the RBC is at rest.The middle column snapshots the aspiration process where the RBC experiences a negative pressure of -40 mmHg. The right depicts the cell morphology after experiencing the negative aspiration pressure. Scale bar = 5 µm. Abbreviations: fMPA = Fluorescence-coupled Micropipette Aspiration; DM = dichroic mirror; RBC = red blood cell. Please click here to view a larger version of this figure.

Representative Results

To establish micropipette aspiration assays, we first constructed a custom cell chamber comprising two metal squares (copper/aluminum) connected by a handle. Two third-cut glass coverslips (40 mm × 7 mm × 0.17 mm) were affixed to create a chamber filled with 200 µL of RBCs suspended in Tyrode's Buffer. After introducing RBCs into the chamber, a tailored borosilicate micropipette was secured on a holder and carefully positioned within the chamber using a micro-manipulator. Subsequently, the micropipette was brought closer to capture the target RBC.

For cell aspiration, the method used a pneumatic high-speed pressure clamp to fine-tune the negative aspiration pressure. Fluorescence imaging was then conducted to investigate the calcium mobilization at the different negative aspiration pressures applied.

By using the fMPA to investigate how RBCs respond to varying negative aspiration pressures, our findings reveal that there is a clear proportional relationship between the negative pressure applied and the calcium influx present in the aspirated RBC. To determine the calcium intensity change, the maximum intensity of the single aspirated cell (***Fmax***) minus the background intensity (***Fb***) was divided by the resting intensity (***F0***) minus ***Fb***. There was a corresponding increase in the influx of calcium ions into the RBCs when the pressure was incrementally increased between -10 mmHg **(Figure 3A)** to -40 mmHg **(Figure 3D).** This suggests that RBCs possess the ability to sense changes in their mechanical and respond by rapid calcium-specific channel activities14,15.

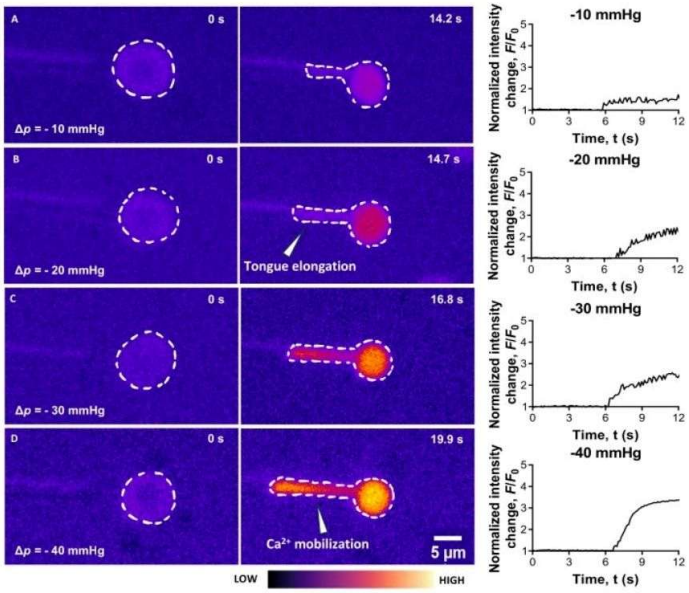

Figure 3: Fluorescence imaging with a graphical representation of normalized intensity changes against time. Horizontally across depicts fluorescence snapshots of the RBCs at rest (left) and the human RBCs being aspirated by the micropipette (middle). Representative traces of the RBCs being aspirated at multiple negative aspiration pressures (***Δp***) can be seen on the right. The negative aspiration pressure is incrementally increased, starting at (**A**) ***Δp*** = -10 mmHg, (**B**) ***Δp*** = -20 mmHg, (**C**) ***Δp*** = -30 mmHg, and (**D**) ***Δp*** = -40 mmHg. When the tongue of the RBC is elongated during aspiration, a significant calcium mobilization can be observed as shown by the increased Cal-520 AM fold change. ***F***/***F***0 was used to investigate the calcium mobilization inside the aspirated RBC. From the above curves, the observed trend demonstrated that the Cal-520 AM signal increased proportionally with the increase of the applied negative aspiration pressure. Scale bar = 5 µm. Abbreviation: RBCs = red blood cell. Please click here to view a larger version of this figure.

Supplemental Table S1: Checkpoints for critical steps in the fMPA preparation protocols. Please click here to download this File.

Supplemental File 1: A guided process to adjust and perform segmentation. Please click here to download this File.

Discussion

Micropipette aspiration assays embody a refined methodology, deploying substantial pressure modulation,

exact spatial orchestration, and reliable temporal discernment to probe the profound intricacies of cellular biomechanics. This study places particular emphasis on the application of fMPA as a crucial tool for unveiling the nuanced mechanosensitive responses showcased by RBCs under varying stimuli. The concurrent use of brightfield and fluorescence signals enabled a multifaceted exploration of cellular phenomena, advancing the monitoring and detection of intracellular calcium influx in real time. This approach provides an integrative insight into the complex mechanosensing reactions of RBCs.

Importantly, the applicability of the fMPA technique extends beyond RBCs, as it can be employed with other cell types that disapply high mechanical sensitivity, such as platelets and neurons9. Moreover, owing to its minimal impact on cell integrity during experimental handling, fMPA guarantees the preservation of the cell's natural state, making it highly suitable for use with primary cells1. Furthermore, the fMPA method offers versatility through the tunable geometry of the micropipettes, allowing for a broader range of experimental designs tailored to specific research questions and the effective exploration of various mechanical conditions.

Additionally, with the improvement in the optical pathway that enhances the simultaneous use of multi-fluorescence imaging, the fMPA system allows for real-time detection of intracellular calcium concentration upon aspiration. This capability opens an opportunity to explore calcium-related molecules, such as the mechanosensitive ion channel, PIEZO1, which has been shown to mediate and perceive mechanical cues from the external environments7,14. Recent literature highlights an increase in membrane tension as a significant factor stimulating PIEZO1 channel activity, subsequently facilitating the Ca^{2+} influx6. This underscores a crucial application of fMPA, which is to investigate the interplay between membrane tension, PIEZO1, and calcium influx, shedding light on the intricate mechanosensing processes within cells.

From a technical perspective, it is worth mentioning that the two primary components of the fMPA system, responsible for generating the aspiration force (mechanical stimuli) and conducting real-time fluorescence imaging, are the pneumatic pressure pump and the fluorescence camera, respectively. The selection of the appropriate pump and camera for the system should be based on the specific cell type and biological process under study. The pump employed in our system operates within a steady-state pressure range of ± 200 mmHg and can respond to commands for pressure changes as significant as ± 200 mmHg. The pressure rise time and fall time should not exceed 6-8 ms for a 20 mmHg step and 15-20 ms for a 200 mmHg step. To ensure force resolution, the noise level of the HSPC system should be less than ± 0.5 mmHg, peak-to-peak. These requirements are applied in this setup; however, a range of ± 40 mmHg is sufficient to achieve a response for the experimental protocol15. Regarding the fluorescence camera, we selected features a 95% Quantum Efficiency and an 11 µm x 11 µm pixel size chip. This sensitive sensor configuration efficiently captures the fluorescence signal at high speed. Additionally, it is crucial to maintain a median read noise of 1.6e- for an adequate signal-to-noise ratio during imaging16.

From a procedural perspective, executing fMPA requires a set of advanced skills. For example, crafting micropipettes using the micropipette cutter demands precision and dexterity, along with meticulous control of temperature and positioning. Positioning the micropipette within the microscope's field of view requires meticulous effort to

avoid damage to both the micropipette tip and the cellular chamber. Additionally, one common challenge associated with fluorescence imaging is photobleaching. To mitigate this issue, it is important to minimize the sample's exposure time to the illumination system. With reference to the 'fluorescence-coupled micropipette aspiration assay' protocol, the fluorescence shutter of the excitation light source remains switched off until all parameters are inputted through the camera-operating software and the aspiration system is ready for experiments. Only then is the fluorescence shutter turned on to commence imaging. To further reduce the photobleaching, it is recommended to use the minimum light source intensity that still yields adequate fluorescence expression in the sample.

Furthermore, the current manual operation required for fMPA assays makes this technique labor-intensive. Consequentially, the inconsistencies that may arise in this assay primarily stem from operator-dependent variables, as well as the factors associated with variations in filament preheating and capillary glass characteristics. In the future, optimizing the performance of this technique necessitates consideration of potential tandem implementations. For example, when combined with microfluidic devices, the micropipette aspiration can be transformed into a high-throughput platform, significantly increasing the experimental rate from studying around 20 cells per hour to approximately 1,000 cells/h17,18. This incorporation also improves the reproducibility of the data. Moreover, certain avenues have been successfully explored by incorporating automation and image analysis systems19. Notably, finite element analysis (FEA) is a computational tool commonly employed to model micropipette aspiration assays. FEA can predict the cellular response to mechanical stimuli and characterize their mechanical properties. It holds the potential to optimize the micropipette design and further validate the experimental results19.

In conclusion, the fMPA approach offers valuable insights into the mechanosensitive behaviors of RBCs in responding to mechanical stimuli. This study establishes a foundational framework for future investigations into the intricate mechanisms of mechanotransduction within RBCs and across broader biological systems. Such inquiries hold great promise for advancing our understanding of these mechanisms and unraveling their extensive implications in various physiological contexts.

Disclosures

The authors declare that they have no competing interests to report regarding the present study.

Acknowledgments

We thank Nurul Aisha Zainal Abidin and Laura Moldovan for additional donor recruitment, blood collection, and phlebotomy support. We thank Tomas Anderson and Arian Nasser for organizing the equipment and reagents. This research was funded by the Australian Research Council (ARC) Discovery Project (DP200101970-L.A.J.); the National Health and Medical Research Council (NHMRC) of Australia Ideas Grant (APP2003904-L.A.J.); NHMRC Equipment Grant-L.A.J.; NSW Cardiovascular Capacity Building Program (Early-Mid Career Researcher Grant- L.A.J.); NSW CVRN-VCCRI Research Innovation Grant; Office of Global and Research Engagement (Sydney- Glasgow Partnership Collaboration Award-L.A.J.); L.A.J. is a National Heart Foundation Future Leader Fellow Level 2 (105863), and a Snow Medical Research Foundation Fellow (2022SF176).

References

1. González-Bermúdez, B., Guinea, G. V., Plaza, G. R. Advances in micropipette aspiration: applications in cell biomechanics, models, and extended studies. ***Biophysical Journal*** **116** (4), 587-594 (2019).
2. Mierke, C. T. ***Physics of Cancer, Volume 3 (Second Edition): Experimental biophysical techniques in cancer research.*** IOP Publishing (2021).
3. Chen, Y. et al. Loss of the F-BAR protein CIP4 reduces platelet production by impairing membrane-cytoskeleton remodeling. ***Blood.*** **122** (10), 1695-1706 (2013). Shin,
4. J.-W., Swift, J., Spinler, K. R., Discher, D. E. Myosin-II inhibition and soft 2D matrix maximize multinucleation and cellular projections typical of platelet-producing megakaryocytes. ***Proceedings of the National Academy of Sciences.*** **108** (28), 11458-11463 (2011).
5. Liapis, H., Foster, K., Miner, J. H. Red cell traverse through thin glomerular basement membrane. ***Kidney International.*** **61** (2), 762-763 (2002). Wang, H. et al.
6. Fluorescence-coupled micropipette aspiration assay to examine calcium mobilization caused by red blood cell mechanosensing. ***European Biophysics Journal.*** **51** (2), 135-146 (2022).
7. Danielczok, J. G. et al. Red blood cell passage of small capillaries is associated with transient Ca2+-mediated adaptations. ***Frontiers in Physiology.*** **8**, 979 (2017).
8. Diez-Silva, M., Dao, M., Han, J., Lim, C.-T., Suresh, S. Shape and biomechanical characteristics of human red blood cells in health and disease. ***MRS Bulletin.*** **35** (5), 382-388 (2010).
9. Maître, J.-L., Niwayama, R., Turlier, H., Nédélec, F., Hiiragi, T. Pulsatile cell-autonomous contractility drives compaction in the mouse embryo. ***Nature Cell Biology.*** **17** (7), 849-855 (2015).
10. Ju, L., Chen, Y., Xue, L., Du, X., Zhu, C. Cooperative unfolding of distinctive mechanoreceptor domains transduces force into signals. ***eLife.*** **5**, e15447 (2016).
11. Bogdanova, A., Makhro, A., Wang, J., Lipp, P., Kaestner, L. Calcium in red blood cells-a perilous balance. ***International Journal of Molecular Sciences.*** **14** (5), 9848-9872 (2013).
12. Oesterle, A. ***Pipette Cookbook 2018.*** https://www.sutter.com/PDFs/cookbook.pdf (2018).
13. Cahalan, S. M. et al. Piezo1 links mechanical forces to red blood cell volume. ***eLife.*** **4**, e07370 (2015).
14. Sforna, L. et al. Piezo1 controls cell volume and migration by modulating swelling-activated chloride current through Ca2+ influx. ***Journal of Cellular Physiology.*** **237** (3), 1857-1870 (2022).
15. High-speed pressure clamp - ALA Scientific Instruments. ***ALA Scientific.*** https://alascience.com/products/hspc-2sb/ (2023).
16. ***Teledyne Imaging Prime 95BTM Scientific CMOS Camera Datasheet.*** https://www.photometrics.com/wp-content/uploads/2019/10/Prime-95B-Datasheet-07172020.pdf (2020).
17. Lee, L. M., Lee, J. W., Chase, D., Gebrezgiabhier, D., Liu, A.P. Development of an advanced microfluidic micropipette aspiration device for single cell mechanics studies. ***Biomicrofluidics.*** **10** (5), 054105 (2016).

18.Weaver, W. M. et al. Advances in high-throughput single-cell microtechnologies. ***Current Opinion in Biotechnology.*** **25**, 114-123 (2014).

19.Zhou, E. H., Lim, C. T., Quek, S. T. Finite element simulation of the micropipette aspiration of a living cell undergoing large viscoelastic deformation. ***Mechanics of Advanced Materials and Structures.*** **12** (6), 501-512 (2005).

20.Oh, M.-J., Kuhr, F., Byfield, F., Levitan, I. Micropipette aspiration of substrate-attached cells to estimate cell stiffness. ***Journal of Visualized Experiments.*** (67), e3886 (2012).

21.Rand, R. P., Burton, A. C. Mechanical properties of the red cell membrane. ***Biophysical journal.*** **4** (4), 303-316 (1964).

22.Hogan, B., Babataheri, A., Hwang, Y., Barakat, A. I., Husson, J. Characterizing cell adhesion by using micropipette aspiration. ***Biophysical Journal.*** **109** (2), 209-219 (2015).

23.Henriksen, J. R., Ipsen, J. H. Measurement of membrane elasticity by micro-pipette aspiration. ***The European Physical Journal E.*** **14** (2), 149-167 (2004).

24.Hochmuth, R. M. Micropipette aspiration of living cells. ***Journal of Biomechanics.*** **33** (1), 15-22 (2000).

25.Pu, H. et al. Micropipette aspiration of single cells for both mechanical and electrical characterization. ***IEEE Transactions on Biomedical Engineering.*** **66** (11), 3185-3191 (2019).

26.Guevorkian, K., Maître, J.-L. Chapter 10 - Micropipette aspiration: A unique tool for exploring cell and tissue mechanics in vivo. ***Methods in Cell Biology.*** **139**, 187-201 (2017).

27.Biro, M., Maître, J.-L. Chapter 14 - Dual pipette aspiration: A unique tool for studying intercellular adhesion. ***Methods in Cell Biology.*** **125**, 255-267 (2015).

Chapter 3: Establishing the Acoustics Force-Based Cell Avidity Analyzer

3.1. Introduction

With regard to the literature review presented in Chapter 2, the study of cellular interactions and their subsequent response to mechanical stimuli can elucidate the fundamental characteristics of cells. By understanding the cellular communication within cells' microenvironments, it gives rise to the advancements of vital therapeutics across a range of diseases – this is particularly critical and necessary for the complex malady known as cancer [148]. Due to the limitations of current technology confining researchers' knowledge of the tumour microenvironment (TME) and the intricate cellular communication that occurs within, efforts to fully uncover the underlying mechanisms of cancer continues to be hindered.

During the process of metastasis, where the primary tumour spreads to other areas of the body, tumour cells not only interact among themselves but also interact with a variety of non-cancerous host cells, such as endothelial cells, fibroblasts, and immune cells [149]. For example, during the early stages of metastasis, tumour cells will transmit signals to promote angiogenesis, the formation of new blood vessels, to sustain the tumour with nutrients and oxygen [150]. Additionally, tumour cells also respond to factors such as cytokines, growth factors, and ECM proteins. Within the TME, cell adhesion to ECM proteins, assisted by integrin receptors, is fundamental for tumour cell invasion and metastasis [151]. Such cellular interactions have the capacity for general indication of the metastatic potential for certain cancer types.

Currently, there are several established model systems that have been implemented to study the affinity of cell-cell and cell-matrix interactions, including optical tweezers [13] and traditional wash assays [14]. Although these applications can distinguish key components during the cell adhesion process, they are known to be non-standardised and substantially manually operated. To address such limitations, this chapter introduces the emerging commercialised cell avidity analyser, z-Movi, to investigate cell-cell and cell-matrix interactions in high-throughput. Originally developed

for immunotherapeutic screening through measuring the avidity between T cells and a target tumour cell monolayer, the z-Movi application is also expanded to measure cell-ECM avidity [152], [153].

3.2. Publication of Method Paper for the z-Movi Application

Jasmine Jin is a leading author of the following publication, which forms the part of this thesis submitted for the examination for the Master of Philosophy. The corresponding author below provides their consent for the inclusion of the following publication in this thesis and accept the following candidate statement of contribution for this publication.

Biosensors: Wang Yao, Jin Jasmine, Wang Jerry Haoqing, Ju Lining Arnold Acoustic Force-Based Cell-Matrix Avidity Measurement in High Throughput. Biosensors (2023). DOI: https://doi.org/10.3390/bios13010095

Candidate contribution:

This is the method paper to elaborate and demonstrate the established novel high-throughput cell-matrix avidity measuring platform using z-Movi. Jasmine Jin led and performed the z-Movi experiments and data analysis. Data interpretation and related results incorporated in the manuscript was carried out by Jasmine Jin and other co-authors. Manuscript formatting and editing was performed by Jasmine Jin and other co-authors.

Corresponding Author	Signature	Date
Lining Arnold Ju		11/07/2025

biosensors

MDPI

Article

Acoustic Force-Based Cell–Matrix Avidity Measurement in High Throughput

Yao Wang [1], Jasmine Jin [1], Haoqing Jerry Wang [1,2] and Lining Arnold Ju [1,2,3,*]

[1] School of Biomedical Engineering, The University of Sydney, Darlington, NSW 2008, Australia
[2] Charles Perkins Centre, The University of Sydney, Camperdown, NSW 2006, Australia
[3] The University of Sydney Nano Institute (Sydney Nano), The University of Sydney, Camperdown, NSW 2006, Australia
* Correspondence: arnold.ju@sydney.edu.au; Tel.: +61-2-9351-7140

Abstract: Cancer cells interacting with the extracellular matrix (ECM) in the tumor microenvironment is pivotal for tumorigenesis, invasion, and metastasis. Cell–ECM adhesion has been intensively studied in cancer biology in the past decades to understand the molecular mechanisms underlying the adhesion events and extracellular mechanosensing, as well as develop therapeutic strategies targeting the cell adhesion molecules. Many methods have been established to measure the cell–ECM adhesion strength and correlate it with the metastatic potential of certain cancer types. However, those approaches are either low throughput, not quantitative, or with poor sensitivity and reproducibility. Herein, we developed a novel acoustic force spectroscopy based method to quantify the cell–ECM adhesion strength during adhesion maturation process using the emerging z-Movi® technology. This can be served as a fast, simple, and high-throughput platform for functional assessment of cell adhesion molecules in a highly predictive and reproducible manner.

Keywords: extracellular matrix; mechanobiology; acoustic force spectroscopy; integrin

check for updates

Citation: Wang, Y.; Jin, J.; Wang, H.J.; Ju, L.A. Acoustic Force-Based Cell–Matrix Avidity Measurement in High Throughput. *Biosensors* **2023**, *13*, 95. https://doi.org/10.3390/bios13010095

Received: 17 November 2022
Revised: 9 December 2022
Accepted: 21 December 2022
Published: 6 January 2023

1. Introduction

Cancer metastasis, where malignant cells spread from a primary site to distant organs in the body, is largely responsible for the mortality and morbidity of cancer [1]. After dissociating from the original tumor mass, metastatic cells migrate through the extracellular matrix (ECM) by reorganizing their attachment to the ECM with altered cell–ECM adhesion dynamics, and then invade through adjacent tissues and intravasate into the blood vessels [2]. These motile cells journey through the vascular circulation and extravasate via invading the vascular basement membrane and ECM again to ultimately attach at a new location and grow into the secondary tumor [2]. Therefore, tumor cells experience alterations in cell–cell and cell–ECM adhesion during various stages of cancer invasion and metastasis.

In the tumor microenvironment, integrin receptors mediate cell adhesion with ECM ligands (such as fibronectin or FN, laminin, collagen, and gelatin) [3,4]. Such interactions couple the extracellular environment to intracellular signals via the actin cytoskeleton, which enables cell responses to external stimuli in a coordinated manner and enhances cancer cell proliferation, migration, invasion, and metastasis [2,4–6]. The biophysical and biochemical cues from the tumor ECM modulates each one of the 'hallmarks of cancer', and defective mechanosensitivity and mechano-responsiveness of the cell–ECM interactions are often associated with metastasis progression [7–9]. Therefore, the cell–ECM adhesion strength or avidity has been considered as a general indication for the metastatic potential of tumor cells, which defines the aggressiveness of cancer cells [6,10,11]. Many cell-adhesion proteins have been proposed as potent targets for inhibiting cancer cell invasion and metastasis [6].

Existing techniques established to measure the cell–ECM avidity include fixed-cell imaging based in vitro adhesion seeding assays [12], micropipette-based adhesion frequency assays [13–15], optical tweezers-based traction force microscopy [16], as well as the conventional wash assays [17]. These model systems are able to identify key adhesion components and correlate with metastatic progression [12] thereafter providing invaluable insights into regulatory mechanisms. However, those methods are either low throughput, not quantitative, or with poor sensitivity and reproducibility [11,17]. In recent years, Engler et al. established a population-based adhesion assay using the spinning-disk shear to quantify the cell adhesion strength on fibronectin and correlate it with focal adhesion assembly. This method also captured the adhesion heterogeneity within the studied cell population [10,11]. However, this measuring system is a custom-built spinning-disk device, and the experimental operation is time-consuming, which requires relatively long sample preparation and processing time with multiple experimental steps. These aspects limit its application as a high-throughput screening system.

To this end, we established a user-friendly, high-throughput yet effective method to study cell–ECM interaction in vitro using the acoustic force-based z-Movi® cell–cell avidity analyzer (Figure 1A). This technology allows sample preparation and avidity testing to be performed within a few hours. It can determine avidities of up to 400 cell pairs in a single run within a few minutes with minimum cell damage and high sensitivity and generate instant statistically relevant data. The z-Movi has rapidly emerged to measure the bona fide avidity between a T cell and its target tumor cell, which determines the adhesive strength of immunological synapse formation and T cell activation [18–20]. Assessments of the cell avidity in vitro have been proven to accurately predict cellular responses in vivo and outcomes during immunotherapy and facilitate the selection of optimal immune cells (e.g., CAR-T or TCR-T cells, NK cells) to kill cancer [18–20]. Here, we optimized and repurposed the z-Movi technology, for the first time, to measure cell–ECM avidity (Figure 1B,C), particularly the cell avidity with FN as a showcase. This method can be served as a rapid, simple, and high-throughput screening platform for functional assessment of cell adhesion molecules and their interactions with the tumor microenvironment in a highly predictive and reproducible manner.

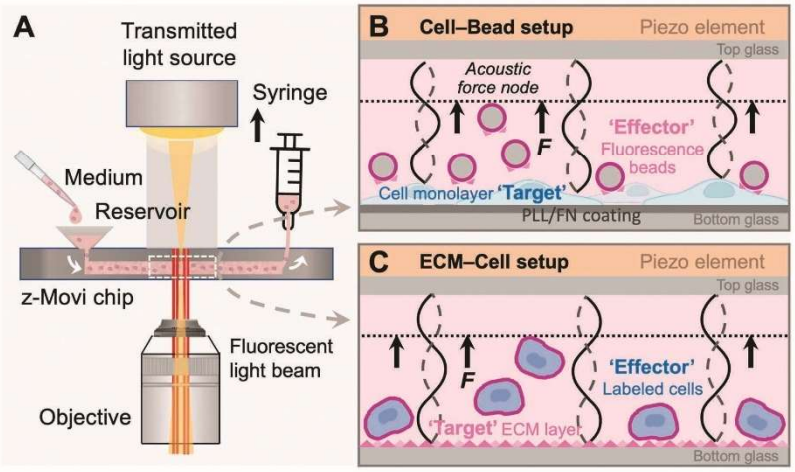

Figure 1. z-Movi working principle. (**A**) z-Movi utilizes a piezo-embedded microfluidic chip to perform the cell avidity measurement. The targets and effectors in the cell medium will be injected into the reservoir and then flushed into the flow chamber by pulling the syringe attached to the outlet

of the chip. The light path of the imaging platform will acquire both transmitted and fluorescent light through the objective simultaneously. The target cells or extracellular matrix (ECM) proteins were flushed in first and incubated in the flow chamber to form a monolayer. To form a monolayer of cells (**B**), the chip was pre-coated with fibronectin (FN) or poly-L-lysine (PLL), which promotes cell attachment. Otherwise, the flow chamber bottom surface was coated with ECM proteins via physical absorption (**C**). (**B**) Cell–Bead setup. After coating the flow chamber bottom glass with a monolayer of target cells, fluorescence beads coated with fibronectin were flushed in as effectors and incubated with the monolayer to form interactions. Then, the piezo element driven by the software generated a standing acoustic wave in the flow chambers and applied the lifting force to the effectors to the acoustic force node (dashed line). (**C**) ECM–Cell setup. Replacing fluorescent beads in the Cell–Bead layout, labelled effector cells were flushed into the flow chamber and formed interaction with the ECM protein monolayer.

2. Materials and Methods

2.1. Cell Culture

The human ovarian cancer cell line A2780 (ECACC 93112519) and human breast cancer cell line MCF-7 (ATCC HTB-22) were cultured in RPMI1640 medium (11875-119, Gibco, Waltham, MA, USA) supplemented with 10% fetal bovine serum (FBS; 10099141, Gibco), and kept in a humidified 37 °C incubator with 5% CO_2. All cell lines were negative for mycoplasma using real-time PCR-based screening.

2.2. Chip Glass Surface Coating with Poly-L-Lysine (PLL)

The chip needs to be cleaned and dried for at least 1 h at 37 °C before coating. The surface coating was carried out using 0.002% PLL (P4707, Sigma-Aldrich, Macquarie Park, NSW, Australian) in PBS (10010023, Thermo Fisher Scientific, Waltham, MA, USA). For each chip, 50 µL of fresh PLL solution was prepared and pulled into the microfluidic channel using a syringe (SS+03L1, Terumo Medical Canada Inc., Vaughan, ON, Canada) with 10 µL volume left in the reservoir to avoid bubble formation. After 15 min-incubation at room temperature, the PLL solution was completely removed using the syringe. The chip was pulled through with air several times to remove any remaining liquid in the microfluidic channel. The PLL-coated chips were kept in a dry incubator at 37 °C with a cap onto the reservoir (to avoid evaporation) for at least 1 h. The coated chips must be used within 3 days after coating. Upon cell seeding, the chips were rehydrated by pulling in 100 µL warm PBS into the microfluidic channel, leaving about 10 µL in the reservoir to avoid bubble formation. This step was repeated once with 100 µL warm complete cell culture medium.

2.3. Chip Glass Surface Coating with Fibronectin

The chip needs to be cleaned and dried for at least 1 h at 37 °C. For each chip, the glass surface was rehydrated by pulling in the following solutions to the microfluidic channel using a syringe (leave about 10 µL in the reservoir to avoid bubble formation): 200 µL 1M NaOH (incubation for 5 min), 400 µL Milli-Q water for two times, 400 µL 1 M HCl for two times (incubation for 2 min at the second time), 400 µL Milli-Q water for three times, and 400 µL PBS once. For each chip, 50 µL of 100 µg/mL fresh FN (F0895, Sigma-Aldrich) solution in PBS was pulled into the microfluidic channel with about 10 µL left in the reservoir. The inlet was washed with 400 µL PBS three times to prevent fiber or aggregate formation and re-filled with 200 µL PBS. Chips were caped firmly and kept in the 37 °C dry incubator overnight. Before cell seeding, the FN-coated chips were washed 3 times with PBS and once with the complete culture medium. The coated chips need to be used within 3 days after coating.

2.4. Target Cell Monolayer Formation

Target cells with at least 80% confluency were used for z-Movi experiments. Adherent cells were washed once with PBS and trypsinized using TrypLE (12605010, Thermo Fisher

Scientific) for 3–5 min at 37 °C. Cells were collected using the complete culture medium, and the cell density was determined using the automatic cell counter. For each chip, 20 µL of MCF-7 or A2780 cells at indicated densities were seeded into the microfluidic channel using a syringe (leave about 10 µL volume in the reservoir to avoid bubble formation). It is important to keep the chips and cells at 37 °C during cell seeding to reduce cell clumping. The inlet was washed with 400 µL complete medium three times and re-filled with 400 µL PBS. Chips were caped firmly and kept in the 37 °C dry incubator for a designated period (1-4 h, cell-line dependent) before z-Movi avidity assay.

2.5. Cell Viability Measurement of the Target Cell Monolayer

The viability of the cell monolayer was evaluated by adding 10 µL Trypan Blue (15250061, Thermo Fisher) in the reservoir containing 50 µL medium. The Trypan Blue dilution was pulled into the microfluidic channel and incubated with the monolayer cells for 30 s to stain the dead cell population, followed by 200 µL complete culture medium to rinse out Trypan Blue. The cell viability was observed by brightfield imaging.

2.6. Effector Cell Staining

Adherent cells were washed once with PBS and trypsinized using TrypLE for 3–5 min at 37 °C. Cells were collected using the complete culture medium, and the cell density was determined using the automatic cell counter. For a single run on the chip, 20 µL of 15×10^6 cells/mL (0.3×10^6 cells) was prepared. Cells were washed once with PBS and stained with the 1× CellTrace Far Red Dye (C34564, Thermo Fisher) dilution in PBS at 1×10^6 cells/mL in the dark at 37 °C for 15 min. Cells were re-suspended by pipetting every 5 min during the staining process. Approximal 5 mL complete culture medium was then added to the cell solution to stop the staining. Stained cells were washed once with PBS, re-suspended in complete culture medium at 15×10^6 cells/mL, and transferred into a 96-well plate with round bottom.

2.7. Effector Beads Coating with Fibronectin (FN)

The red-fluorescent melamine resin particles (MF-FluoRed-L840, microParticles GmbH, Berlin-Adlershof, Germany) were washed with 500 µL PBS three times and once with 500 µL complete culture medium. Beads were then incubated with FN at 10 µg/mL in 200 µL of completed culture medium for 1 h on a rotating stage at room temperature. FN-coated beads were washed three times with 500 µL complete medium and re-suspended in the complete medium (10 µL for a single run).

2.8. Cell Binding Avidity Measurement

The chip was placed on the z-Movi (LUMICKS B.V., Amsterdam, The Netherlands) stage, and the in-chip cell monolayer quality was evaluated and validated by applying force at 1000 pN for 10 s. Once the monolayer passed the validation, the medium level in the inlet was brought down to about 10 µL. 20 µL of stained effector cells were added into the reservoir and pulled into the microfluidic channel to interact with the target cell monolayer for a designated period. Depending on the effector density, up to 400 effectors that being considered as individual events will be incubated in the field of view (FOV) for the avidity measurement. During the incubation, the inlet was gently washed with complete culture medium three times to remove the remaining cells and refilled with 100 µL complete medium. After interaction, the acoustic force was applied with a linear force ramp from 0 to 1000 pN over 2.5 min. The percentage of bound cells to the monolayer under different levels of applied force was calculated simultaneously. To block FN binding with cancer cells, a FN antibody (MA5-11981, Thermo Fisher) was used. To block non-specific bindings, 2% BSA (A3311, Sigma-Aldrich) in complete culture medium was used.

2.9. Chip Cleaning

The cleaning solution containing 5% bleach (A1727, Sigma-Aldrich) was pulled into the microfluidic channel, and the chip was incubated at room temperature for at least 20 min and up to 4 h. The channel was then washed with 400 µL Milli-Q water and the glass surface was scrubbed by introducing air and moving the bubbles back and forth several times. The chip surface was scrubbed with 200 µL bleach twice, followed by pulling through (1) 400 µL bleach, (2) 400 µL Milli-Q water twice, (3) 100 µL 12M HCl (H1758, Sigma-Aldrich), and (4) 200 µL Milli-Q water twice. The surface was then scrubbed with 400 µL 1 M NaOH twice and incubated with 1 M NaOH for 1 h. After pulling through the NaOH solution, the surface was scrubbed with 200 µL 1 M NaOH twice, followed by washing with 400 µL Milli-Q water twice. Cleaned chips were stored in the dry incubator.

2.10. Avidity Data Analysis

The analysis of z-Movi data was performed offline by using Oceon 1.4.1 (LUMICKS B.V., Amsterdam, The Netherlands). Two-channel images were loaded into the software: (1) brightfield images which were used to examine the monolayer confluency and screen the effector events (Figure 2A, *left*); (2) fluorescence images were used to track the position of effectors (Figure 2A, *right*) and, thus, judge whether the effector was lifted. During the z-Movi application, the control software will move the field of view (FOV) to the force-calibrated region of the chip based on the information stored in the chip, while the software will capture both brightfield (monolayer tracking) and fluorescence (effectors tracking) signals within the FOV for the whole force application. The region of interest (ROI) for each effector is a 12 pixel-wide circle (with the cell as the center) by default. ROIs of up to 400 effectors within the FOV were identified by the software. Effectors left the ROIs while force application would be considered as 'lifted' and the software tracked all ROIs automatically. Manual selections were performed after software ROI selections (Figure 2B). Clustered effectors, effectors stuck on the glass, on the target cell clump, and under the acoustic force nodes were excluded from the analysis. In addition, effectors that escaped from the ROI but were not lifted (hinged effectors) were considered as attached effectors for the whole force application. After the manual selections, the software ran the automatic detection on lifted cells over the force ramp from 0–1000 pN (Figure 2C). Since the avidity curve would be dramatically different if no manual selection were performed (Figure 2D), we strongly recommended consistent manual selection over different runs of experiments.

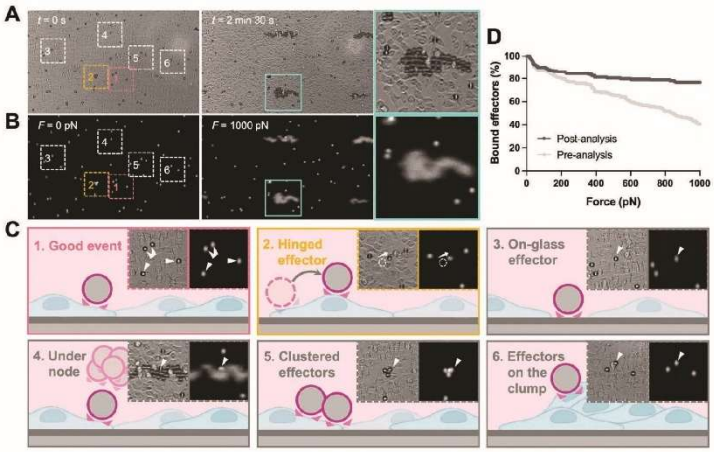

Figure 2. z-Movi image analysis and data selection criteria. z-Movi experiments acquired brightfield (**A**) and fluorescence (**B**) images during the force application. The brightfield images were used to

examine the confluency of the monolayer and guide the manual selection. The fluorescence images were used to track the effectors whether being lifted. Zoom-ins were the representative snapshots of selected cases. Of note, if the effector escaped from the region of interest (ROI) but was not lifted during the force application (hinged, 2), the selected effector was considered as attached. Additionally, when the effectors were located on the glass surface (3), under the force node (4), clustered (5), or laid on the target cell clumps (6), these events were excluded from the analysis. Besides the listed conditions, the event was considered as a good event (1) for further analysis. (**C**) During experiments, the z-Movi applied a constant acoustic force ramping, increasing the lifting force from 0–1000 pN in 2.5 min. The lifted effectors accumulated at the acoustic force node. (**D**) Comparison between Bound cells (%) vs. Force (pN) before and after the manual selection was calculated and shown. A significant difference was seen after applying manual selection criteria. Thereby, consistent manual selection criteria are required across all runs during analysis.

2.11. Statistical Analysis

Unpaired two-tailed Student's *t* test was performed in Prism 9 for the measurement of statistical significance. $p < 0.05$ was considered statistically significant. All data points with error bars are presented as mean ± standard error of the mean (S.E.M).

3. Results

3.1. Configuration of Acoustic Force-Based Measurement on Cell–ECM Adhesion

In the classic z-Movi® cell–cell experimental setup (Figure 1A), the 'Target' cells are placed at the bottom glass of a piezo-embedded microfluidic chip. The fluorescently labeled 'Effector' cells are then flushed into the chip to interact with the 'Targets' over a certain period at 37 °C. Upon measurement, the piezo element stuck to the top glass of the microfluidic channel via a thin layer of glue generated an acoustic pulling force to 'Effectors'. The element was driven by a function generator to excite a planar acoustic standing wave over the microfluidic channel [21], using forces ranging from 1 pN to 1000 pN to lift the 'Effector' to the acoustic force node. The z-Movi has a dual light path setup, allowing us to monitor the 'Target' with the transmitted light signal and track labelled 'Effectors' with the fluorescence light signal (Figure 1A). Moreover, the conversion factor for voltage amplitude in piezo to force is pre-calibrated by the manufacturer. The z-Movi® software controlled the voltage amplitude supplied to the piezo element, gradually increased the force applied to the stained 'Effectors' and tracked their movement in the fluorescence channel. The percentage of 'Effectors' still bound or being lifted was enumerated over forces to indicate the level of Target–Effector avidity (Figure 2A,B,D).

In this study, repurposing the z-Movi to measure cell–ECM avidity, we developed two novel configurations to measure the cancer cell adhesion on the specific ECM component, fibronectin. For the first one, we seeded the breast cancer cells MCF-7 or ovarian cancer cells A2780 in monolayer as the 'Targets' and used red-fluorescent melamine resin particles coated with FN (i.e., FN-beads) as the 'Effectors' (*Cell–Bead setup*; Figure 1B). This Cell–Bead setup enabled us to determine the FN-dependent adhesion of tumor cells that have already spread out and formed a structural organization to mimic the late stage of firm adhesion.

In the second configuration, we formed a thin layer of FN protein as the 'Target' on the glass bottom and stained the MCF-7 or A2780 cells with the CellTrace Far Red Dye as the 'Effectors' (*ECM–Cell setup*, Figure 1C). In this ECM–Cell setup, the effector cells were in suspension when flushed into the flow chamber. Cells contacted the ECM substrate (i.e., FN) with loose attachment, followed by flattening, and cell membrane spreading over the substrate surface [22]. During this process, cells establish focal adhesions that firmly anchor on the FN matrix, and cell spreading is driven by actin polymerization and myosin contraction that push the cell membrane forward [23]. Therefore, this configuration allowed us to capture the processes of adhesion maturation from initial attachment (weak interaction during sedimentation), flattening (integrin bonding during cell attachment),

to fully spreading (stable focal adhesion) [22] via increasing the incubation time for the suspended tumor cells interacting with the ECM layer.

3.2. Optimization of Target Cell Monolayer Formation

3.2.1. Chip Surface Coating for Cell Adhesion

To make a stable monolayer of solid tumor cells (i.e., MCF-7 and A2780 cells) on the glass surface of the chip, FN and poly-L-lysine (PLL) were used. Specifically, PLL enhances the electrostatic interaction between negatively charged ions of the cell membrane and the culture surface. Such a reaction caused the cells firmly attached to the chip surface after incubation for 2 h, which was validated using the acoustic force (Figure 3C). In comparison, coating with FN for 1 h has already enabled firm attachment of cells in the chip (Figure 3B), which is more efficient than PLL.

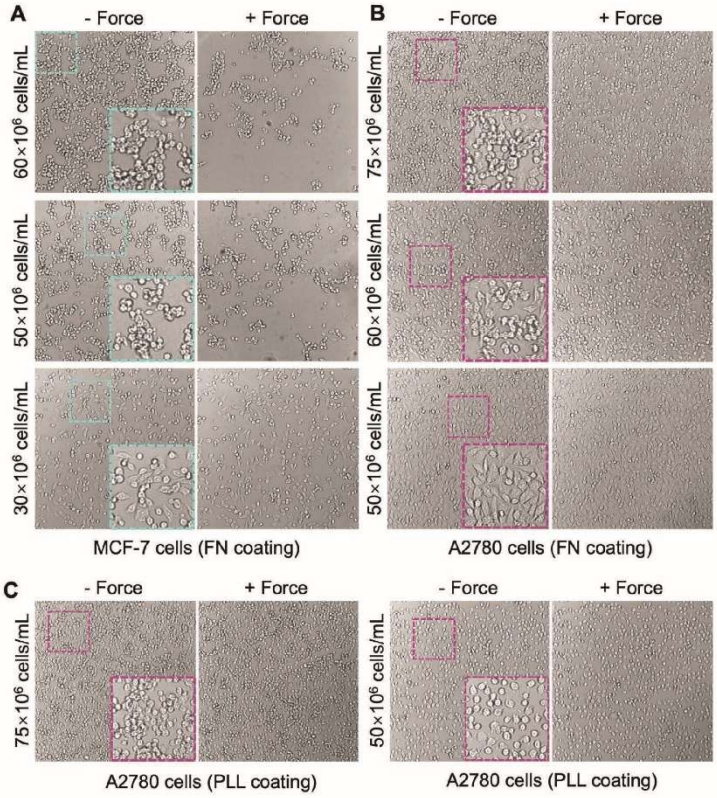

Figure 3. Monolayer cell seeding. MCF-7 cells (**A**) and A2780 cells (**B**) were seeded in the flow chamber at multiple density from 30×10^6 to 75×10^6 cells/mL to make the monolayer. The glass surface of the flow chamber was pre-coated with FN to enhance cell attachment. Representative images of the monolayer (at each seeding condition) after 2 h incubation at 37 °C (i.e., −Force) and then validation using acoustic force (i.e., +Force) were shown. After validation, weakly adhered cells were lifted from the coated surface and washed out using complete medium. (**C**) PLL coating was also tested to make A2780 cell monolayer at 75×10^6 (*left*) or 50×10^6 cells/mL (*right*) seeding density. Representative images of the monolayer after 2 h incubation with (+Force) or without (−Force) validation were shown. Insert: the zoom-in images showing the confluency of cell monolayer and the cell morphology.

Dissociating adherent cells from the surface of plastic culturing flasks using TrypLE caused morphological changes from flattened to round shapes. After incubation on the PLL surface for 2–4 h, most cells remained round morphology with gaps between cells (Figure 3C). On the other hand, as a ubiquitous ECM glycoprotein, FN promotes cell adhesion and spreading. It largely improved the recovery of cell morphology from trypsinization. After incubation on FN for one hour, most of the cells became flattened with less empty surface space (Figure 3B), indicating a faster spreading rate as compared with that on the PLL coating. Thus, FN coating is recommended for cell seeding in the chip.

Notably, in the Cell–Bead setup, we only included the adhesion events of FN-coated beads interacting with cells for data analysis and excluded the events where beads landed on the cell-free surface (Figure 2). Therefore, the FN (serves as 'glue') used for cell monolayer seeding has no impact on the adhesion measurement between tumor cells and the FN ('Effector') coated on the beads.

3.2.2. Monolayer Cell Seeding

To generate a target cell monolayer with high confluency (at least 70%), an extremely high cell seeding density (50×10^6 to 75×10^6 cells/mL) is required. A2780 cells were seeded at multiple densities to determine the best condition for forming a good monolayer with minimal cell–cell gaps and maximal cell population firmly attached to the chip surface. The density of 50×10^6 cells/mL produced the optimal monolayer with majority of cells spreading out and covering most of the chip surface after 1 h incubation at 37 °C (Figure 3B). Cell adhesion on the FN coating was strong enough to maintain the monolayer after the validation (Figure 3B, +Force). Increasing the seeding density to 60×10^6 or 75×10^6 cells/mL resulted in an obvious clumping issue, where a significant number of cell clumps formed on top of the cell monolayer (Figure 3B, −Force). The clumped cells hardly spread out even after 4 h incubation and were easily lifted by the acoustic force. However, they were hard to be removed by washing with medium due to their link with the monolayer cells that firmly adhered on the surface (Figure 3B, +Force), leading to a partial multi-layer that is not suitable for the avidity measurement.

During the preparation of suspension cell solution for monolayer seeding, some solid tumor cell lines such as MCF-7 cells are particularly prone to clumping after trypsinization. Moreover, because of the extremely high cell density required for monolayer seeding (i.e., $50–75 \times 10^6$ cells/mL), the clumping issue became exacerbated. Indeed, after loading the MCF-7 cells into the chip at a density of 60×10^6 or 50×10^6 cells/mL, significant clumping was observed within 2–5 min, leading to large empty surfaces between clumps. Once cells clumped, they hardly spread out on the surface even with FN coating. Indeed, most of MCF-7 cells (after 2 h incubation) were lifted when the acoustic force was applied to validate the monolayer (Figure 3A, *top* and *middle*). Overnight incubation (16 h) with FN coating at 37 °C was not feasible due to the intensive cell death induced by the sealed culturing environment without CO_2 and O_2 exchange. Decreasing the seeding density to 30×10^6 cells/mL effectively reduced the clumping rate and level (Figure 3A, *bottom*), with an increased number of MCF-7 cells spreading out and firmly attached to the chip surface. However, it also led to low seeding confluency. Although the gaps between spreading cells were small, a certain number of 'Effectors' will land on and interact with the surface coating (not the monolayer cells), which must be carefully identified and excluded during data analysis (Figure 2C).

To improve the seeding confluency while minimizing cell clumping, a multi-seeding strategy was conducted. MCF-7 cells at 20×10^6 cells/mL density were loaded into the z-Movi chip with FN coating and incubated for 15 min at 37 °C. Cell seeding with a density of 20×10^6 or 10×10^6 cells/mL was then repeated one to three more times under the same condition to achieve a final density equivalent to 60×10^6 (Figure 4A,B) or 70×10^6 cells/mL (Figure 4C). As shown in Figure 4, the monolayer after two rounds of seeding ($20 \times 10^6 + 20 \times 10^6$ cells/mL) exhibited an increased confluency with similar levels of cell spreading on the surface as compared to one-time seeding at 30×10^6 cells/mL (Figure 3A).

Additional seeding with either 20×10^6 or 10×10^6 cells/mL further promote the confluency of the monolayer but with noticeable cell clumping incidence. Although the clumping level is less than the one that occurred when seeding at 50×10^6 or 60×10^6 cells/mL (Figure 3A), clumped cells were hardly spreading out and failed to firmly adhere on the surface, which is not suitable for avidity measurement.

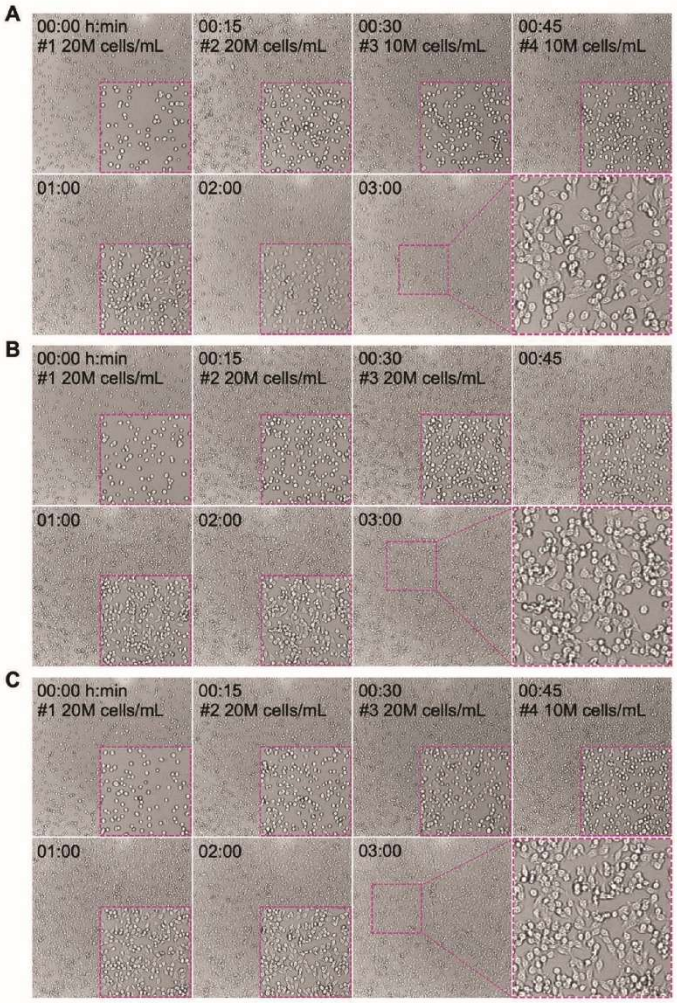

Figure 4. Seeding optimization to achieve target monolayer without clumpy cells. MCF-7 cells are highly clumpy at high seeding concentrations. Multiple rounds of cells seeding with low cell density were performed to avoid cell clumping. Three seeding procedures were conducted: (**A**) 20×10^6 cells/mL seeding for two times followed by two times at 10×10^6 cells/mL; (**B**) 20×10^6 cells/mL seeding for three times; (**C**) 20×10^6 cells/mL seeding for three times followed by additional seeding at 10×10^6 cells/mL. The interval time was 15 min. The monolayer condition for each seeding procedures at indicated time points was imaged and presented. Insert: the zoom-in images showing the confluency of cell monolayer and the cell morphology.

3.3. Avidity Measurement of Tumor Cell Monolayer Interacting with ECM Proteins

We then used the optimized monolayer of A2780 cells as proof of concept for cell–ECM avidity measurement (i.e., *Cell–Bead setup* in Figure 1B). As an intriguing matrix component found in cancer, FN was studied as a showcase. FN (10 µg/mL) was coated on the red-fluorescent beads (FN-beads) as the effectors to interact with the A2780 cell monolayer. The interaction formed rapidly after 2.5 min incubation with strong avidity, where only 3% and 6.6% FN-beads were detached from the cell monolayer under the acoustic force at 200 pN and 1000 pN, respectively (Figure 5B). It is worth mentioning that 2% BSA was added into complete medium to block the non-specific binding during avidity measurement. However, the avidity levels were similar with or without 2% BSA (Figure 5). When inhibiting FN–cell binding using an antibody specific to FN the avidity decreased in a dose-dependent manner (Figure 5C). Indeed, treatment with FN antibody (1:100 dilution) enhanced the detachment of FN-beads from 3% to 12.5% at 200 pN and 6% to 22% at 1000 pN. Increasing the concentration of FN antibody (1:50 dilution) further inhibited the interaction with 37.6% detachment at 200 pN and 51% at 1000 pN.

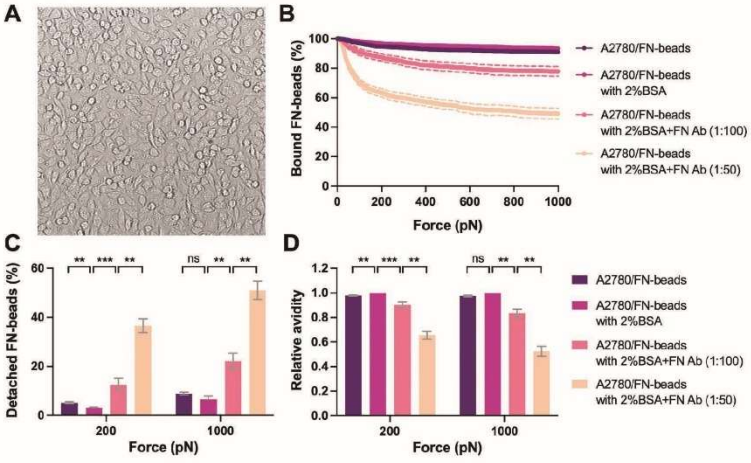

Figure 5. Avidity measurement of tumor cell monolayer interacting with ECM coated beads. (**A**) A2780 cells were seeded at the density of 50×10^6 cells/mL. A stable monolayer was formed after 1 hr incubation at 37 °C. After validation the monolayer was used as the 'Target'. The representative image of the monolayer was shown. FN proteins were coated on the beads as the 'Effector'. 2% BSA was used in the complete medium to block the non-specific binding. The FN antibody was used to treat the FN-beads at 1:100 or 1:50 dilutions for 1 h to block its interaction with the 'Target'. The 'Effectors' pre-treated with indicated conditions were flushed into the flow chamber and interacted with the 'Targets' for 2.5 min before the acoustic force was applied. (**B**) The percentage of 'Effectors' bound to 'Targets' under the force from 0 to 1000 pN was measured and analyzed to indicate the avidity. (**C**) The percentage of detached 'Effectors' under each treatment conditions at 200 pN and 1000 pN of force was plotted. (**D**) The avidity relative to that of A2780/FN-beads with 2% BSA was calculated and presented. Data were collected from at least three independent experiments. Error bars are mean ± S.E.M.; ns = not significant; ** $p < 0.01$; *** $p < 0.001$, assessed by unpaired two-tailed Student's *t* test.

3.4. Avidity Measurement of ECM Protein Layer Interacting with Tumor Cells

We next performed the cell–ECM avidity measurement (Figure 1C). To visualize the effector cells during the avidity measurement, A2780 and MCF-7 cells were stained with the CellTrace™ Far Red dye. The ECM protein FN was coated on the glass surface (50 µg/mL) and incubated with stained cancer cells for 2.5 to 15 min before the avidity

measurement. We observed that A2780 cells (Figure 6A) exhibited significantly higher avidity with FN than MCF-7 cells (Figure 6C). For example, after incubation for 5 min, 11–14% of A2780 cells were detached from the FN layer at 200–1000 pN (Figure 6B,F), versus 62-71% for MCF-7 cells (Figure 6D,F). A similar trend was observed with the avidity measurements after 7.5 min and 2.5 min incubation (Figure 6E,G). Moreover, to achieve the same level of avidity (e.g., 40% detached cells at 1000 pN) A2780 required a shorter interacting duration than MCF-7 (e.g., 2.6 min versus 12.5 min). Additionally, four runs of experiments were conducted for each z-Movi chip. Notably, the avidity of the Cell-ECM interaction measured during the first runs was always significantly higher than that determined via the other three runs, which produced more consistent results (Figure 6A–D). For better reproducibility, we established a protocol by excluding the data from the first runs for each chip. Taken together, these observations indicate that different cancer types exhibit substantially different cell-adhesion capacities to the ECM.

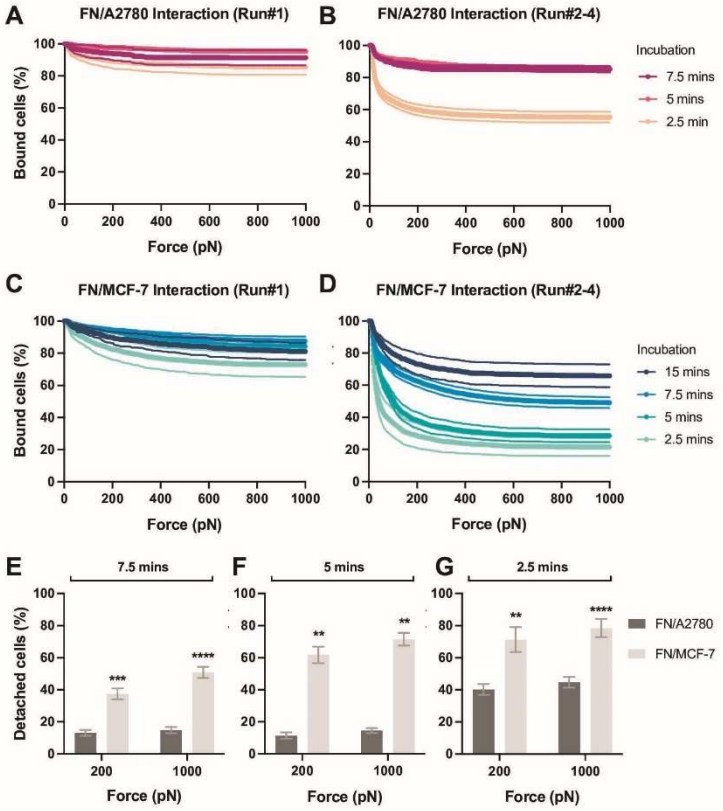

Figure 6. Avidity measurement of ECM protein layer interacting with tumor cells. FN protein was coated on the flow chamber surface at 50 µg/mL as the protein monolayer ('Target'). A2780 or MCF-7 cells pre-stained with the CellTrace™ Far Red dye were flushed into the flow chamber as the 'Effectors' and incubated with the FN monolayer for 2.5 to 15 min before the acoustic force was applied. The percentage of effector cells bound to FN under the force from 0 to 1000 pN was measured and analyzed to indicate the avidity. The data from the first runs of each chips using (**A**) A2780 or

(**C**) MCF-7 cells was shown. The data generated from the second to fourth runs in each chip using (**B**) A2780 or (**D**) MCF-7 cells was presented. After incubation for (**E**) 7.5 min, (**F**) 5 min or (**G**) 2.5 min with FN monolayer, the percentage of detached effector cells at 200 pN and 1000 pN was plotted for each cell lines. Data were collected from at least three independent experiments. Error bars are mean ± S.E.M.; ns = not significant; ** $p < 0.01$; *** $p < 0.001$, **** $p < 0.0001$, assessed by unpaired two-tailed Student's *t* test.

4. Conclusions

In brief, we have established a novel high-throughput measuring platform using the emerging acoustic force-dependent z-Movi technology to determine the adhesion strength of different types of cancer cells on ECM in vitro. This robust and highly maneuverable method will offer a rapid and simple solution to perform predictive, reproducible, and fast characterization of bona fide interactions between tumor cells and ECM components. More importantly, z-Movi allows us to capture early adhesion events and quantitate the adhesion strength from the initial cell attachment, flattening, to fully spreading on ECM, which cannot be achieved by traditional methods. Furthermore, given that acoustic force causes minimal damage to live cells, this system is suitable for studying fragile cells like primary patient samples and cancer stem cells, regardless of the tumor types. Although the experimental setup is designed for in vitro testing, the adhesion strength quantified by z-Movi serves as a general marker to predict the metastatic potential of the cancer cells *in vivo*. Moreover, by measuring the avidity of hundreds of 'Target–Effector' pairs in parallel with minimum cell damage with high sensitivity, this method is of great potential for preclinical drug screening to identify new candidates with potential anti-metastatic properties in a high-throughput manner.

Author Contributions: Conceptualization, Y.W. and L.A.J.; methodology, Y.W. and J.J.; software, H.J.W.; validation, Y.W. and J.J.; formal analysis, Y.W. and J.J.; investigation, Y.W. and J.J.; resources, Y.W. and L.A.J.; data curation, Y.W. and L.A.J.; writing—original draft preparation, Y.W. and H.J.W.; writing—review and editing, L.A.J., Y.W. and H.J.W.; visualization, Y.W. and L.A.J.; supervision, Y.W. and L.A.J.; project administration, Y.W. and L.A.J.; funding acquisition, L.A.J. All authors have read and agreed to the published version of the manuscript.

Funding: This research was funded by the Sydney Cancer Institute Seed Grant—Y.W.; Australian Research Council (ARC) Discovery Project, grant number DP200101970—L.A.J.; the National Health and Medical Research Council (NHMRC) of Australia Ideas Grant, grant number APP2003904—L.A.J.; NHMRC Equipment Grant—L.A.J.; NSW Cardiovascular Capacity Building Program, Early-Mid Career Researcher Grant—L.A.J.; Sydney Nano Grand Challenge Funding—L.A.J.; NSW CVRN-VCCRI Research Innovation Grant and Ramaciotti Foundations Health Investment Grant, grant number 2020HIG76—L.A.J.; Office of Global and Research Engagement Sydney-Glasgow Partnership Collaboration Award—L.A.J.; Tour de Cure Annual Grant, grant number RSP-391-FY2023—L.A.J. and Y.W. L.A.J. is an Heart Foundation Future Leader Fellow Level 2 (105863) and AMP Tomorrow Maker.

Institutional Review Board Statement: Not applicable.

Informed Consent Statement: Not applicable.

Data Availability Statement: Data is contained within the article.

Acknowledgments: We thank Evy Sanders, Eugen Ostrofet, and Qing Frank Wang (LUMICKS B.V., Amsterdam, The Netherlands) for technical support on z-Movi experiments. We thank Yingqi Kaitlyn Zhang and Hongxu Lu for the helpful discussion. We also thank Hala Zreiqat for providing the initial lab space support for cell culture.

Conflicts of Interest: The authors declare no conflict of interest.

References

1. Martin, T.A.; Ye, L.; Sanders, A.J.; Lane, J.; Jiang, W.G. *Cancer Invasion and Metastasis: Molecular and Cellular Perspective*; Landes Bioscience: Austin, TX, USA, 2013.
2. Gkretsi, V.; Stylianopoulos, T. Cell Adhesion and Matrix Stiffness: Coordinating Cancer Cell Invasion and Metastasis. *Front. Oncol.* **2018**, *8*, 145. [CrossRef] [PubMed]
3. Humphries, J.-D.; Byron, A.; Humphries, M.-J. Integrin ligands at a glance. *J. Cell Sci.* **2006**, *119*, 3901–3903. [CrossRef] [PubMed]
4. Chen, Y.; Ju, L.; Rushdi, M.; Ge, C.; Zhu, C. Receptor-mediated cell mechanosensing. *Mol. Biol. Cell.* **2017**, *28*, 3134–3155. [CrossRef] [PubMed]
5. Chen, Y.; Li, Z.; Ju, L.-A. Tensile and compressive force regulation on cell mechanosensing. *Biophys. Rev.* **2019**, *11*, 311–318. [CrossRef]
6. Hynes, R.-O. Integrins: Bidirectional, allosteric signaling machines. *Cell* **2002**, *110*, 673–687. [CrossRef]
7. Pickup, M.-W.; Mouw, J.-K.; Weaver, V.-M. The extracellular matrix modulates the hallmarks of cancer. *EMBO Rep.* **2014**, *15*, 1243–1253. [CrossRef]
8. Cooper, J.; Giancotti, F.-G. Integrin Signaling in Cancer: Mechanotransduction, Stemness, Epithelial Plasticity, and Therapeutic Resistance. *Cancer Cell* **2019**, *35*, 347–367. [CrossRef]
9. Hamidi, H.; Ivaska, J. Every step of the way: Integrins in cancer progression and metastasis. *Nat. Rev. Cancer* **2018**, *18*, 533–548. [CrossRef]
10. Fuhrmann, A.; Banisadr, A.; Beri, P.; Tlsty, T.-D.; Engler, A.-J. Metastatic State of Cancer Cells May Be Indicated by Adhesion Strength. *Biophys. J.* **2017**, *112*, 736–745. [CrossRef]
11. Beri, P.; Popravko, A.; Yeoman, B.; Kumar, A.; Chen, K.; Hodzic, E.; Chiang, A.; Banisadr, A.; Placone, J.-K.; Carter, H.; et al. Cell Adhesiveness Serves as a Biophysical Marker for Metastatic Potential. *Cancer Res.* **2020**, *80*, 901–911. [CrossRef]
12. Reticker-Flynn, N.-E.; Malta, D.-F.; Winslow, M.-M.; Lamar, J.-M.; Xu, M.-J.; Underhill, G.-H.; Hynes, R.-O.; Jacks, T.-E.; Bhatia, S.-N. A combinatorial extracellular matrix platform identifies cell-extracellular matrix interactions that correlate with metastasis. *Nat. Commun.* **2012**, *3*, 1122. [CrossRef] [PubMed]
13. Palmer, C.-P.; Mycielska, M.-E.; Burcu, H.; Osman, K.; Collins, T.; Beckerman, R.; Perrett, R.; Johnson, H.; Aydar, E.; Djamgoz, M.-B. Single cell adhesion measuring apparatus (SCAMA): Application to cancer cell lines of different metastatic potential and voltage-gated Na+ channel expression. *Eur. Biophys. J.* **2008**, *37*, 359–368. [CrossRef] [PubMed]
14. Chen, Y.; Ju, L.-A.; Zhou, F.; Liao, J.; Xue, L.; Su, Q.-P.; Jin, D.; Yuan, Y.; Lu, H.; Jackson, S.-P.; et al. An integrin αIIbβ3 intermediate affinity state mediates biomechanical platelet aggregation. *Nat. Mater.* **2019**, *18*, 760–769. [CrossRef]
15. Wang, H.; Zhou, F.; Guo, Y.; Ju, L.-A. Micropipette-based biomechanical nanotools on living cells. *Eur. Biophys. J.* **2022**, *51*, 119–133. [CrossRef]
16. Zhou, Z.-L.; Ma, J.; Tong, M.-H.; Chan, B.-P.; Wong, A.-S.; Ngan, A.-H. Nanomechanical measurement of adhesion and migration of leukemia cells with phorbol 12-myristate 13-acetate treatment. *Int. J. Nanomed.* **2016**, *11*, 6533–6545. [CrossRef] [PubMed]
17. Garcia, A.-J.; Gallant, N.-D. Stick and grip: Measurement systems and quantitative analyses of integrin-mediated cell adhesion strength. *Cell Biochem. Biophys.* **2003**, *39*, 61–73. [CrossRef] [PubMed]
18. Balneger, N.; Cornelissen, L.-A.-M.; Wassink, M.; Moons, S.-J.; Boltje, T.-J.; Bar-Ephraim, Y.-E.; Das, K.-K.; Søndergaard, J.-N.; Büll, C.; Adema, G.-J. Sialic acid blockade in dendritic cells enhances CD8(+) T cell responses by facilitating high-avidity interactions. *Cell. Mol. Life Sci.* **2022**, *79*, 98. [CrossRef] [PubMed]
19. Katsarou, A.; Sjöstrand, M.; Naik, J.; Mansilla-Soto, J.; Kefala, D.; Kladis, G.; Nianias, A.; Ruiter, R.; Poels, R.; Sarkar, I.; et al. Combining a CAR and a chimeric costimulatory receptor enhances T cell sensitivity to low antigen density and promotes persistence. *Sci. Transl. Med.* **2021**, *13*, eabh1962. [CrossRef]
20. Leick, M.-B.; Silva, H.; Scarfò, I.; Larson, R.; Choi, B.-D.; Bouffard, A.-A.; Gallagher, K.; Schmidts, A.; Bailey, S.-R.; Kann, M.-C.; et al. Non-cleavable hinge enhances avidity and expansion of CAR-T cells for acute myeloid leukemia. *Cancer Cell* **2022**, *40*, 494–508.e5. [CrossRef]
21. Sitters, G.; Kamsma, D.; Thalhammer, G.; Ritsch-Marte, M.; Peterman, E.-J.; Wuite, G.-J. Acoustic force spectroscopy. *Nat. Methods* **2015**, *12*, 47–50. [CrossRef]
22. Khalili, A.-A.; Ahmad, M.-R. A Review of Cell Adhesion Studies for Biomedical and Biological Applications. *Int. J. Mol. Sci.* **2015**, *16*, 18149–18184. [CrossRef] [PubMed]
23. McGrath, J.-L. Cell spreading: The power to simplify. *Curr. Biol.* **2007**, *17*, R357–R358. [CrossRef] [PubMed]

3.3. Leveraging CD19 Chimeric Antigen Receptor (CAR) for Solid Tumor Treatment via a Novel Adaptor Approach

The following sections include a collaborative manuscript with Dr. Clare Slaney from Peter MacCallum Cancer Institute, Melbourne and forms part of this thesis submitted for the examination for the Master of Philosophy. The presented z-Movi work, and data analysis was performed by Jasmine Jin. All relevant sections have been rewritten by Jasmine Jin.

Section 3.3. introduces an application of the z-Movi technology to investigate cell-cell interactions. It will detail the key findings and data collection through implementation of the Cell-Bead setup, replacing the matrix-coated glass bead with a cell, presented in Section 3.2., to investigate the different binding avidities for CD19 CAR T cells and HER2 CAR T cells to their target as well as the introduction to a novel adapter approach.

3.3.1. Introduction

With the development of more progressive cell therapies, in particular chimeric antigen receptor (CAR) T cell treatments, there is a rise in the clinical application of such therapies to treat cancer. In general, CAR T cell therapy refers to the process in which a clinical patient's T cells undergo genetic modification to express CAR. This enables the modified T cells to identify cancer antigens and moderate anti-cancer cytotoxicity. There are currently seven CAR T cell therapies sanctioned by the US Food and Drug Administration (FDA) which are designed for hematologic cancer, including five therapies that specifically target CD19 which is known as a B-cell lineage marker and two therapies that target the B-cell maturation antigen (BCMA).

Although there has been significant clinical success for CAR T cell therapy, especially in B-cell tumours, there is a notable juxtaposition for solid malignancy treatment. To date, there have been several clinical studies implementing CAR T cell therapies to target solid tumours. However, despite the varying target antigens that have been clinically experimented, observations demonstrate low efficacy in targeting solid cancers [154]. This challenge can be potentially attributed to the multiplicity of cancer

antigens and the immunosuppressive tumour microenvironment (TME) [155]. It should be noted that both liquid and solid cancers have very different antigen expression, suggesting that the selection of the target antigen with its respective CAR is essential when determining the clinical efficacy of CAR T cell therapies between hematologic and solid malignancies. Although there have been a substantial number of clinical trials to investigate varying CAR-antigen pairs, this mechanism cannot be easily identified due to several factors such as the many cancer types and CAR backbones as well as the varying strategies in producing the CAR T cells. To bridge this gap, this study compares the efficacy of B-lymphocyte antigen CD19 (CD19)-CAR and human epidermal growth factor receptor 2 (HER2)-CAR to that of hematologic and solid malignancies. Additionally, this study introduces the potential of a novel anti-HER2 single chain variable fragment (scFv) adaptor for the treatment of solid tumours.

3.3.2. Avidity Measurements to Compare CD19-CAR and HER2-CAR T Cells Binding to Suspension and Solid Tumours

As the target tumour cells are paired with their identical CAR backbones, it is theorised that the reduced efficacy observed in CAR T cells targeting solid cancers is attributed to the interaction between the target antigen and corresponding CAR, potentially due to the various scFvs. Typically, affinity, which refers to the binding strength of an individual antibody to its antigen, is used with regard to CAR activity. However, to better understand the antigen and CAR interaction, investigating cellular avidity is preferred. By imitating the cell-bead configuration detailed in section 3.2, the matrix-coated fluorescent glass bead is replaced with an effector cell instead. To elaborate, this study uses CD19-CAR and HER2-CAR T cells as the stained effector cells and the respective target cells is the human B-cell precursor leukemia cell line, NALM6, and the M D Anderson–Metastatic Breast (MDA-MB)-468 cell line. Before beginning the assay, z-Movi microfluidic chips are pre-coated with 0.002% Poly-L-Lysine (PLL). The target cells are then seeded as a monolayer with approximately 95% surface coverage. The seeding density for the NALM6 monolayer is 180×10^6 cells/mL, whereas due to the cell size being larger for MDA-MB-468, the seeding density was set at 100×10^6 cells/mL. The monolayer is incubated for 2 hrs at 37 ˚C before introducing the respective effector CAR T cells which interact with the monolayer for 5 mins before the force application.

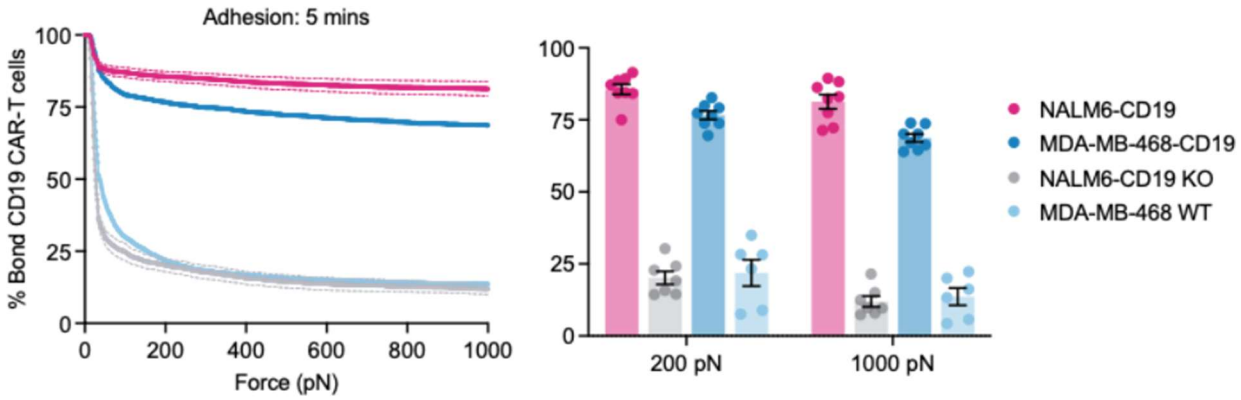

Figure 3.1. Avidity measurements to determine the efficacy of CD19-CAR T cells. An incubation of 5 mins with NALM6 and MDA-MB-468 expressing CD19 (positive controls) and NALM6-CD19KO and MDA-MB-468 WT (negative controls) was performed before a force ramp of 0 – 1000 pN was applied for 2.5 mins was applied. Avidity trends across 0 – 1000 pN for all four conditions (left) and percentage of cells bound at force points 200 pN and 1000 pN (right).

For the positive controls, CD19-CAR T effector cells interacted with both NALM6 and MDA-MB-468 expressing CD19 for an adhesion time point of 5 mins. From Figure 3.1, it is demonstrated that there is higher avidity between the CD19-CAR when bound to the hematologic cancer, NALM6, where approximately 20% of the total effector cell population was lifted from the monolayer at 1000 pN. Although the solid breast tumour cell line, MDA-MB-468, demonstrated relatively high avidity with approximately 30% effector cell detachment at 1000 pN when compared to NALM6, the observed trend was inferior. This decrease in avidity indicates that CD19-CAR T cells exhibit better binding to cancer cells that possess an innate expression of CD19. As NALM6 naturally expresses CD19, the isogenic derivative, NALM6-CD19 Knockout (KO) cell line was used for the negative control for blood tumour monolayer. In contrast, MDA-MB-468 does not inherently express CD19 and thus the parental MDA-MB-468 Wild Type (WT) cell line was used as a negative control to represent the solid tumour monolayer. As shown in Figure 3.1, when CD19-CAR T effector cells interact with NALM6-CD19 KO and MDA-MB-468 WT, the avidity significantly reduces, further validating the efficacy of the antigen/CAR interaction.

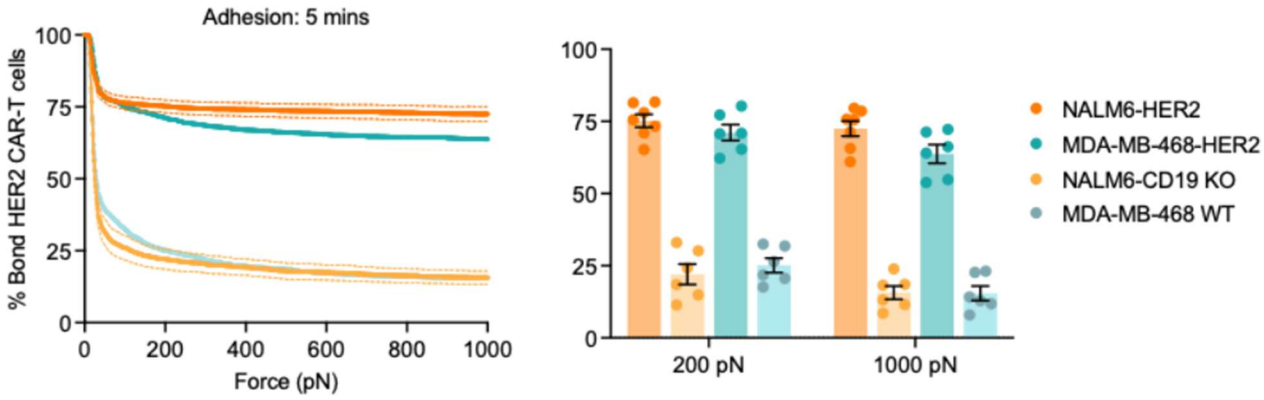

Figure 3.2. Avidity measurements to determine the efficacy of HER2-CAR T cells. An incubation of 5 mins with NALM6 and MDA-MB-468 expressing HER2 (positive controls) and NALM6-CD19KO and MDA-MB-468 WT (negative controls) was performed before a force ramp of 0 – 1000 pN was applied for 2.5 mins was applied. Avidity trends across 0 - 1000 pN for all four conditions (left) and percentage of cells bound at force points 200 pN and 1000 pN (right).

To compare the binding efficacy with CD19-CAR T cells, HER2-CAR T effector cells interacted with NALM6 and MDA-MB-468 expressing HER2 for the adhesion time point of 5 mins. Visualised in Figure 3.2, NALM6 exhibited slightly higher avidity with the HER2-CAR T cells where approximately 25% of the effector cell population detached from the target monolayer at 1000 pN. Although MDA-MB-468 demonstrates a lower avidity curve, the effector cell population that detached from the target monolayer was approximately 30% at 1000 pN. As NALM6 inherently expressed HER2, this can potentially explain the slight increase in avidity compared to the MDA-MB-468 which does not have an innate expression of HER2. Overall, CD19-CAR T cells displayed superior binding with higher avidity trends than HER2-CAR T cells during NALM6 and MDA-MB468 interactions with the corresponding antigen expression. For each time point, three runs of experiments were performed for a single z-Movi chip. The avidity trends presented incorporate data collected from three separate z-Movi chips in one day. This was repeated twice more on separate days.

3.3.3. Investigating the potential of an Anti-HER2 scFv adaptor to leverage CD19 CAR on solid tumour treatment

By repurposing the remarkable efficacy of the CD19-CAR T cells toward solid malignancies, complicated strategies the involve improving weaker CARs through further modification can be avoided. To divert the CD19-CAR T cells to target solid cancers which do not inherently express CD19, a recombinant bispecific protein adaptor, consisting of a

human CD19 extracellular domain (ECD) sequence fused to an anti-HER2 scFv, is used to redirect the CD19-CAR T cells to target solid cancers expressing the HER2 antigen.

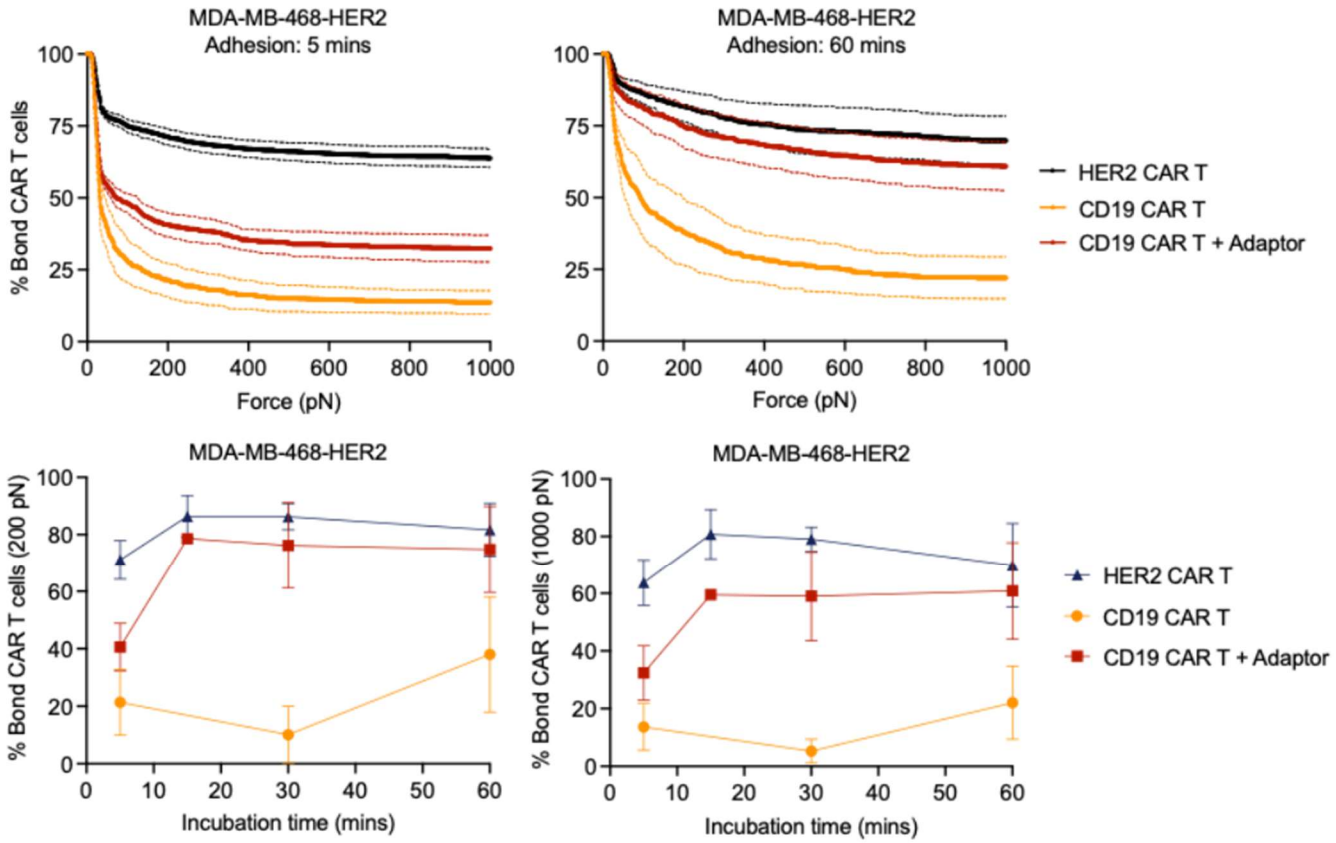

Figure 3.3 Avidity measurements to determine the efficacy of anti-HER2 scFv adaptor. CD19-CAR T cells were incubated with the adaptor for 30 min before introducing the CAR to the MDA-MB-468-HER2 monolayer. An incubation of 5, 15, 30, and 60 mins with MDA-MB-468 expressing HER2 (positive control) was performed before a force ramp of 0 – 1000 pN was applied for 2.5 mins was applied. Untreated CD19-CAR T cells were also used to perform the exact same condition as a negative control. The avidity of HER2-CAR T cells is included to provide better comparison on the efficiency of the adaptor. Avidity trends across 0 – 1000 pN for all three conditions at 5 mins (top left) and at 60 mins (top right). Percentage of cells bound at force points 200 pN (bottom left) and 1000 pN (bottom right) were visualised for all three conditions.

To test the efficacy of the anti-HER2 scFv adaptor in redirecting the CD19-CAR to target solid tumours, avidity measurements were taken between the target MDA-MB-468 expressing the HER2 antigen cell line interacting with the effector cell: HER2-CAR T cells, CD19-CAR T cells (Negative Control), and CD19-CAR T cells incubated with the anti-HER2 scFv adaptor (Positive Control). In top right of Figure 3.3, CD19-CAR T cells incubated for 60 mins with the adaptor demonstrated a significant increase in avidity where 35% of the effector cells detached at 1000 pN, when compared to the negative control, which is the CD19-CAR T cells only, where 85% of the effector cells detached at 1000 pN. It should be noted that by increasing the adaptor incubation period with the CD19-CAR T cells during

the adhesion interaction, the avidity significantly increases. Across the different time points, the avidity between MDA-MB-469-HER2 with CD19-CAR T cells incubated with the adaptor begins to closely follow the avidity trend of that with the HER2-CAR T cells after the 15 min adaptor incubation. For each time point, three runs of experiments were performed for a single z-Movi chip. The avidity trends presented incorporate data collected from three separate z-Movi chips in one day. This was repeated twice more on separate days.

3.3.4. Discussion

Typically, affinity has been the preferred indicator to determine CAR function with reference to the CAR-antigen interaction [156], [157], [158]. However, this has proven to be less reliable when discerning the original binding between the CAR and antigen. In contrast, avidity profiles use population studies to present the cumulative binding strength of CAR T cells against tumour cells, offering a more comprehensive valuation compared to affinity measurements. Regarding the technological advancement of the z-Movi instrument, the novel biophysical tool allows for high throughput screening to quantitatively compare cell-cell avidities at the single-cell level [159]. With the explicit measurement of cell-cell binding strengths, avidity profiles provide mechanical acuity into CAR T cell function.

The presented findings suggest that CD19-CAR T cells had a more effective overall binding capacity through higher avidity profile when compared to that of HER2-CAR T cells. Recent studies have revealed that by increasing the binding strength of both sides of the immunological synapse, it can result in higher avidity which improves the *in vivo* function of the CAR T cells [160]. Furthermore, a previously developed mathematical model representing the bivalent binding of CAR, showed that with higher avidity profiles, the amount of phosphorylated CAR also subsequently increases. This indicates that increased avidity extends the interactions between antigens and CAR, further improving the signaling potential of CAR T cells [161]. In juxtaposition, it was discovered that by engineering a CAR that binds to the BCMA and the transmembrane activator CAML interactor, the resulting *in vivo* efficacy is low. Although having comparable affinity to BCMA-CARs, this particular CAR exhibited reduced binding avidity which led to less interleukin (IL)-2 secretion and increase exhaustion [162]. These studies suggest that

measuring CAR T cell avidity through targeting tumour cells can be correlated to *in vivo* efficacy.

In conclusion, this study reveals that the CD19-CAR binding capacity far surpasses that of HER2-CAR within a regulated solid tumour model system. By leveraging the potent efficacy of CD19-CAR T cells, redirection to target HER2 expressing tumours through the introduction of the anti-HER2 scFv adaptor is possible.

3.4. Cell Avidity Regulation on Fibronectin via the Piezo1 Mechanosensitive Ion Channel

The following subsections introduce an application of the z-Movi technology to investigate cell-ECM interactions. It will detail the key findings and data collection through implementation of the ECM-cell setup, presented in Section 3.2., to investigate the role of Piezo1 during initial stages of the cell adhesion process.

3.4.1. Introduction

Cell adhesion is an important process involved in cellular regulation and intercellular communication. Cell adhesion essentially refers to the capacity of a cell to bind to either another cell or to the ECM [163]. As an essential mediator, cell adhesion governs several cellular processes including cell differentiation and migration. Fluctuations exhibited in the adhesive properties of cells to the ECM are indications of tumour cells and their predisposition to invade and metastasize [164], [165]. In general, the cell adhesion process involves three main stages: the initial attachment of the cell body to the substrate, flattening and spreading of the cell body, and the restructuring of the actin cytoskeleton resulting in the development of focal adhesions (FA) between the cell and substrate [166]. Cells, particularly tumour cells, are known to transduce mechanical stimuli into biochemical responses with the mechanically-gated ion channel, Piezo1. This mechanosensor is a crucial component of cells as it facilitates with sensing and generating mechanical forces. When the cation channel is activated by mechanical cues, cation translocation occurs where calcium ions enter the cell, subsequently inducing the mechanotransduction process and downstream signalling. It is susceptible to a diverse range of mechanical cues, that is, membrane stretch, shear flow, cell indentation,

substrate stiffness, and confinement. The subunits of the trimeric mechanosensitive calcium ion channel are constructed with Piezo1 proteins.

Piezo1 is known to be involved in the regulation of certain cellular functions such as protein synthesis, spreading, migration, proliferation, and apoptosis, in response to mechanical force. Previously, Piezo1 proteins have demonstrated co-localisation with FA complexes at the edges of spreading cells, suggesting a direct involvement in the cell adhesion process. As FA maturation is associated with perpetual traction forces, it has been suggested that Piezo1-adhesion interplay depend on force [167]. Studies have shown that with the inhibition of actomyosin contraction, a reduction of Piezo1 at adhesion sites before FA disassembly is observed. In contrast, Piezo1 enrichment is observed when the cell contractility is augmented through active RhoA, demonstrating that the recruitment of Piezo1 to adhesion sites is force-dependent [168], [169]. It has also been demonstrated that Piezo1 plays an important role in mature adhesion for normal cells and have little role in transformed or tumour cells. The following study presented aims to investigate the role of Piezo1 in transformed and tumour cells during the initial attachment stage.

3.4.2. Avidity Measurement of Different Piezo1 Expression Levels in Transformed Cells when Interacting with Fibronectin

Implementing the ECM-Cell setup detailed in Section 3.2., the ECM protein, fibronectin (FN), was coated at a concentration of 50 µg/mL, on the glass surface of a z-Movi microfluidic chip and incubated overnight for approximately 16 hrs. The effector cells used in the z-Movi assay included transformed Human Embryonic Kidney (HEK239T) cells with different Piezo1 expression levels, denoted as HEK293T Wild Type (WT), HEK293T Piezo1 Knockout (P1KO), HEK293T Piezo1 Overexpressed-Halo (P1OE). These effector cells were visualised on the z-Movi platform through the staining of the membrane with CellTrace™ Far Red dye. Before measuring the avidity, which is the collective binding strength of numerous bonds between cells and substrates, the stained effector cells were incubated to the FN coating for 2.5, 5 and 15 mins.

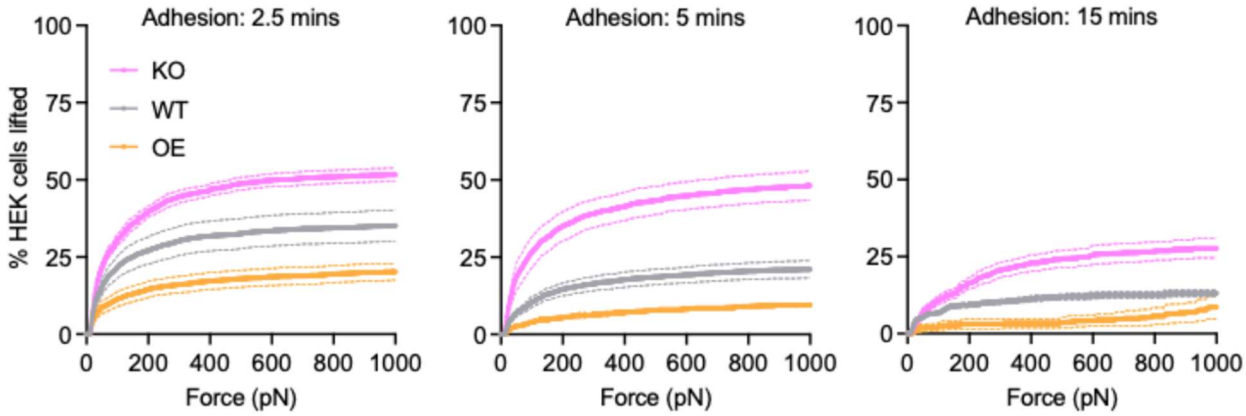

Figure 3.4. Avidity measurements of HEK293T WT, HEK293T P1KO, and HEK293T P1OE incubated on FN at time points: 2.5 (left), 5 (middle), and 15 mins (right). The presented trends represent the percentage of cells lifted across the applied force ramp of 0 – 1000 pN.

After the 0 – 1000 pN force ramp is applied, it is noted that HEK293T P1OE exhibited the highest overall binding avidity to FN with the percentage of cells lifted to be approximately 12% at 200 pN and 20% at 1000 pN for the adhesion time point, as shown in Figure 3.4 for 2.5 mins. Comparing this to HEK293T WT, the percentage of cells lifted was 27% at 200 pN and 35% at 1000 pN, demonstrating a decrease in avidity to FN. Overall, HEK293T P1KO had the lowest avidity to FN with the percentage of cells lifted to be 42% at 200 pN and 52% at 1000 pN. This trend is further reflected in the adhesion time points at 5 and 15 mins. For each time point, four runs of experiments were performed for a single z-Movi chip where the first data set is omitted due to an evident increase in avidity when compared to the remaining three runs. The avidity trends presented incorporate data collected from three separate z-Movi chips in one day. This was repeated twice more on separate days.

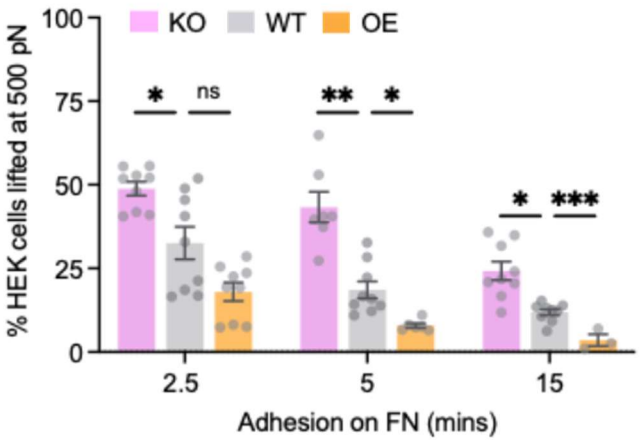

Figure 3.5. Avidity measurements of HEK293T WT, HEK293T P1KO, and HEK293T P1OE incubated on FN at time points: 2.5, 5, and 15 mins at the selected force point of 500 pN.

To better visualise the avidity differences across the three different Piezo1 expression levels, data points collected at the 500 pN force point was graphed across the three different adhesion times. Through the bar plot shown in Figure 3.5, it can be observed that HEK293T P1KO exhibited the lowest binding strength to FN, while HEK293T P1OE had the highest binding strength, and HEK293T WT served as the baseline between the two. The collective trend indicates that with the elimination of the Piezo1 construct in the HEK293T cells, the adhesion rate to FN is significantly slower during the initial attachment stage of the cell adhesion process. To further validate this, the Piezo1 inhibitor, Grammostola Mechanotoxin #4 (GsMTx4) was introduced to impede the Piezo1 function present in HEK293T WT. A dosage of 2.5 and 5 μM was used to drug treat the HEK293T WT cells for an incubation period of 20 mins. Before the force application, the adhesion time point was set at 2.5 mins as the untreated HEK293T WT cells already exhibited high binding avidity to the FN coating.

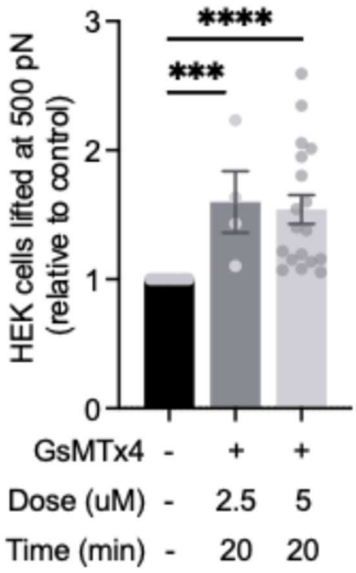

Figure 3.6. Avidity measurements at 500 pN of HEK293T WT drug treated with 2.5 and 5 μM of GsMTx4 to inhibit the Piezo1 function. HEK293T WT cells were treated for 20 mins before introduction to FN coating for 2.5 mins. Untreated HEK293T WT avidity measurements is included for comparison.

Relative to the control, which is the untreated HEK293T WT cells, the GsMTx4 treated HEK293T WT cells were normalised in Figure 3.6. By plotting the percentage of cell detachment at 500 pN for both the control and drug-treated cells, the visualised trend depicts an increase in cells lifted, indicating a reduction in the population binding to FN. To elaborate, by inhibiting the function of the Piezo1 in HEK293T WT, a comparable trend

to the HEK293T P1KO is observed, further reinforcing that Piezo1 plays a role in the initial attachment process. It should be highlighted that the initial Piezo1 expression level in HEK293T WT was already relatively low, which further demonstrates the significance of Piezo1 during the initial attachment phase.

3.4.3. Avidity Measurement of Different Piezo1 Expression Levels in Tumour Cells when Interacting with Fibronectin

To further investigate the role of Piezo1 in the initial attachment phase of the cell adhesion process, avidity measurements were taken of the breast tumour cell lines, Michigan Cancer Foundation-7 (MCF-7). With varying Piezo1 expression levels, these effector cells are denoted as MCF-7 WT and MCF-7 P1KO. By utilising the aforementioned ECM-Cell configuration, the membrane-stained effector cells were incubated on the 50 µg/mL FN coating for 5 and 7.5 mins.

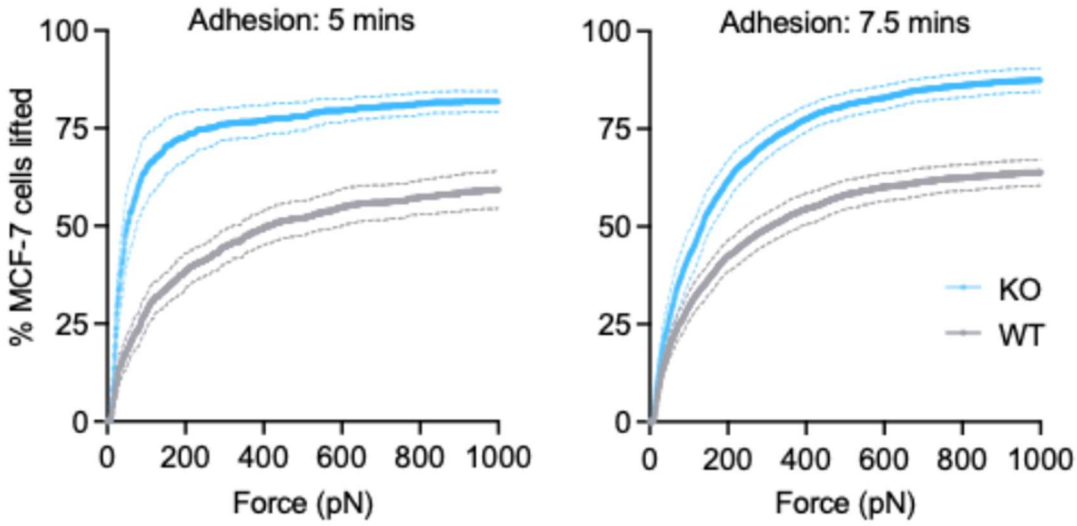

Figure 3.7. Avidity measurements of MCF-7 WT and MCF-7 P1KO incubated on FN at time points: 5 (left) and 7.5 mins (right). The presented trends represent the percentage of cells lifted across the applied force ramp of 0 – 1000 pN.

After the 2.5 min force application from 0-1000 pN is completed, it can be shown in Figure 3.7 at the adhesion time point of 5 mins, MCF-7 WT exhibited a higher overall binding strength with approximately 43% of cells lifted at 200 pN and 60% at 1000 pN. Comparing these values to MCF-7 P1KO, which exhibited lower binding avidity to FN, it is observed that at 200 pN, 75% of cells were lifted and 80% at 1000 pN. The significantly

higher avidity difference across the MCF-7 WT and its isogenic derivative, MCF-7 P1KO, can be attributed to the original Piezo1 expression level being already high in the MCF-7 WT. This may explain the sharp decrease observed in the MCF-7 P1KO avidity curve. Additionally, when the adhesion time to FN is increased to 7.5 mins before the force application, a similar trend to that of the 5 mins incubation is observed. For MCF-7 WT, the percentage of cells lifted were approximately 43% at 200 pN and 63% at 1000 pN. In contrast, MCF-7 P1KO showed approximately 60% of cells detached at 200 pN and 83% at 1000 pN. For each time point, four runs of experiments were performed for a single z-Movi chip where the first data set is omitted due to an evident increase in avidity when compared to the remaining three runs. The avidity trends presented incorporate data collected from three separate z-Movi chips in one day. This was repeated twice more on separate days.

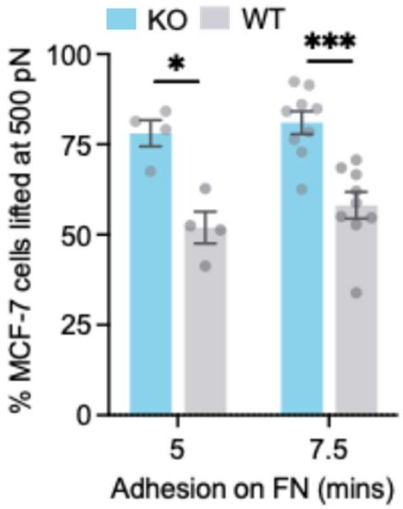

Figure 3.8. Avidity measurements of MCF-7 WT and MCF-7 P1KO incubated on FN at time points: 5 and 7.5 mins at the selected force point of 500 pN.

To better highlight the avidity differences observed between the two different Piezo1 expression levels, data points were taken at the 500 pN force point and plotted across the two adhesion times represented in Figure 3.8. The overall trend between MCF-7 WT and MCF-7 P1KO is similar to the HEK23T isogenic cell lines, indicating that with the elimination of Piezo1, the initial attachment process is significantly delayed. To further validate these observations, 2.5 and 5 μM dosages of GsMTx4 were used to drug-treat MCF-7 WT for a period of 20 mins. The adhesion time point was set at 5 mins as the avidity difference between the two time points were similar.

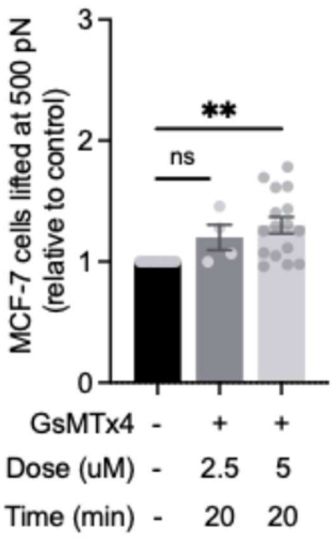

Figure 3.9. Avidity measurements at 500 pN of MCF-7 WT drug treated with 2.5 and 5 μM of GsMTx4 to inhibit the Piezo1 function. MCF-7 WT cells were treated for 20 mins before introduction to FN coating for 5 mins. Untreated MCF-7 WT avidity measurements are included for comparison.

Relative to the control, that is, the untreated MCF-7 WT cells, the GsMTx4-treated cells lifted at 500 pN was normalised and graphed in Figure 3.9. By taking the data points at 500 pN, the observed trend depicts an increase in cell detachment when Piezo1 is inhibited in the GsMTx4-treated MCF-7 cells. With a high percentage of cell lifted, this demonstrates that by impeding the function of Piezo1, the total binding strength is reduced. By discerning the similar decreasing avidity curves when Piezo1 is removed or inhibited for both transformed and tumour cell lines, it can be interpreted that Piezo1 is involved in the initial attachment process and can regulate the cellular avidity on FN.

3.4.4. Discussion

It has been previously established that the mechanosensitive ion channel, Piezo1, is involved in cell spreading and has the capacity for adherent cells to respond to mechanical stimuli. Through implementation of the acoustic force-based cell avidity analyser, z-Movi, the presented findings suggest that Piezo1 plays a significant role during the initial attachment stage of the cell adhesion process. Recent studies of cell spreading on micropatterns have demonstrated that normal human embryonic kidney (HEK293) cells expressing Piezo1 exhibited elongation on FN stripes, whereas when Piezo1 is knocked out, the HEK293 cells no longer elongate. This was further validated through the inhibition of Piezo1 conductance through drug treatments with GsMTx4 and Gadolinium

Chloride ($GdCl_3$) which resulted in only partial cell spreading across the micropatterns [170]. As the recruitment of Piezo1 is hypothesized to be force-dependent, studies have shown that with the inhibition of actomyosin contraction through drug treatments using Y-27632 or blebbistatin, there is a significant reduction of Piezo1 in the adhesion sites before FA disassembly. Additionally, the CV-1 Origin Simian (COS)-7 cells have been studied to model the force-dependency for the recruitment of Piezo1. By restoring the myosin internal iliac artery-dependent contractility, an influx in Piezo1 accumulation to adhesions is observed. Overall, these studies suggest that the magnitude of the force applied, and the force duration dictates the degree of recruitment of Piezo1 at FA [168].

As Piezo1 accumulates at FA sites, a resulting calcium influx in the cell occurs. These cations facilitate with regulating various cellular processes, including cell adhesion. With the increase in calcium intake, Piezo1 can subsequently control the FA dynamics, determining the integrity of the cell-ECM interactions [167], [171]. This supports the notion that by impeding the Piezo1 structure and function accompanied by the lack of FA regulation, it results in the instability of cell-matrix interactions, observed as the significantly lower avidity profiles in the initial attachment stage. Typically, the localized calcium transients surrounding the adhesions in normal cells are evidently weaker when compared to transformed cells. This indicates that the interaction between Piezo1 and adhesions have been modified during the transformation process [167], [172]. In support of this, a secondary study demonstrated that Piezo1 is involved during the maturation stage of cell adhesion for normal cells but had no influence on transformed and tumour cells, whereas the presented findings in this thesis demonstrate that Piezo1 is involved in the initial attachment of cell adhesion for both transformed and tumour cells [167].

To conclude, the novel approach of utilising the biophysical acoustic force-based z-Movi technology to investigate the role of Piezo1 during initial cell adhesion has proven to be a reliable and highly versatile application. With its high-throughput capabilities and relatively short experimental time, rapid analysis of cell-matrix interactions is possible across all stages of cell adhesion.

Chapter 4: The Development of Acoustic Force Spectroscopy for Live Cell Studies

Section 4.1. in this chapter aims to first introduce the operational system behind AFS, including the experimental configuration, software interface, and the analysis of AFS experiments. Following this, Section 4.2. details the application of AFS in investigating the role of Piezo1 in cellular mechanoprotection.

4.1. Operational System of AFS

In the literature review presented in Chapter 2, the principles behind AFS and its application in biomolecular and cellular studies are detailed. With the capability for high-throughput, AFS employs acoustic forces to measure the structural, mechanical and kinetic properties of cells.

4.1.1. AFS Experimental Configuration

The AFS experimental configuration is multi-faceted, incorporating a z-Movi chip holder, Nikon inverted microscope (Nikon Eclipse Ti2), IDS imaging camera (UI-3240CP-M-GL), Nikon Collimation Adaptor (COP5-A), acoustic force field generator, z-Movi microfluidic chip and the accompanying AFS software. The setup involves the z-Movi chip holder to be positioned on the stage of the microscope where a z-Movi chip is fastened in place by tightening four thumb screws located at each corner of the chip. The z-Movi chip holder has **8** prongs that connects to the PCBA of a z-Movi chip to extract information, such as the chip serial number and the pre-calibrated force map. The extracted data is then fed back to the acoustic force field generator. The AFS software reads and visualises this data and performs minor adjustments, and through a feedback loop with the generator, calibrates the resonant frequency with respect to the physical properties of the interacting cell. Once the appropriate resonance frequency is determined, the magnitude of the desired power and mode of the force application (i.e. force ramp or force clamp) is then applied to the z-Movi chip.

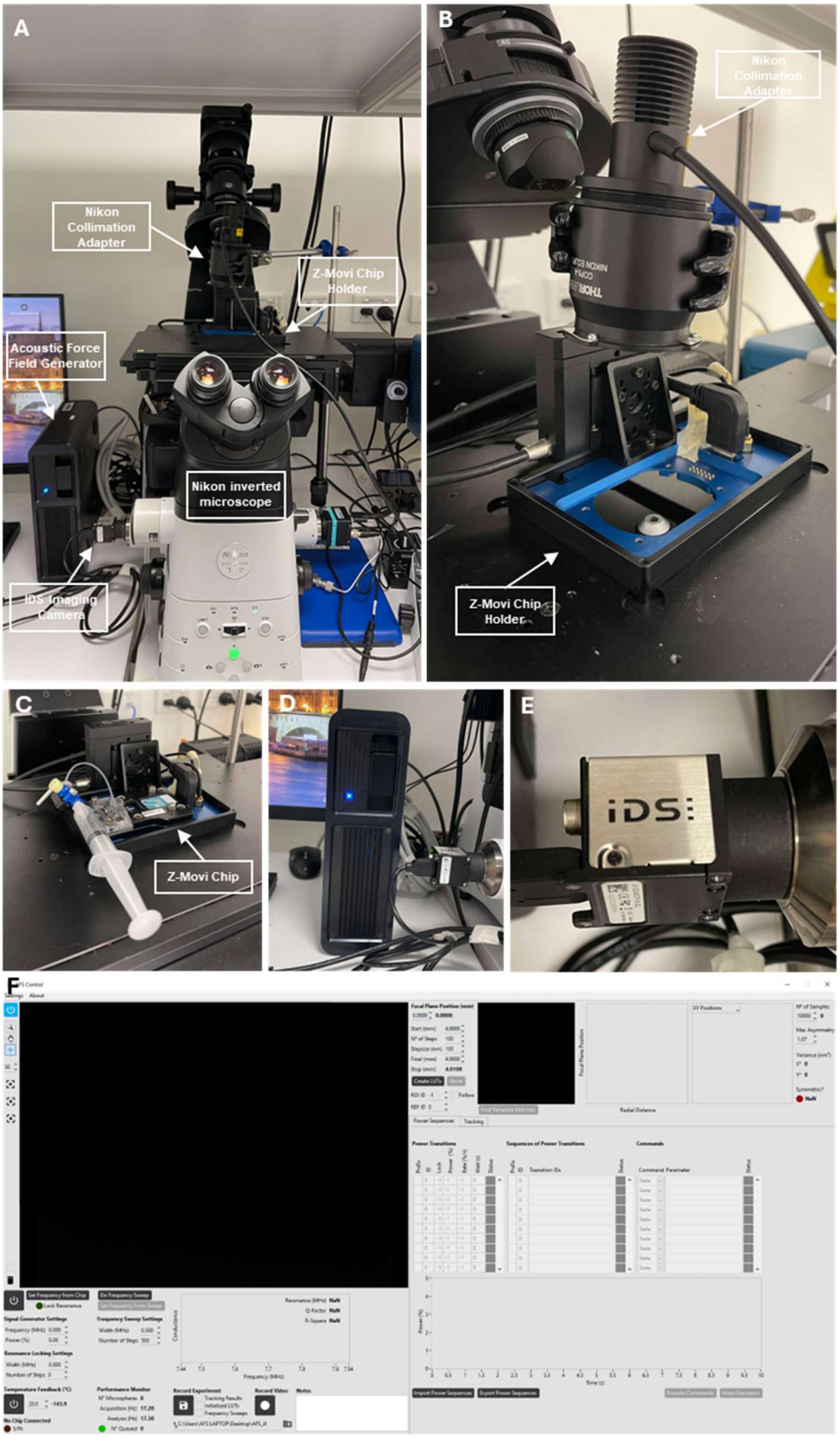

Figure 4.1. Schematic of AFS assembly. (A) An overview of the AFS hardware system. (B) The z-Movi chip holder with a Nikon collimation adaptor. (C) AFS stage with the z-Movi microfluidic chip secured to the holder. (D) Acoustic force field generator (E) iDS imaging camera (F) AFS software interface.

4.1.1.1. z-Movi Microfluidic Chips, Chip Holder and Acoustic Force Field Generator

In this AFS experimental setup, certain z-Movi components were repurposed and integrated, leveraging the shared AFS-based operating principle of the z-Movi system. This includes the z-Movi microfluidic chips, chip holder and controller, that is, the acoustic force field generator. Although the AFS configuration integrates these z-Movi components, it is important to note that this AFS setup enables a greater range of applicable force modalities as compared to the commercialised z-Movi device explored in Chapter 3. For example, the z-Movi device is only capable of one force application, a linear force ramp from 0 to 1000 pN across 2.5 mins whereas the AFS system can apply up to 8000 pN for any desired length of time with complete flexibility of the force patterns, either as a force ramp (gradually increasing tension), force clamp (constant tension) or a combination of the two. Although the avidity measured by z-Movi is graphed as a function of force, the cellular interactions measured using AFS is graphed as a function of percentage of maximum power. The preparation of the z-Movi chip to investigate the role of Piezo1 in cellular mechanoprotection will be detailed in Section 4.2.

4.1.1.2. AFS Software

The AFS software allows for the adjustment of the temperature, resonance frequency and the acquisition parameters, including the frame rate and shutter time. Selected particles are tracked through brightfield imaging where the AFS software determines the particles' x-, y-, and z-positions. Once the z-Movi chip has been secured to the chip holder, the AFS software can be initiated. The general workflow of the software involves setting the *temperature feedback* (Figure 4.2A) to 37 ˚C before zeroing the *power percentage* (Figure 4.2B) and turning on the signal generator (Figure 4.2C). Depending on the particle size, adjust the *region of interest (ROI)* for the particle selection (Figure 4.2D) to the desired area and attune the *focal plane position* (Figure 4.2E) to best visualise the particle.

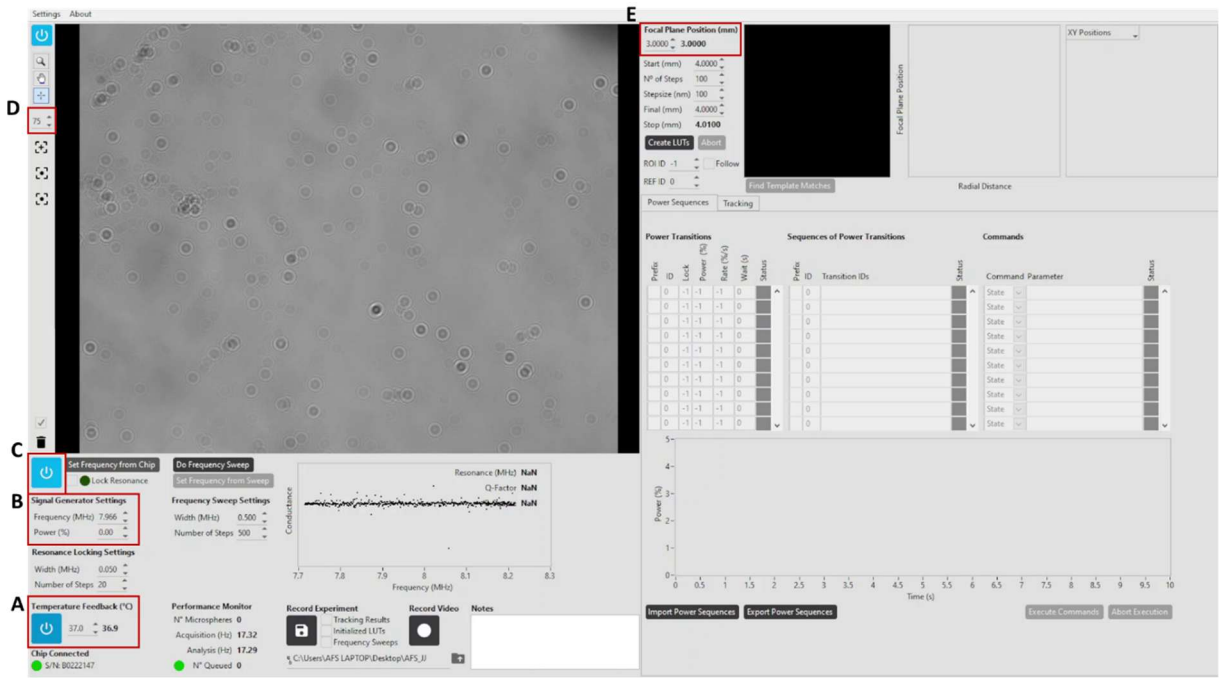

Figure 4.2. AFS software interface during setup (A) Temperature feedback settings (B) Power percentage settings (C) Signal Generator button (D) ROI adjustor for particle selection (E) Focal Plane Position settings.

To establish the desired power sequences, the power transitions first need to be parameterised by entering the required power percentages in the *power* column (Figure 4.3A) and the duration of force application in the *wait* column (Figure 4.3B). By dragging each transition into the *sequences of power transitions* column (Figure 4.3C), the power sequence can then be initiated under the *command parameter* column (Figure 4.3D). Before the force application, initiate a frequency sweep (Figure 4.3E) to determine the resonance frequency specified in the printed circuit board assembly (PCBA) of each z-Movi chip. Once particles have been introduced to the channel, select the particles of interest to begin tracking in the x-, y- and z-position. When the force application commences, the software is able to detect the detachment of tracked particles, that is, where the particle leaves the ROI placed on it.

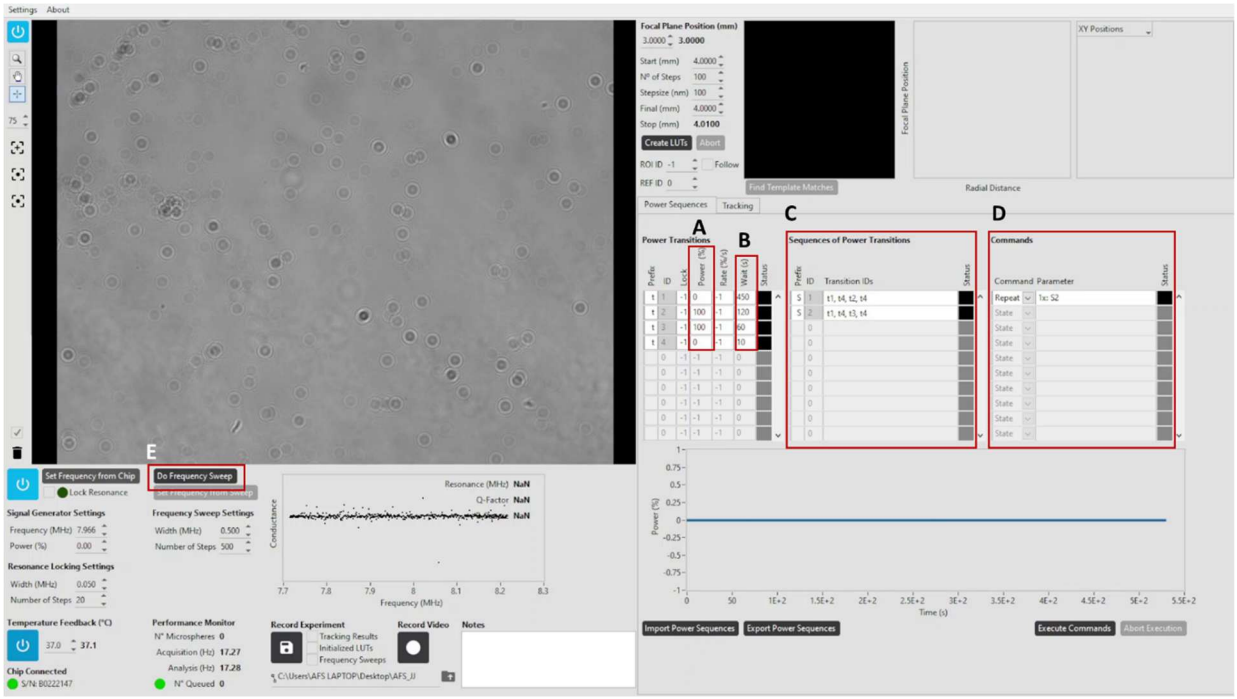

Figure 4.3. AFS software interface for configuring the force application (A) Power column (B) Wait column (C) Sequences of Power Transitions (D) Command Parameter (E) Frequency Sweep button.

4.1.2. Data Analysis

To analyse the results attained from the AFS experiments, there are two main approaches, using the accompanying AFS data analysis software or through manual data analysis.

4.1.2.1. AFS Data Analysis Interface

To utilise the accompanying data analysis software, the data collected from the AFS software must first be converted into a compatible file format. Using the Python code found in Appendix A provided by LUMICKS, the generated technical data management systems (TDMS) files were converted into binary files which can be imported into the data analysis software. The original Python code was modified to allow access to the corresponding file paths. After importing the binary files into the data analysis software, the tracking signals in the x-, y-, and z-position can be visualised.

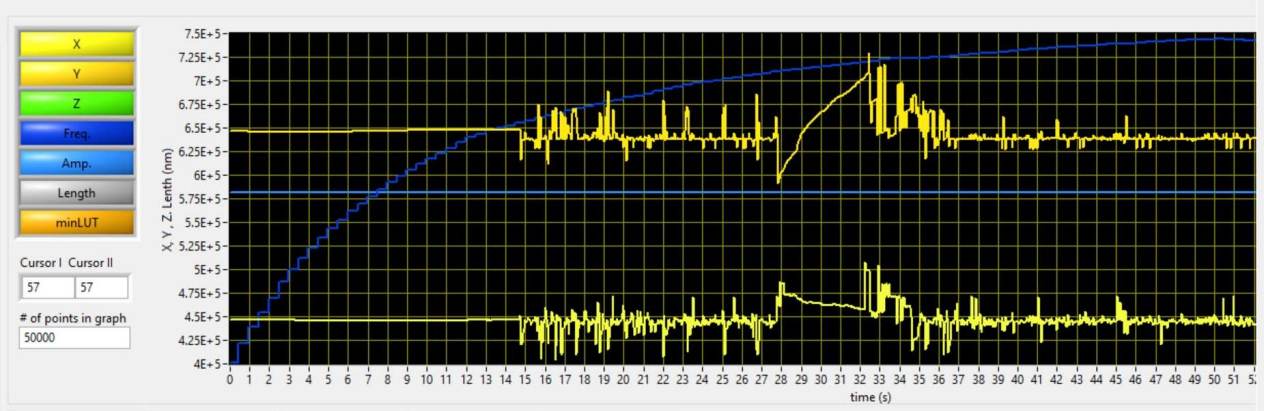

Figure 4.4. Resultant x- and y- position signal of a cell bound to the FN-coated glass surface, tracked through the AFS software. The significant spike demonstrates a rupture event which indicates that the cell has detached from the surface. A positive spike on the x-position indicates that the particle was pulled towards the right, and a negative spike would indicate the particle was pulled to the left, where the centre is denoted as the original position held by the particle. This can be applied to the y-position, where a positive spike represents pulling in the upward direction and a negative spike represents a pulling in the downward direction.

From Figure 4.4, it is observed that when the particle remains within the confines of the selected ROI, there is little background signal. In comparison, when the particle is outside the ROI, there is a significant spike in the displacement of the x- and y- position, indicating the detachment of the particle from the substrate. It should be noted that the displacement for the z-position can also be visualised if the focal plane position was calibrated in the initial setup. The time point at which the particle displacement occurs can be located at the onset of the signal spike. The time point at which the signal returns to the baseline signal indicates when the particle is completely detached from the surface. Depending on the negative or positive spikes on the graphs for the x and y displacements, the direction of the particle displacement and the closest acoustic node can be determined. For the experiment performed in Section 4.2, the AFS Data Analysis Software was not utilised as more in-depth analysis was required. As such, manual data analysis was performed.

4.1.2.2. Manual Data Analysis

In addition to the AFS data analysis software, manual data analysis can be performed to investigate particle-substrate interactions within a field of view (FOV). The particle-substrate interactions recorded can be categorised into four interaction types: immediate detachment, short tethering, long tethering and no detachment. For events categorised as immediate detachment, the time point corresponding to the complete

detachment of the particle is recorded, enabling the calculation for the retention of the particle to the substrate. When categorised as a tethering event (short or long), the time point for the onset of particle tethering, the duration of the tethering and if applicable, the time point of complete particle detachment is recorded. For events where the particle exhibited no detachment, the retention time on the substrate is recorded as the end time point of the force application period.

4.2. PIEZO1 Mechanically Protects Cell Integrity Through Balancing Membrane Tensions

The following section details the application of AFS in investigating the role of Piezo1 in cellular mechanoprotection. Employed alongside AFS brightfield imaging, confocal microscopy is also used to study the cellular response after experiencing acoustic force.

4.2.1. Introduction

What happens when a cell's structure is pushed to its limits? Mechanical forces are fundamental for cellular function however the maintenance of cellular integrity remains as one of the most critical yet often overlooked frontier in modern medicine and biotechnology. With the growing aging population and the global rise of cardiovascular diseases, there is an unprecedented demand for mechanical support devices where over 50,000 left ventricular assist devices are implanted worldwide [173], [174]. While life-saving interventions including extracorporeal membrane oxygenation and haemodialysis provide vital support, they expose blood cells to supraphysiological shear stresses of greater than 100 dyne/cm^2, potentially triggering haematologic complications such as haemolysis and thrombosis [175]. Similarly, the biotechnology revolution has rapidly advanced for tissue engineering and organoid development. However, the mechanical procedures involved in bioprinting and biofabrication impose significant mechanical forces during extrusion processes leading to compromised cellular viability and tissue functionality [176], [177]. Despite such challenges, the biomolecular mechanisms that safeguard the cellular integrity remains severely understudied.

During the process of mechanotransduction, cells adopt mechanically-gated ion channels to function as key transducers to sense and respond to mechanical stimulation [178]. In particular, the mechanosensitive ion channel Piezo1 is a primary regulator by converting mechanical forces such as membrane tension into electrochemical signals where a Ca^{2+} influx is observed due to the opening of the Piezo1 channel, resulting in downstream signaling [179]. However, the unique triskelion-bladed structure of Piezo1 suggests potential functions independent of ion conduction. Structural studies have shown that while other mechanosensitive ion channels such as Transient Receptor Potential Cation Channel Subfamily M member 4 (TRPM4) and Anoctamin 2 (ANO2) exhibit insignificant influence on the cellular membrane structure, the combined convex centre and three-bladed architecture of Piezo1 stimulates more distinct nanocurvature [180], [181].

The idea that membrane proteins are able to facilitate the mechanoprotective abilities of cells through structural properties, irrespective of their innate electrochemical signalling potential, offers a new outlook in investigating the mechanisms of cellular resilience. This chapter proposes that Piezo1 can confer mechanoprotection via its structure to reinforce cellular integrity. By elucidating the mechanoprotective capabilities of Piezo1, this work aims to establish the novel concept where Piezo1 is capable of dual functionality – mechanosensation through calcium influx and mechanoprotection through structural reinforcement.

4.2.2. Methods and Materials

4.2.2.1. List of Reagents

Table 4-1. Detailed list of reagents used in the Methods.

Full Name	Source	Catalogue Number
Dulbecco's Modified Eagle Medium (DMEM)	Thermo Fisher Scientific	11995073
Fetal Bovine Serum (FBS)	Thermo Fisher Scientific	10100147
Penicillin-Streptomycin (PS)	Sigma-Aldrich	P4458-100ml
Geneticin™ Selective Antibiotic (G418)	Sigma-Aldrich	G8168-100ML
Phosphate-Buffered Saline (PBS)	Thermo Fisher Scientific	10010023

TrypLE™ Express	Thermo Fisher Scientific	12604021
Trypan Blue	Thermo Fisher Scientific	15250061
Fibronectin (FN)	Thermo Fisher Scientific	33016015
Ethylene glycol-bis(2-aminoethylether)-N,N,N',N'-tetraacetic acid (EGTA)	BioWorld	40120127-1
Calcein405	Thermo Fisher Scientific	65-0855-28
mβCD	Merck Life Science	C4805-5G
CellMask Orange (CMO555)	Thermo Fisher Scientific	C10045
CellMask Green (CMG488)	Thermo Fisher Scientific	C37608
Phalloidin 488 (Pha488)	Thermo Fisher Scientific	A12379
Phalloidin 647 (Pha647)	Thermo Fisher Scientific	A30107
Janelia Fluor® JFX554 HaloTag® Ligands (JFX554)	Promega Corporation	HT1030

4.2.2.2. Cell culture and Harvesting

Transformed Human Embryonic Kidney cell lines HEK293T with Piezo1 Wildtype (WT), Knockout (P1KO; kindly gifted from Dr Ardem Patapoutian), and Overexpressed-Halo (P1OE; kindly gifted from Dr Philip Gottlieb) and the breast cancer cell line MCF-7 with Piezo1 WT and P1KO was cultured in Dulbecco's Modified Eagle Medium (DMEM; Thermo Fisher Scientific) supplemented with 10% Fetal Bovine Serum (FBS; Thermo Fisher Scientific) and 1% Penicillin-Streptomycin (PS; Sigma-Aldrich). The cultured cell lines were stored in a saturated incubator at 37 ˚C with 5% CO_2. This solution will be referred to herein as complete culture medium. During the transfection process, HEK293T P1KO-Mutant-Halo (P1KO-Mutant) and HEK293T P1KO-TRPM4-GFP (P1KO-TRPM4) cells were cultured in 5 mL of complete culture medium supplemented with 80 µL of the disulfate salt solution, Geneticin™ selective antibiotic (G418; Sigma-Aldrich), which is at a concentration of 800 µg/mL. HEK293T P1KO-Mutant and P1KO-TRPM4 was continuously maintained using 5 mL of the complete culture medium supplemented with 40 µL of G418 to attain a concentration of 400 µg/mL. Cells were maintained in T25

culture flasks and when required for experiments, cells were seeded into 35 mm x 10 mm petri dishes and left to recover overnight before use.

Prior to experiments, the cells were harvested when the confluency in the petri dishes reached approximately 80%. Cells were initially washed with Phosphate-buffered saline (PBS; Thermo Fisher Scientific) before being incubated with TrypLE™ Express (Thermo Fisher Scientific) for 3 min at 37 ˚C. After the cells begin to detach from the surface of the culture flask, they are resuspended in complete culture medium. The concentration of the cells in suspension was calculated by mixing 10 µL of the cell solution and 10 µL of 0.4% Trypan Blue (Thermo Fisher Scientific) before seeding 10 µL of this mixture between the haemocytometer dish and a glass slide. The cell concentration can be calculated using the following equation:

$$Cell\ Concentration = \frac{Total\ cell\ count\ in\ squares\ \times Dilution\ factor}{No.of\ squares} \times 10^4$$

To note, each experimental run requires 20 µL of a cell solution at a concentration of 3×10^6 cells/mL. To ensure optimal viability, a larger initial volume of 40 µL was taken from the 3×10^6 cells/mL stock solution. Before seeding, each 40 µL aliquot is resuspended to ensure the cell pellet is separated from which 20 µL will be taken for seeding.

4.2.2.3. Chip Glass Surface Coating with Fibronectin

Ensure the channel of the z-Movi microfluidic chip is cleaned and dried for at least 1 hr before beginning the surface coating process. To begin the coating process of each chip, the glass surface of the channel was rehydrated by pulling in 400 µL of 1 M sodium hydroxide (NaOH) from the reservoir into the channel using a 3 mL syringe (Terumo) for an incubation period of 5 min. The channel was then washed twice with 400 µL of Milli-Q water before pulling in 400 µL of 1 M HCl for an incubation period of 2 min. The channel was again washed with 400 µL of Milli-Q water for three times before pulling in 400 µL of PBS. Majority of the PBS was pulled through the channel, leaving approximately 10 µL of PBS left in the reservoir. For each chip, 30 µL of 50 µg/mL FN (Thermo Fisher Scientific) solution was pulled through the reservoir until approximately 5 µL was remaining. The reservoir was washed twice with 200 µL of PBS to prevent aggregate formation before a

final 200 µL was deposited into the reservoir. The coated microfluidic chips are then secured with a cap and stored for at least 16 hrs in a dry incubator at 37 ˚C. It is important to note that the FN coating lasts up to 72 hrs from the initial coating. Before introducing the cells into the channel, the FN-coated chips were washed twice with 400 µL of PBS before introducing a buffer exchange with 400 µL of completed culture medium ensuring 10 µL remains in the reservoir.

4.2.2.4. AFS Operational Settings

Upon launching the software, the *temperature feedback* was set to 37 ˚C before zeroing the *power percentage* and turning on the signal generator. The *ROI* was adjusted from 50 × 50 pixels to 75 × 75 pixels for the particle selection area. To focus on the channel of the microfluidic chip, the *focal plane position* was set to 3 mm. For the standard power sequences, the inputted power percentages in the *power* column and duration of the force application in the *wait* column was 0% for 300 secs for the interaction period between the cells and the FN coating, 50% for 120 secs for the acoustic force application, and 0% for 5 secs to re-zero the *power percentage*. For AFS experiments that was followed by confocal imaging (FV4000, Olympus Corporation) after each run, the power transitions were set at 0% for 450 secs for the FN-interaction, 0% for 10 secs for a buffer exchange before force, 100% for 120 secs for the force application and 0% for 5 secs to re-zero the *power percentage*. Before the force application, a frequency sweep is initiated to determine the resonance frequency specific to each chip. The resonance frequency is then calibrated and set as the frequency under the *Signal Generator Settings*. For more details, refer to Section 4.1. which details the AFS configuration and software.

4.2.2.5. Cell-matrix Binding Measurement

The z-Movi chip (LUMICKS B.V.) was secured on the z-Movi chip holder and through the FOV, the channel of the microfluidic chip was focussed. Before seeding the cells and beginning the FN-interaction, the volume of complete culture medium remaining in the reservoir was levelled down to approximately 5 µL. After resuspending the 40 µL aliquot of the 3×10^6 cells/mL cell solution, 20 µL was separated and deposited into the reservoir inlet for seeding. The cells are seeded by pulling the cell solution through the channel using a 3 mL syringe and interact with the FN coating for either 5 mins (standard parameters) or 7.5 mins (parameters with confocal imaging) before a

force application is initiated. During the incubation period, the reservoir is washed twice with 200 µL of complete culture medium to remove cell aggregation left from the seeding solution. The inlet is refilled with the appropriate culture medium – complete medium for Ca^{2+}-positive systems and culture medium treated with ethylene glycol-bis(2-aminoethylether)-N,N,N',N'-tetraacetic acid (EGTA; BioWorld) for Ca^{2+}-negative systems. The concentration of the EGTA was 3mM where 0.6 µL was mixed with 200 µL of DMEM medium only. After the incubation period, the force application begins for 2 mins where the force clamps at either 50% (standard parameters) or 100% (parameters with confocal imaging). It is important to note that the percentage parameters of the power refer to the percentage of max power, for instance 50% power represents 50% of the max power generated by the acoustic force field controller. During the force application, different types of cell-matrix interactions were recorded – immediate detachment, short tethering, long tethering and no detachment.

4.2.2.6. Confocal imaging

Before running the AFS experiments, the 40 µL aliquots of concentration 3 cells/mL solution were suspended in DMEM medium only and stained with Calcein405 (Thermo Fisher Scientific) with a dilution ratio of 1:500 for 25 mins. Prior to seeding, Methyl-β-cyclodextrin (mβCD: Merck Life Science) is added 2 min before Calcein405 staining was completed. The cells are then seeded and incubated with FN for 7.5 mins. Before the force clamps at 100% power for a duration of 2 mins, the channel undergoes a buffer exchange with complete culture medium for Ca^{2+}-positive systems and EGTA-treated culture medium for Ca^{2+}-negative systems. After the force application, the cells are stained to determine the level of damage, that is, either major rupture or minor damages. For HEK293T WT and HEK293T P1KO, 1:500 CellMask Orange (CMO555; Thermo Fisher Scientific) and 1:2000 Phalloidin 488 (Pha488; Thermo Fisher Scientific) was used to stain the cell membrane and actin, respectively. For HEK293T P1OE and HEK293T P1KO-Mutant, 1:500 CellMask Green (CMG488; Thermo Fisher Scientific), 1:2000 Phalloidin 647 (Pha647; Thermo Fisher Scientific) and 1:1000 Janelia Fluor® JFX554 HaloTag® Ligand (JFX554; Promega Corporation) was used to stain the cell membrane, actin and the HaloTag, respectively. For HEK293T P1KO-TRPM4, 1:500 CMO555 and 1:2000 Pha647 was used to stain the cell membrane and actin, respectively. After the dyes have stained the cells in the channel for 5 mins, the microfluidic chips are

then fixed onto the FV4000 stage for confocal imaging. Lasers at wavelengths of 488 nm, 594 nm and 640 nm were used to excite the dyes. The images were scanned at 1024 × 1024 pixels resolution for a single z-position.

4.2.2.7. Data Analysis

The data analysis conducted on the presented experiments were performed using the manual analysis method. Observations made on video recordings of the experimental runs categorised cell-matrix interactions into four types: immediate detachment (0 – 1 secs), short tethering (2 – 5 secs), long tethering (5 – 120 secs) and no detachment. Duration before detachment, before tethering and during tethering were recorded. For more detail on the AFS data analysis, refer to Section 4.1.2. The data analysis involved for the confocal imaging used the membrane and actin staining to determine if the cell body experience major damages. When both CMO555/CMG488 and Pha488/647 entered through the cell body following the force application, this was counted as double-positive staining, indicating significant rupture of the cell body. To note, only double-positive staining was considered as a representation of major rupture. For minor damages, the level of Calcein405 staining was used as an indicator. The extent of damage was assessed by normalizing the intensity change in the Calcein405 staining after force application relative to the control.

4.2.2.8. Statistics and Reproducibility

All representative results presented in this chapter are from at least three independent experiments generating similar outcomes. For each independent experiment, the data was collected from three separate z-Movi chips in one day which was repeated twice more on separate days. All statistical analyses were performed using Prism 10 (GraphPad Software).

4.2.3. Results

4.2.3.1. Cell Membrane Deformations for Transformed Cells

To characterize the impact of Piezo1 in cellular mechanoprotection, the AFS was employed. Repurposing the z-Movi microfluidic chips, the glass surface of the channel was overnight-coated with the ubiquitous glycoprotein FN. Prepared HEK293T WT,

HEK293T P1KO, and HEK293T P1OE cells were introduced into the channel and interacted with the FN coating for 5 mins before a force clamp of 50% power was applied. The generated acoustic forces induced cell membrane deformation with four distinct types of cell membrane interactions: immediate detachment (0 – 1 secs), short tethering (2 – 5 secs), long tethering (5 – 120 secs) and no detachment.

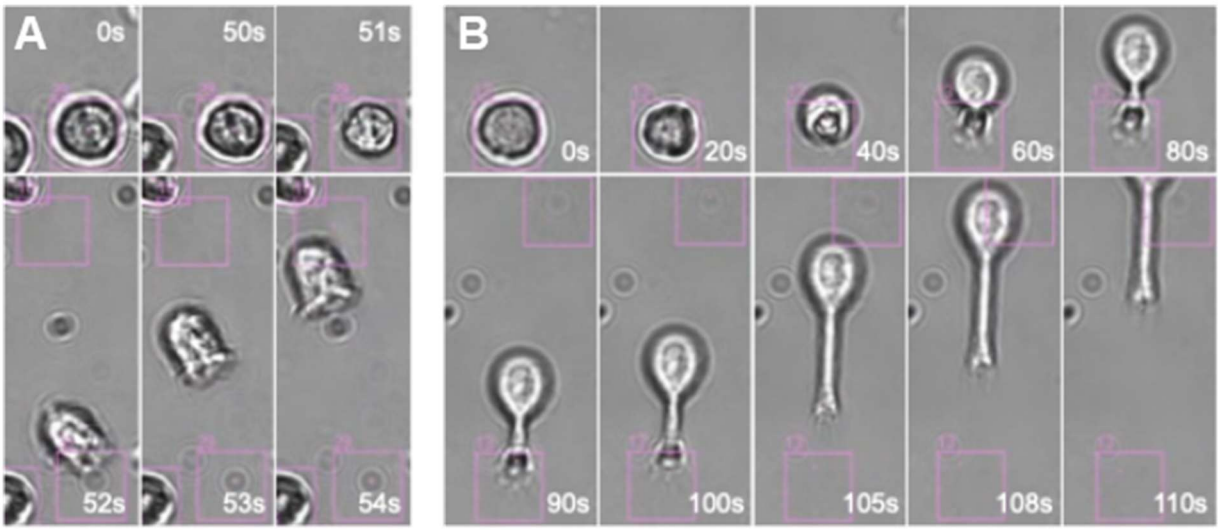

Figure 4.5. Representative images of the two types of tethering. (A) Short-term tethering (B) Long-term tethering.

These interactions were visualised through brightfield imaging, and the two different types of tethering can be seen in Figure 4.5. The membrane tethering events were quantified through recording positive tethering events during the time-lapse brightfield imaging.

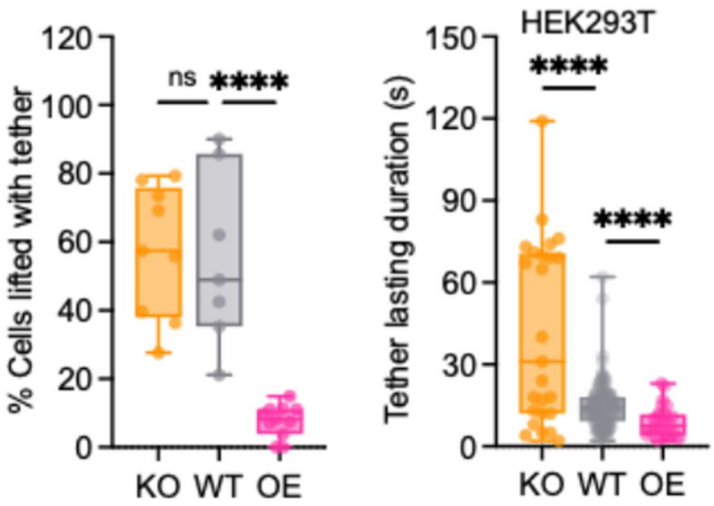

Figure 4.6. HEK293T cell membrane deformation through tethering events. Percentage of cells lifted with tethering (left) and duration of the tethering event (right).

From Figure 4.6, it was observed that HEK293T P1KO exhibited a higher percentage of cells lifted with tethering compared to HEK293T WT and HEK293T P1OE, where the average showed approximately 58% of the cell population exhibited tethering. For HEK293T WT, the average showed that approximately 47% of the cell population exhibited tethering whereas HEK293T P1OE averaged at approximately 8%. Overall, HEK293T P1KO demonstrated a higher precedence of tethering events in the cell population. Potentially attributed to the inherent low expression levels of Piezo1 present in HEK293T WT, the difference between the population of tethering events exhibited between HEK293T P1KO and HEK293T WT was not as significant when compared to HEK293T P1OE. Although the number of tethering events between HEK293T P1KO and HEK293T WT cells was not significantly different, the retention of these events revealed more pronounced differences. To elaborate, the duration of the tethering events exhibited for HEK293T P1KO ranged between 2 to 120 secs, where the average was calculated to be approximately 31 secs. For HEK293T WT, the tethering duration ranged between 2 to 60 secs, where the average was determined to be approximately 13 secs. Similarly, HEK293T P1OE demonstrated tethering durations ranging between 2 to 25 secs, where the average was calculated to be approximately 5%.

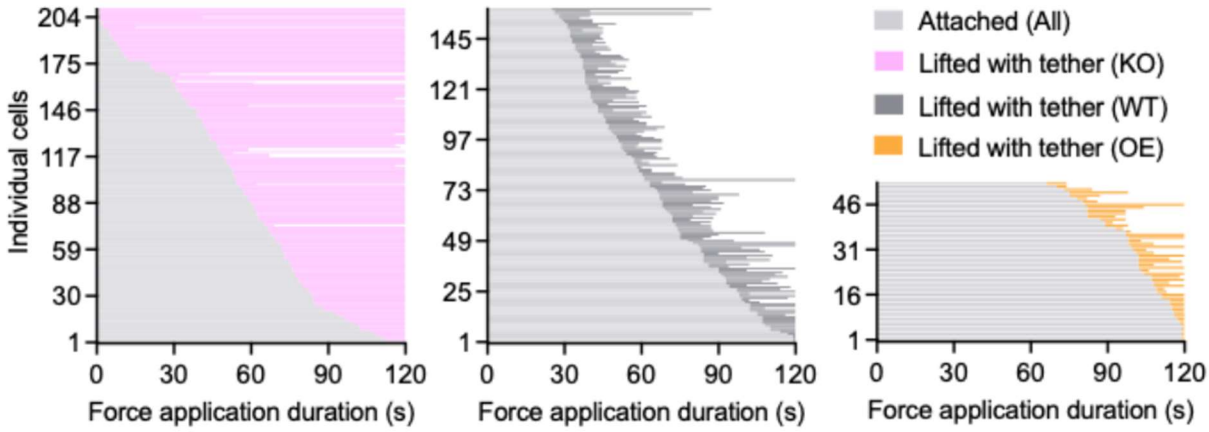

Figure 4.7. Cell-matrix interaction during the force application of 120 secs. The progression from attached to tethering can be depicted for HEK293T P1KO (left), HEK293T WT (middle), and HEK293T P1OE (right).

To better visualize the significant differences of the tethering duration across the three isogenic cell lines, a horizontal bar plot was graphed as shown in Figure 4.7. It is important to note that the cell populations used in the AFS experiments for all three isogenic cell lines were of similar size, however, due to the lower frequency of tethering

events observed in HEK293T P1OE cells, the total number of tethering events analysed was significantly reduced.

4.2.3.2. Cell Membrane Deformations for Tumour Cells

To further investigate the impact of Piezo1 in cellular mechanoprotection, the breast cancer cell line MCF-7 with P1WT and P1KO was used. Similar preparation to the HEK293T cells, suspended MCF-7 WT and MCF-7 P1KO cells were introduced into the channel and interacted with the FN coating for 7.5 mins before a force clamp of 50% power was applied.

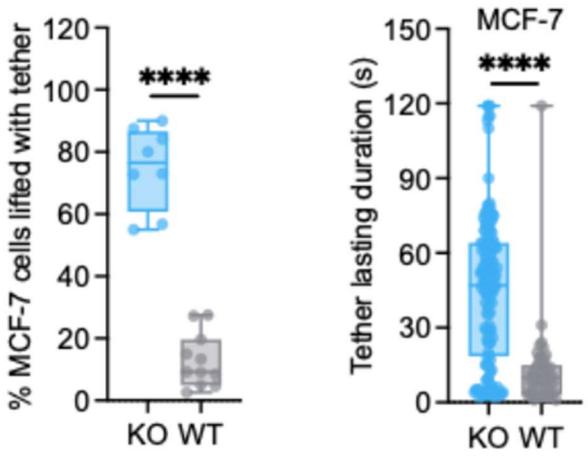

Figure 4.8. MCF-7 cell membrane deformation through tethering events. Percentage of cells lifted with tethering (left) and duration of the tethering event (right).

As observed in Figure 4.8, MCF-7 P1KO exhibited a significantly higher percentage of cells lifted with tethering where the average was calculated to be approximately 77%. For MCF-7 WT, the average percentage of cells lifted with tethering was determined to be approximately 10%. This significant difference can be attributed to MCF-7 WT inherently having high expression levels of Piezo1. To further highlight the pronounced differences between MCF-7 WT and MCF-7 P1KO, the retention of the tethering exhibited for MCF-7 P1KO cells ranged between 2 to 120 secs, where the average tethering duration was determined to be approximately 50 secs. Comparing these results to those of MCF-7 WT, the retention of the tethering also ranged between 2 to 120 secs, however the average tethering duration was found to be approximately 10 secs. Overall, it was observed that when Piezo1 is removed for both HEK293T and MCF-7 cells, the cells exhibited long and lasting tethers during the cell lifting process.

4.2.3.3. Cell Body Membrane Damage and Rupture Events for Transformed Cells

To study the protective function of Piezo1, higher AFS parameters were applied to induce membrane deformation and inflict membrane damage to the cell body. As previously detailed, prepared HEK293T WT, HEK293T P1KO, HEK293T P1OE, HEK293T P1KO-Mutant, and HEK293T P1KO-TRPM4 cells were introduced into the channel and interacted with the FN coating for 7.5 mins before a force clamp of 100% power was applied.

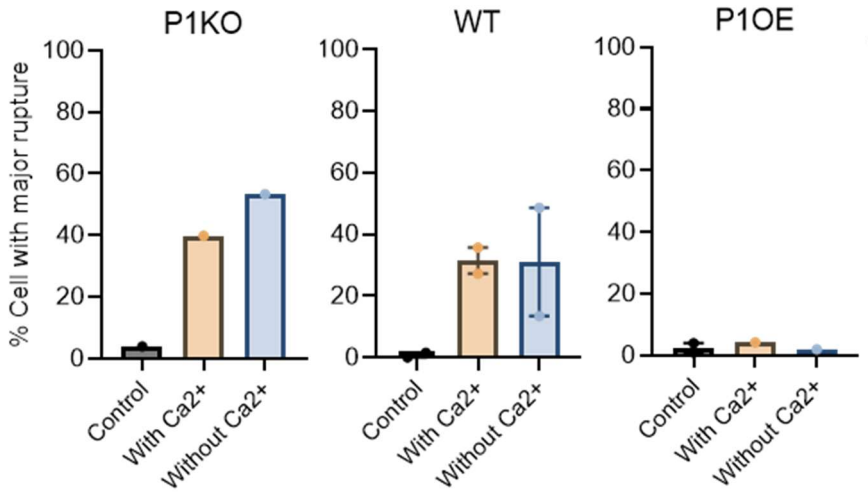

Figure 4.9. Percentage of major rupture events for HEK293T P1KO (left), HEK293T WT (middle), and HEK293T P1OE (right). Major rupture was indicated through double positive staining of membrane and actin dyes.

Additionally, AFS experiments were performed in Ca^{2+} negative systems to determine whether the protective function of Piezo1 is dependent on its ion channel activity. To ensure that there are no Ca^{2+} ions in the system, 3 mM EGTA mixed with DMEM only was used during the buffer exchange prior to the force application. From Figure 4.9, it can be observed that HEK293T P1KO still demonstrated the highest rates of membrane damage when compared to HEK293T WT and HEK293T P1OE. This indicates that the protective effect of the Piezo1 continued even in the absence of extracellular calcium.

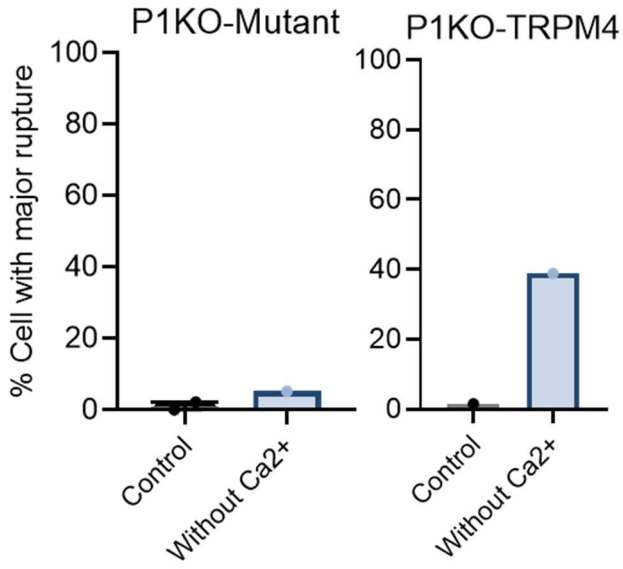

Figure 4.10. Percentage of major rupture events for HEK293T P1KO-Mutant (left) and HEK293T P1KO-TRPM4 (right). Major rupture was indicated through double positive staining of membrane and actin dyes.

Interestingly, for the ion-impermeable Piezo1 mutants (M2493A/F2494A) expressed in HEK293T P1KO cells, the mechanoprotective effect was preserved despite the absence of calcium conductance (Figure 4.10). This indicates that apart from its ion channel function, the structural properties of Piezo1 are involved with mediating membrane protection. In contrast, the non-selective ion channel TRPM4 expressed in HEK293T P1KO continued to show high rates of membrane rupture in a calcium-free environment. This indicates that substituting Piezo1 with TRPM4 does not preserve the mechanoprotective effect against force.

Providing additional support, the intensity of Calcein405 staining was recorded for both Ca^{2+}-positive and Ca^{2+}-negative systems after force application and normalised relative to the control. Upon entering the cell, Calcein405 will remain trapped within an intact cytoplasm until the cell membrane is ruptured or damaged, causing the Calcein to drain out and subsequently reduce the intensity of the dye.

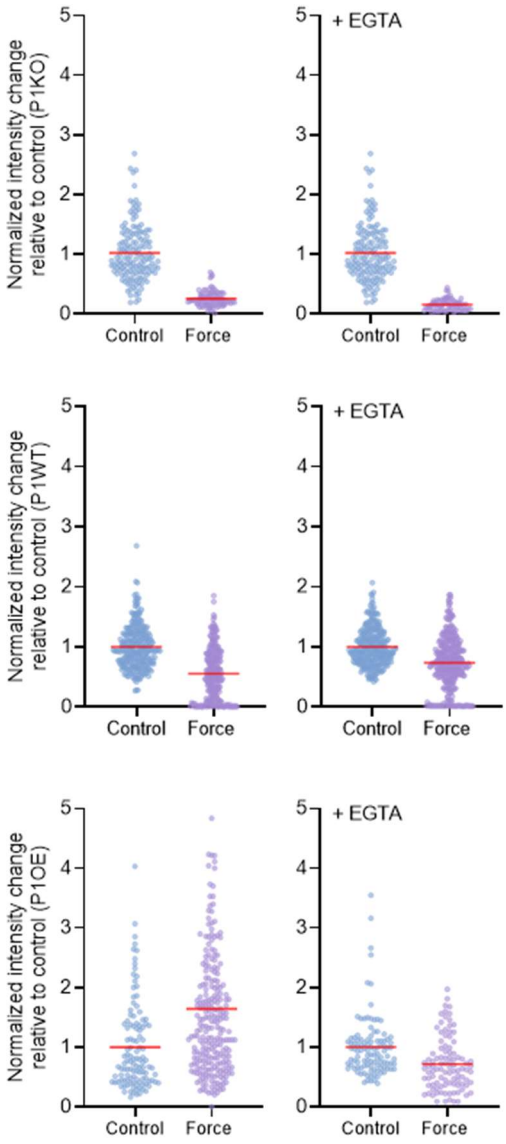

Figure 4.11. Intensity changes of Calcein405 staining for HEK293T P1KO (top row), HEK293T WT (middle row), and HEK293T (bottom row). The intensity changes were normalised against the control.

From Figure 4.11, it is observed that HEK293T P1KO exhibited a significant reduction in Calcein405 intensity for both Ca^{2+}-positive and Ca^{2+}-negative environments, further indicating membrane rupture and damage. The observed intensity change for HEK293T WT was not as significant compared to HEK293T P1KO, however, there was still an overall minor reduction in intensity. In contrast, HEK293T P1OE demonstrated negligible Calcein405 intensity changes in the calcium-free environment and a slight increase in the calcium-present environment.

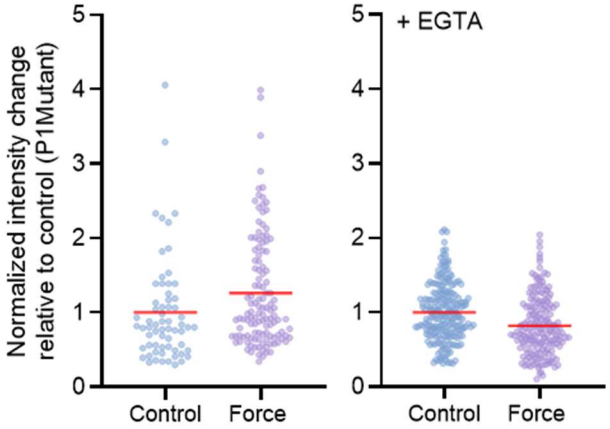

Figure 4.12. Intensity changes of Calcein405 staining for HEK293T P1KO-Mutant in Ca^{2+}-positive (left) and Ca^{2+}-negative (right) environments. The intensity changes were normalised against the control.

Similar to the trend observed for HEK293T P1OE, Figure 4.12 demonstrates that HEK293T P1KO-Mutant is able to facilitate the mechanoprotective properties of the membrane as there is negligible reduction observed for the Calcein intensity, indicating the absence of major rupture or damage.

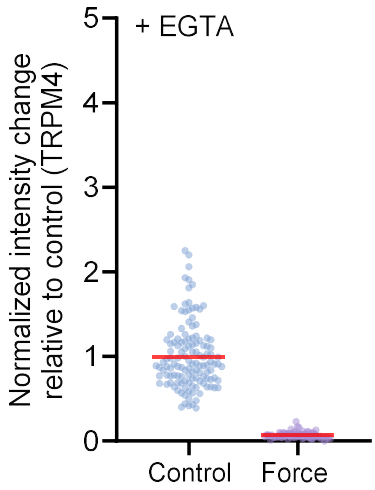

Figure 4.13. Intensity changes of Calcein405 staining for HEK293T P1KO-TRPM4 in a Ca^{2+}-negative environment. The intensity changes were normalised against the control.

Corroborating previous results, Figure 4.13 demonstrates that the ion channel TRPM4 is unable to mediate membrane mechanoprotection. Similar to the HEK293T P1KO, there is a significant reduction in Calcein intensity, suggesting that the membrane is either ruptured or damaged. Overall, the presented data demonstrates that the structural properties of Piezo1 is capable of mediating the membrane protection.

4.2.4. Discussion

The implementation of the AFS system has revealed the ability of Piezo1 as a structural mechanoprotector that preserves cellular membrane integrity undergoing mechanical stimulation. Independent from its canonical ion channel activity, Piezo1 depends on its distinct convex central region combined with triskelion-bladed architecture to protect the cell membrane [179]. By elucidating the mechanoprotective capabilities of Piezo1 through its nanocurvature, this work underlines the dual functionality of Piezo1.

Historically, Piezo1 is involved in the mechanotransduction process wherein it facilitates the cells' ability to sense and respond to mechanical stimuli. It functions by converting mechanical forces such as membrane tension into electrochemical signals where a Ca^{2+} influx is observed due to the opening of the Piezo1 channel, resulting in downstream signaling [180]. Interestingly, through the AFS platform, it was identified that cells without Piezo1 exhibited more elastic cellular membranes represented through the higher rates of deformation, that is, longer and lasting tether formation. Indicated by the Calcein staining and double-positive staining of the membrane and actin, P1KO cell lines demonstrated weaker membrane integrity with larger cell population sizes experiencing major rupture and damage under acoustic forces. In conjunction with this finding, HEK293T P1OE demonstrated that with higher expression levels of Piezo1, the cellular membrane was observed to be more rigid and intact against acoustic forces. This is represented through the low deformation frequency and shorter tethering retention, suggesting that the mechanoprotective properties of Piezo1 may be partially calcium independent.

The protective function of Piezo1 and its dependency on its ion channel activity was validated through AFS experiments in Ca^{2+}-negative environments. Remarkably, the protective effect of Piezo1 continued even with the absence of extracellular calcium, further supporting the notion that the mechanoprotective properties of Piezo1 is independent of its ion channel activity. Furthermore, with the introduction of Piezo1 mutants expressed on HEK293T P1KO, the mechanoprotective capabilities was rescued despite the impaired calcium conductance. This suggests that Piezo1 repurposes its distinctive trimeric architecture to achieve dual functions, that is, mechanosensation

through calcium influx and mechanoprotection through structural reinforcement. Through the coupled functionality of Piezo1, it may explain the increased conservation of Piezo1's structure across various species, reconceptualising the current understanding of the multifaceted roles of membrane proteins in cellular physiology [182].

The mechanoprotective effect was determined to be Piezo1-specific with the introduction of HEK293T P1KO cells expressed with the non-selective ion channel, TRPM4. The findings demonstrated that by replacing Piezo1 with the TRPM4 ion channel, the mechanoprotective properties could not be rescued. This suggests that other mechanosensitive ion channels are incapable of recapitulating the protective properties of that of the Piezo1 structure. The discovery of Piezo1 as a structural mechanoprotector reconceptualises the current understanding of this mechanosensor. Through the elucidation of Piezo1's structure facilitating membrane resilience, valuable insights into cellular adaptation to mechanical stress can be achieved. This provides new avenues to address current challenges in clinical settings, such as for mechanical circulatory support devices for cardiovascular diseases and regenerative medicine.

Chapter 5: Conclusions and Future Directions

5.1 Summary of Findings

This thesis investigated the fundamental roles of mechanical forces in cellular biology, with a particular focus on the mechanosensitive ion channel Piezo1 in regulating cell-matrix and cell-cell interactions. Through the implementation of two complementary acoustic force-based platforms—the z-Movi cell avidity analyser and Acoustic Force Spectroscopy (AFS)—this research has provided quantitative insights into cellular mechanobiology in both high-throughput and single-cell levels.

The comprehensive literature review presented in Chapter 2 established the theoretical framework for this research, detailing the principles of mechanobiology, mechanotransduction pathways, and biomechanical cues that influence cellular behaviour. The review also highlighted the evolution of dynamic force spectroscopy techniques, emphasizing acoustic force-based approaches as powerful tools for high-throughput investigations of molecular and cellular mechanics.

In Chapter 3, the z-Movi cell avidity analyser is introduced as an innovative platform for quantifying cell-matrix and cell-cell interactions in high throughput. Using this technology, the findings demonstrated that Piezo1 plays a significant role in the initial attachment phase of cell adhesion to fibronectin. This reveals that Piezo1 overexpression enhances adhesion strength, while Piezo1 knockout or pharmacological inhibition reduces avidity in both transformed (HEK293T) and tumor (MCF-7) cell lines. These results challenge the prevailing view that Piezo1 primarily influences mature adhesions in normal cells but has minimal impact on transformed or tumor cells. Instead, the data suggests that Piezo1 contributes significantly to the early stages of cell-matrix interactions across different cell types. Additionally, Chapter 3 showcased the versatility of the z-Movi platform through a collaborative study evaluating CAR T-cell binding avidity to target cells. This investigation demonstrated the superior binding capacity of CD19-CAR T cells compared to HER2-CAR T cells, providing mechanical insights into the differential efficacy of CAR T-cell immunotherapy. Furthermore, this work validated a novel bispecific adaptor approach to redirect CD19-CAR T cells to target HER2-

expressing solid tumours, highlighting the potential of acoustic force-based assays in the development and optimization of cancer immunotherapies.

Detailed in Chapter 4, AFS was established for live cell studies, focusing on the role of Piezo1 in cellular mechanoprotection. Experimental findings revealed that beyond its ion channel function, Piezo1 structurally reinforces cell membrane integrity under mechanical stress. Through comparative analyses of both transformed and tumour cells, and calcium-free conditions, the results demonstrated that Piezo1's mechanoprotective role involves both calcium-dependent signaling and calcium-independent structural reinforcement. This expands the current understanding of Piezo1's function beyond traditional mechanotransduction, positioning it as a multifunctional protein critical for cellular adaptation to mechanical environments.

5.2 Significance and Implications

The findings presented in this thesis have several important implications for our understanding of cellular mechanobiology and its relevance to health and disease.

First, the demonstration of Piezo1's role in the initial attachment phase of cell adhesion expands the temporal framework for considering mechanosensitive ion channels in cell-matrix interactions. While previous research has emphasized Piezo1's contribution to mature adhesions, the presented work highlights its importance in the earliest stages of contact establishment. This discovery indicates that mechanical sensing begins immediately after contact between the cell and substrate which can potentially explaining how cells adapt to their microenvironments during processes such as wound healing, tissue regeneration, and cancer metastasis.

Second, the discovery of Piezo1's dual role in mechanoprotection involving both calcium signaling and structural reinforcement, provides more details on the process of how cells maintain integrity under mechanical stress. This finding may be particularly relevant in contexts where cells experience significant mechanical challenges, such as blood circulation, muscle contraction, or tumor invasion. The mechanoprotective function of Piezo1 could represent an evolutionary adaptation enabling cells to withstand the diverse mechanical environments they encounter.

Third, the use of acoustic force-based technologies to evaluate CAR T-cell therapies highlights the broad scope of such approaches in biomedical research. Through quantifying binding avidity at the single-cell level, acoustic force-based platforms offer a mechanical perspective on immunotherapeutic efficacy, complementing traditional functional assays. These quantified avidities provide valuable insights for optimizing cell-based cancer therapies, potentially improving their efficacy against solid tumours. Acoustic force-based systems have been increasingly adapted for in vivo and clinical applications. For example, in blood-based diagnostics, acoustic separation is implemented to enable the sorting of rare circulating tumor cells. Additionally, acoustic waves are utilised in targeted drug delivery to guide nanocarriers toward specific tissues. By focusing on clinically relevant parameters such as cell stiffness, tissue elasticity, and the mechanical properties of circulating cells, AFS is potentially capable of distinguishing between malignant and benign tumours, studying drug-induced effects in cell mechanics, and identifying pathological tissue softening or stiffening.

Fourth, to highlight the novelty of acoustic force-based technologies in comparison to other existing force-based systems, AFS offers scalable and parallel manipulation for high-throughput applications alongside force tuneability for both gentle manipulation as well as stronger force applications. The high dynamic nature of the AFS system enables compatibility with complex media such as fluids and tissue. To compare with other force-based systems, OT operates within similar force ranges as AFS but has limited scalability and is susceptible to flow. While TFM is capable of high-throughput, it measures the forces exerted by cells on a substrate rather than actively manipulating the cells. In conclusion, AFS presents a more holistic set of advantages that addresses certain limitations found in existing force-based systems.

5.3 Limitations and Challenges

Despite the significant findings achieved through the presented studies, several limitations and challenges should be acknowledged. Although the *in vitro* nature of this research offers precise control over experimental conditions, it does not fully recapitulate the complex mechanical environments that cells undergo *in vivo*. For instance, within the tumor microenvironment, dynamic interactions among various cell types and ECM components collectively influence mechanical signaling.

Additionally, acoustic force-based systems are dependent on medium properties such as density and attenuation, however, these parameters vary within complex tissues which may affect the calibration of the applied acoustic forces. Although the presented experimental setup applies acoustic forces of approximately 4000 pN, which is within the biomechanical range in certain key physiological processes such as tumour invasion, the applied forces represent the higher end of this range. While the acoustic force-based platforms are capable of high-throughput and precision, it primarily evaluates tensile forces perpendicular to the adhesion surface. In physiological contexts, cells experience multidirectional forces including compression, shear, and torsion. A more comprehensive understanding of cellular mechanobiology would require integration of diverse force application methods.

Furthermore, while the focus on Piezo1 is justified by its prominent role in mechanotransduction, it only represents one aspect of the cell's intricate mechanosensory system. The interplay between Piezo1 and other mechanosensors, such as integrins, cadherins, and cytoskeletal components, should be further investigated to develop a systems-level understanding of cellular mechanosensing.

5.4 Future Directions

To build on the findings and addressing the limitations of this research, there are several potential avenues for further investigation. Future studies should aim to elucidate the interplay between Piezo1 and other mechanosensory systems, investigating how these components function collectively to orchestrate cellular responses to mechanical stimuli. This could involve simultaneous manipulation of multiple mechanosensors and assessment of downstream signaling integration. Additionally, the mechanoprotective role of Piezo1 warrants exploration in pathological conditions characterized by abnormal mechanical environments, such as cancer, cardiovascular disease, and musculoskeletal disorders. Understanding how alterations in Piezo1 function affect cell survival and behaviour under disease-related mechanical stresses could reveal new therapeutic targets.

Furthermore, developing techniques to monitor and manipulate mechanical forces in living tissues would enable more physiologically relevant studies of

mechanotransduction. Advances in intravital imaging, optogenetics, and biomaterial engineering offer promising approaches for extending mechanobiological investigations to in vivo settings. Additional insights gained into Piezo1 function and CAR T-cell mechanics could inform the development of novel therapeutic strategies. These might include small molecules targeting mechanosensitive ion channels to modify cell adhesion or migration or engineered CAR T cells with optimized mechanical properties for improved tumour targeting. Lastly, continued refinement of acoustic force-based technologies could expand their capabilities, allowing for application of complex force patterns, simultaneous imaging of molecular dynamics, and integration with other analytical techniques such as mass spectrometry or genomic analyses.

5.5 Concluding Remarks

This thesis has contributed to the understanding of cellular mechanobiology by elucidating the multifaceted roles of Piezo1 within cell-matrix interactions and mechanoprotection. It demonstrates the utility of acoustic force-based technologies in quantifying cellular mechanical responses. The findings underscore the fundamental importance of mechanical forces in cellular function and highlight the potential of targeting mechanosensitive pathways for therapeutic interventions. As the understanding of mechanobiology evolves, it is becoming increasingly evident that physical forces are not secondary influences but primary determinants of cellular behaviour in both health and disease. The integration of advanced biophysical techniques with molecular and cellular analyses promises to yield further insights into how cells navigate their mechanical landscapes, opening new avenues for diagnostic and therapeutic innovations.

In conclusion, this thesis establishes a foundation for future investigations at the intersection of mechanobiology, cell biology, and biomedical engineering, contributing to the growing recognition of mechanotransduction as a central principle in biological systems. The continued exploration of how cells sense, respond to, and withstand mechanical forces will undoubtedly enhance our ability to address complex biomedical challenges, from tissue engineering to cancer therapy, through mechanically informed approaches.

Chapter 6: References

[1] Y. Hao, S. Cheng, Y. Tanaka, Y. Hosokawa, Y. Yalikun, and M. Li, 'Mechanical properties of single cells: Measurement methods and applications', *Biotechnol Adv*, vol. 45, p. 107648, Dec. 2020, doi: 10.1016/j.biotechadv.2020.107648.

[2] P. Urdeitx and M. H. Doweidar, 'Single-cell based models for cell–cell and cell–extracellular matrix interactions', in *Digital Human Modeling and Medicine*, Elsevier, 2023, pp. 547–590. doi: 10.1016/B978-0-12-823913-1.00003-8.

[3] P. L. Head, 'Rehabilitation Considerations in Regenerative Medicine', *Phys Med Rehabil Clin N Am*, vol. 27, no. 4, Art. no. 4, Nov. 2016, doi: 10.1016/j.pmr.2016.07.002.

[4] X. Di *et al.*, 'Cellular mechanotransduction in health and diseases: from molecular mechanism to therapeutic targets', *Signal Transduct Target Ther*, vol. 8, no. 1, Art. no. 1, Jul. 2023, doi: 10.1038/s41392-023-01501-9.

[5] K. M. Yamada, A. D. Doyle, and J. Lu, 'Cell-3D matrix interactions: recent advances and opportunities', *Trends Cell Biol*, vol. 32, no. 10, Art. no. 10, Oct. 2022, doi: 10.1016/j.tcb.2022.03.002.

[6] A. Sainio and H. Järveläinen, 'Extracellular matrix-cell interactions: Focus on therapeutic applications', *Cell Signal*, vol. 66, p. 109487, Feb. 2020, doi: 10.1016/j.cellsig.2019.109487.

[7] G. M. Cooper, 'Cell-Cell Interactions', in *The Cell: A Molecular Approach. 2nd edition*, Sinauer Associates, 2000. Accessed: Apr. 10, 2025. [Online]. Available: https://www.ncbi.nlm.nih.gov/books/NBK9851/

[8] Y. Chen, L. Ju, M. Rushdi, C. Ge, and C. Zhu, 'Receptor-mediated cell mechanosensing', *MBoC*, vol. 28, no. 23, pp. 3134–3155, Nov. 2017, doi: 10.1091/mbc.e17-04-0228.

[9] R. O. Hynes, 'Integrins', *Cell*, vol. 110, no. 6, pp. 673–687, Sep. 2002, doi: 10.1016/S0092-8674(02)00971-6.

[10] Y. Chen, Z. Li, and L. A. Ju, 'Tensile and compressive force regulation on cell mechanosensing', *Biophys Rev*, vol. 11, no. 3, pp. 311–318, Jun. 2019, doi: 10.1007/s12551-019-00536-z.

[11] V. Gkretsi and T. Stylianopoulos, 'Cell Adhesion and Matrix Stiffness: Coordinating Cancer Cell Invasion and Metastasis', *Front. Oncol.*, vol. 8, p. 145, May 2018, doi: 10.3389/fonc.2018.00145.

[12] N. E. Reticker-Flynn *et al.*, 'A combinatorial extracellular matrix platform identifies cell-extracellular matrix interactions that correlate with metastasis', *Nat Commun*, vol. 3, no. 1, p. 1122, Oct. 2012, doi: 10.1038/ncomms2128.

[13] Z. L. Zhou, J. Ma, M.-H. Tong, B. P. Chan, A. S. T. Wong, and A. H. W. Ngan, 'Nanomechanical measurement of adhesion and migration of leukemia cells with phorbol 12-myristate 13-acetate treatment', *IJN*, vol. Volume 11, pp. 6533–6545, Dec. 2016, doi: 10.2147/IJN.S118065.

[14] A. J. Garcia and N. D. Gallant, 'Stick and Grip: Measurement Systems and Quantitative Analyses of Integrin-Mediated Cell Adhesion Strength', *CBB*, vol. 39, no. 1, pp. 61–74, 2003, doi: 10.1385/CBB:39:1:61.

[15] H. Wang, F. Zhou, Y. Guo, and L. A. Ju, 'Micropipette-based biomechanical nanotools on living cells', *Eur Biophys J*, vol. 51, no. 2, pp. 119–133, Mar. 2022, doi: 10.1007/s00249-021-01587-5.

[16] N. Nishida-Aoki and T. S. Gujral, 'Emerging approaches to study cell-cell interactions in tumor microenvironment', *Oncotarget*, vol. 10, no. 7, pp. 785–797, Jan. 2019, doi: 10.18632/oncotarget.26585.

[17] P. Beri *et al.*, 'Cell Adhesiveness Serves as a Biophysical Marker for Metastatic Potential', *Cancer Research*, vol. 80, no. 4, pp. 901–911, Feb. 2020, doi: 10.1158/0008-5472.CAN-19-1794.

[18] H. Atcha, Y. S. Choi, O. Chaudhuri, and A. J. Engler, 'Getting physical: Material mechanics is an intrinsic cell cue', *Cell Stem Cell*, vol. 30, no. 6, Art. no. 6, Jun. 2023, doi: 10.1016/j.stem.2023.05.003.

[19] V. Swaminathan and M. Gloerich, 'Decoding mechanical cues by molecular mechanotransduction', *Curr Opin Cell Biol*, vol. 72, pp. 72–80, Oct. 2021, doi: 10.1016/j.ceb.2021.05.006.

[20] A. Chazi, C. Berrier, B. Ajouz, and M. Besnard, 'Mechanosensitive ion channels and their mode of activation', *Biochimie*, vol. 80, no. 5–6, pp. 357–362, May 1998, doi: 10.1016/S0300-9084(00)80003-6.

[21] D. E. Jaalouk and J. Lammerding, 'Mechanotransduction gone awry', *Nature reviews. Molecular cell biology*, vol. 10, no. 1, p. 63, Jan. 2009, doi: 10.1038/nrm2597.

[22] G. Ramaswamy, M. W. Bidez, and C. E. Misch, 'Chapter 6 - Bone Response to Mechanical Loads', in *Dental Implant Prosthetics (Second Edition)*, C. E. Misch, Ed., St. Louis: Mosby, 2015, pp. 107–125. doi: 10.1016/B978-0-323-07845-0.00006-3.

[23] C. T. Mierke, P. Kollmannsberger, D. Paranhos Zitterbart, J. Smith, B. Fabry, and W. H. Goldmann, 'Mechano-Coupling and Regulation of Contractility by the Vinculin Tail Domain', *Biophys J*, vol. 94, no. 2, pp. 661–670, Jan. 2008, doi: 10.1529/biophysj.107.108472.

[24] A. W. Holle and A. J. Engler, 'More Than a Feeling: Discovering, Understanding, and Influencing Mechanosensing Pathways', *Current opinion in biotechnology*, vol. 22, no. 5, p. 648, Apr. 2011, doi: 10.1016/j.copbio.2011.04.007.

[25] K. A. Jansen, P. Atherton, and C. Ballestrem, 'Mechanotransduction at the cell-matrix interface', *Seminars in Cell & Developmental Biology*, vol. 71, pp. 75–83, Nov. 2017, doi: 10.1016/j.semcdb.2017.07.027.

[26] R. Cao, H. Tian, Y. Tian, and X. Fu, 'A Hierarchical Mechanotransduction System: From Macro to Micro', *Adv Sci (Weinh)*, vol. 11, no. 11, p. 2302327, Dec. 2023, doi: 10.1002/advs.202302327.

[27] B. Bakhshandeh *et al.*, 'Mechanotransduction in tissue engineering: Insights into the interaction of stem cells with biomechanical cues', *Experimental Cell Research*, vol. 431, no. 2, p. 113766, Oct. 2023, doi: 10.1016/j.yexcr.2023.113766.

[28] V. D. L. Putra, K. A. Kilian, and M. L. Knothe Tate, 'Biomechanical, biophysical and biochemical modulators of cytoskeletal remodelling and emergent stem cell lineage commitment', *Commun Biol*, vol. 6, no. 1, pp. 1–24, Jan. 2023, doi: 10.1038/s42003-022-04320-w.

[29] D.-H. Kim, P. K. Wong, J. Park, A. Levchenko, and Y. Sun, 'Microengineered Platforms for Cell Mechanobiology', *Annu. Rev. Biomed. Eng.*, vol. 11, no. 1, pp. 203–233, Aug. 2009, doi: 10.1146/annurev-bioeng-061008-124915.

[30] Z. Mai, Y. Lin, P. Lin, X. Zhao, and L. Cui, 'Modulating extracellular matrix stiffness: a strategic approach to boost cancer immunotherapy', *Cell Death Dis*, vol. 15, no. 5, pp. 1–16, May 2024, doi: 10.1038/s41419-024-06697-4.

[31] Y. Jiang, H. Zhang, J. Wang, Y. Liu, T. Luo, and H. Hua, 'Targeting extracellular matrix stiffness and mechanotransducers to improve cancer therapy', *Journal of Hematology & Oncology*, vol. 15, no. 1, p. 34, Mar. 2022, doi: 10.1186/s13045-022-01252-0.

[32] Q. Wei *et al.*, 'Cellular modulation by the mechanical cues from biomaterials for tissue engineering', *Biomater Transl*, vol. 2, no. 4, Art. no. 4, 2021, doi: 10.12336/biomatertransl.2021.04.001.

[33] E. Sitarska and A. Diz-Muñoz, 'Pay attention to membrane tension: Mechanobiology of the cell surface', *Curr Opin Cell Biol*, vol. 66, pp. 11–18, Oct. 2020, doi: 10.1016/j.ceb.2020.04.001.

[34] J. Petzold and E. Gentleman, 'Intrinsic Mechanical Cues and Their Impact on Stem Cells and Embryogenesis', *Front Cell Dev Biol*, vol. 9, p. 761871, Nov. 2021, doi: 10.3389/fcell.2021.761871.

[35] P. Elblová, M. Lunova, A. Dejneka, M. Jirsa, and O. Lunov, 'Impact of mechanical cues on key cell functions and cell-nanoparticle interactions', *Discov Nano*, vol. 19, no. 1, Art. no. 1, Jun. 2024, doi: 10.1186/s11671-024-04052-2.

[36] L. Ju *et al.*, 'Compression force sensing regulates integrin αIIbβ3 adhesive function on diabetic platelets', *Nat Commun*, vol. 9, no. 1, p. 1087, Mar. 2018, doi: 10.1038/s41467-018-03430-6.

[37] B. J. Ballermann, A. Dardik, E. Eng, and A. Liu, 'Shear stress and the endothelium', *Kidney International*, vol. 54, pp. S100–S108, Sep. 1998, doi: 10.1046/j.1523-1755.1998.06720.x.

[38] J. A. Espina, M. H. Cordeiro, M. Milivojevic, I. Pajić-Lijaković, and E. H. Barriga, 'Response of cells and tissues to shear stress', *J Cell Sci*, vol. 136, no. 18, p. jcs260985, Sep. 2023, doi: 10.1242/jcs.260985.

[39] K. Metavarayuth, P. Sitasuwan, X. Zhao, Y. Lin, and Q. Wang, 'Influence of Surface Topographical Cues on the Differentiation of Mesenchymal Stem Cells in Vitro', *ACS Biomater. Sci. Eng.*, vol. 2, no. 2, pp. 142–151, Feb. 2016, doi: 10.1021/acsbiomaterials.5b00377.

[40] H. Ge, M. Tian, Q. Pei, F. Tan, and H. Pei, 'Extracellular Matrix Stiffness: New Areas Affecting Cell Metabolism', *Front Oncol*, vol. 11, p. 631991, Feb. 2021, doi: 10.3389/fonc.2021.631991.

[41] E. H. Barriga and R. Mayor, 'Adjustable viscoelasticity allows for efficient collective cell migration', *Seminars in Cell & Developmental Biology*, vol. 93, pp. 55–68, Sep. 2019, doi: 10.1016/j.semcdb.2018.05.027.

[42] Z. Yang, Y. Wu, L. Yin, and H. Lee Eng, 'Chapter 19 - Impact of Mechanobiological Perturbation in Cartilage Tissue Engineering', in *Advances in Biomechanics and Tissue Regeneration*, M. H. Doweidar, Ed., Academic Press, 2019, pp. 379–392. doi: 10.1016/B978-0-12-816390-0.00019-4.

[43] D. Li and Y. Wang, 'Chapter 14 - Mechanobiology, tissue development, and tissue engineering', in *Principles of Tissue Engineering (Fifth Edition)*, R. Lanza, R. Langer, J. P. Vacanti,

and A. Atala, Eds., Academic Press, 2020, pp. 237–256. doi: 10.1016/B978-0-12-818422-6.00015-0.

[44] B. D. Riehl, J.-H. Park, I. K. Kwon, and J. Y. Lim, 'Mechanical Stretching for Tissue Engineering: Two-Dimensional and Three-Dimensional Constructs', *Tissue Eng Part B Rev*, vol. 18, no. 4, pp. 288–300, Aug. 2012, doi: 10.1089/ten.teb.2011.0465.

[45] C. Schmitter, M. Di-Luoffo, and J. Guillermet-Guibert, 'Transducing compressive forces into cellular outputs in cancer and beyond', *Life Sci Alliance*, vol. 6, no. 9, p. e202201862, Jun. 2023, doi: 10.26508/lsa.202201862.

[46] Y.-Y. Jiang *et al.*, 'BIO alleviated compressive mechanical force-mediated mandibular cartilage pathological changes through Wnt/β-catenin signaling activation', *Journal of Orthopaedic Research*, vol. 36, no. 4, pp. 1228–1237, 2018, doi: 10.1002/jor.23748.

[47] H. Cheng *et al.*, 'Effects of shear stress on vascular endothelial functions in atherosclerosis and potential therapeutic approaches', *Biomedicine & Pharmacotherapy*, vol. 158, p. 114198, Feb. 2023, doi: 10.1016/j.biopha.2022.114198.

[48] J. Zhou, Y.-S. Li, and S. Chien, 'Shear stress-initiated signaling and its regulation of endothelial function', *Arterioscler Thromb Vasc Biol*, vol. 34, no. 10, pp. 2191–2198, Oct. 2014, doi: 10.1161/ATVBAHA.114.303422.

[49] L. Hajra, A. I. Evans, M. Chen, S. J. Hyduk, T. Collins, and M. I. Cybulsky, 'The NF-κB signal transduction pathway in aortic endothelial cells is primed for activation in regions predisposed to atherosclerotic lesion formation', *Proceedings of the National Academy of Sciences*, vol. 97, no. 16, pp. 9052–9057, Aug. 2000, doi: 10.1073/pnas.97.16.9052.

[50] B. K. K. Teo *et al.*, 'Nanotopography Modulates Mechanotransduction of Stem Cells and Induces Differentiation through Focal Adhesion Kinase', *ACS Nano*, vol. 7, no. 6, pp. 4785–4798, Jun. 2013, doi: 10.1021/nn304966z.

[51] B. Alberts, A. Johnson, J. Lewis, M. Raff, K. Roberts, and P. Walter, 'Cell-Cell Adhesion', in *Molecular Biology of the Cell. 4th edition*, Garland Science, 2002. Accessed: Apr. 21, 2025. [Online]. Available: https://www.ncbi.nlm.nih.gov/books/NBK26937/

[52] E. H. J. Danen, 'Integrins: An Overview of Structural and Functional Aspects', in *Madame Curie Bioscience Database [Internet]*, Landes Bioscience, 2013. Accessed: Apr. 21, 2025. [Online]. Available: https://www.ncbi.nlm.nih.gov/books/NBK6259/

[53] X. Pang *et al.*, 'Targeting integrin pathways: mechanisms and advances in therapy', *Sig Transduct Target Ther*, vol. 8, no. 1, pp. 1–42, Jan. 2023, doi: 10.1038/s41392-022-01259-6.

[54] D. E. Leckband, Q. le Duc, N. Wang, and J. de Rooij, 'Mechanotransduction at cadherin-mediated adhesions', *Curr Opin Cell Biol*, vol. 23, no. 5, pp. 523–530, Oct. 2011, doi: 10.1016/j.ceb.2011.08.003.

[55] Z. Zhang *et al.*, 'Programmable integrin and N-cadherin adhesive interactions modulate mechanosensing of mesenchymal stem cells by cofilin phosphorylation', *Nat Commun*, vol. 13, no. 1, p. 6854, Nov. 2022, doi: 10.1038/s41467-022-34424-0.

[56] T. Shemesh, B. Geiger, A. D. Bershadsky, and M. M. Kozlov, 'Focal adhesions as mechanosensors: A physical mechanism', *Proceedings of the National Academy of Sciences*, vol. 102, no. 35, pp. 12383–12388, Aug. 2005, doi: 10.1073/pnas.0500254102.

[57] J.-C. Kuo, 'Focal adhesions function as a mechanosensor', *Prog Mol Biol Transl Sci*, vol. 126, pp. 55–73, 2014, doi: 10.1016/B978-0-12-394624-9.00003-8.

[58] M. Janiszewska, M. C. Primi, and T. Izard, 'Cell adhesion in cancer: Beyond the migration of single cells', *Journal of Biological Chemistry*, vol. 295, no. 8, pp. 2495–2505, Feb. 2020, doi: 10.1074/jbc.REV119.007759.

[59] Á. Otero-Sobrino, P. Blanco-Carlón, M. Á. Navarro-Aguadero, M. Gallardo, J. Martínez-López, and M. Velasco-Estévez, 'Mechanosensitive Ion Channels: Their Physiological Importance and Potential Key Role in Cancer', *Int J Mol Sci*, vol. 24, no. 18, Art. no. 18, Sep. 2023, doi: 10.3390/ijms241813710.

[60] B. Martinac, 'Mechanosensitive ion channels', *Channels (Austin)*, vol. 6, no. 4, pp. 211–213, Jul. 2012, doi: 10.4161/chan.22047.

[61] H. Liu *et al.*, 'Piezo1 Channels as Force Sensors in Mechanical Force-Related Chronic Inflammation', *Front. Immunol.*, vol. 13, Jan. 2022, doi: 10.3389/fimmu.2022.816149.

[62] S. S. Ranade, R. Syeda, and A. Patapoutian, 'Mechanically Activated Ion Channels', *Neuron*, vol. 87, no. 6, pp. 1162–1179, Sep. 2015, doi: 10.1016/j.neuron.2015.08.032.

[63] Y.-C. Chuang and C.-C. Chen, 'Force From Filaments: The Role of the Cytoskeleton and Extracellular Matrix in the Gating of Mechanosensitive Channels', *Front. Cell Dev. Biol.*, vol. 10, May 2022, doi: 10.3389/fcell.2022.886048.

[64] J. L. Nourse and M. M. Pathak, 'How cells channel their stress: Interplay between Piezo1 and the cytoskeleton', *Seminars in Cell & Developmental Biology*, vol. 71, pp. 3–12, Nov. 2017, doi: 10.1016/j.semcdb.2017.06.018.

[65] N. Bavi, C. D. Cox, Y. A. Nikolaev, and B. Martinac, 'Molecular insights into the force-from-lipids gating of mechanosensitive channels', *Current Opinion in Physiology*, vol. 36, p. 100706, Dec. 2023, doi: 10.1016/j.cophys.2023.100706.

[66] J. Li *et al.*, 'Piezo1 integration of vascular architecture with physiological force', *Nature*, vol. 515, no. 7526, pp. 279–282, Nov. 2014, doi: 10.1038/nature13701.

[67] L. John, N. L. Ko, A. Gokin, N. Gokina, M. Mandalà, and G. Osol, 'The Piezo1 cation channel mediates uterine artery shear stress mechanotransduction and vasodilation during rat pregnancy', *American Journal of Physiology-Heart and Circulatory Physiology*, vol. 315, no. 4, pp. H1019–H1026, Oct. 2018, doi: 10.1152/ajpheart.00103.2018.

[68] S. Wang, R. Chennupati, H. Kaur, A. Iring, N. Wettschureck, and S. Offermanns, 'Endothelial cation channel PIEZO1 controls blood pressure by mediating flow-induced ATP release', *J Clin Invest*, vol. 126, no. 12, pp. 4527–4536, Dec. 2016, doi: 10.1172/JCI87343.

[69] A. Lhomme *et al.*, 'Stretch-activated Piezo1 Channel in Endothelial Cells Relaxes Mouse Intrapulmonary Arteries', *Am J Respir Cell Mol Biol*, vol. 60, no. 6, pp. 650–658, Jun. 2019, doi: 10.1165/rcmb.2018-0197OC.

[70] K. Retailleau *et al.*, 'Piezo1 in Smooth Muscle Cells Is Involved in Hypertension-Dependent Arterial Remodeling', *Cell Reports*, vol. 13, no. 6, pp. 1161–1171, Nov. 2015, doi: 10.1016/j.celrep.2015.09.072.

[71] S. M. Cahalan, V. Lukacs, S. S. Ranade, S. Chien, M. Bandell, and A. Patapoutian, 'Piezo1 links mechanical forces to red blood cell volume', *eLife*, vol. 4, p. e07370, May 2015, doi: 10.7554/eLife.07370.

[72] E. Cinar, S. Zhou, J. DeCourcey, Y. Wang, R. E. Waugh, and J. Wan, 'Piezo1 regulates mechanotransductive release of ATP from human RBCs', *Proceedings of the National Academy of Sciences*, vol. 112, no. 38, pp. 11783–11788, Sep. 2015, doi: 10.1073/pnas.1507309112.

[73] M. M. Pathak *et al.*, 'Stretch-activated ion channel Piezo1 directs lineage choice in human neural stem cells', *Proceedings of the National Academy of Sciences*, vol. 111, no. 45, pp. 16148–16153, Nov. 2014, doi: 10.1073/pnas.1409802111.

[74] N. R. Blumenthal, O. Hermanson, B. Heimrich, and V. P. Shastri, 'Stochastic nanoroughness modulates neuron–astrocyte interactions and function via mechanosensing cation channels', *Proceedings of the National Academy of Sciences*, vol. 111, no. 45, pp. 16124–16129, Nov. 2014, doi: 10.1073/pnas.1412740111.

[75] K. Lang, H. Breer, and C. Frick, 'Mechanosensitive ion channel Piezo1 is expressed in antral G cells of murine stomach', *Cell Tissue Res*, vol. 371, no. 2, pp. 251–260, Feb. 2018, doi: 10.1007/s00441-017-2755-0.

[76] M. Zhong *et al.*, 'Alveolar Stretch Activation of Endothelial Piezo1 Protects Adherens Junctions and Lung Vascular Barrier', *Am J Respir Cell Mol Biol*, vol. 62, no. 2, pp. 168–177, Feb. 2020, doi: 10.1165/rcmb.2019-0024OC.

[77] E. E. Friedrich *et al.*, 'Endothelial cell Piezo1 mediates pressure-induced lung vascular hyperpermeability via disruption of adherens junctions', *Proceedings of the National Academy of Sciences*, vol. 116, no. 26, pp. 12980–12985, Jun. 2019, doi: 10.1073/pnas.1902165116.

[78] G.-P. Liang *et al.*, 'Piezo1 induced apoptosis of type II pneumocytes during ARDS', *Respir Res*, vol. 20, no. 1, p. 118, Jun. 2019, doi: 10.1186/s12931-019-1083-1.

[79] T. Miyamoto *et al.*, 'Functional Role for Piezo1 in Stretch-evoked Ca2+ Influx and ATP Release in Urothelial Cell Cultures *', *Journal of Biological Chemistry*, vol. 289, no. 23, pp. 16565–16575, Jun. 2014, doi: 10.1074/jbc.M113.528638.

[80] K. Hasegawa, S. Fujii, S. Matsumoto, Y. Tajiri, A. Kikuchi, and T. Kiyoshima, 'YAP signaling induces PIEZO1 to promote oral squamous cell carcinoma cell proliferation', *The Journal of Pathology*, vol. 253, no. 1, pp. 80–93, 2021, doi: 10.1002/path.5553.

[81] Y. Han *et al.*, 'Mechanosensitive ion channel Piezo1 promotes prostate cancer development through the activation of the Akt/mTOR pathway and acceleration of cell cycle', *Int J Oncol*, Jul. 2019, doi: 10.3892/ijo.2019.4839.

[82] Y. Sun *et al.*, 'The function of Piezo1 in colon cancer metastasis and its potential regulatory mechanism', *J Cancer Res Clin Oncol*, vol. 146, no. 5, pp. 1139–1152, May 2020, doi: 10.1007/s00432-020-03179-w.

[83] F. Wang *et al.*, 'Mechanosensitive ion channel Piezo2 is important for enterochromaffin cell response to mechanical forces', *The Journal of Physiology*, vol. 595, no. 1, pp. 79–91, 2017, doi: 10.1113/JP272718.

[84] K. Nonomura *et al.*, 'Piezo2 senses airway stretch and mediates lung inflation-induced apnoea', *Nature*, vol. 541, no. 7636, pp. 176–181, Jan. 2017, doi: 10.1038/nature20793.

[85] A. T. Chesler *et al.*, 'The Role of PIEZO2 in Human Mechanosensation', *New England Journal of Medicine*, vol. 375, no. 14, pp. 1355–1364, Oct. 2016, doi: 10.1056/NEJMoa1602812.

[86] K. L. Marshall *et al.*, 'PIEZO2 in sensory neurons and urothelial cells coordinates urination', *Nature*, vol. 588, no. 7837, pp. 290–295, Dec. 2020, doi: 10.1038/s41586-020-2830-7.

[87] E. A. Wehrwein and M. J. Joyner, 'Chapter 8 - Regulation of blood pressure by the arterial baroreflex and autonomic nervous system', in *Handbook of Clinical Neurology*, vol. 117, R. M. Buijs and D. F. Swaab, Eds., in Autonomic Nervous System, vol. 117. , Elsevier, 2013, pp. 89–102. doi: 10.1016/B978-0-444-53491-0.00008-0.

[88] H. R. Kirchheim, 'Systemic arterial baroreceptor reflexes', *Physiological Reviews*, vol. 56, no. 1, pp. 100–177, Jan. 1976, doi: 10.1152/physrev.1976.56.1.100.

[89] W.-Z. Zeng *et al.*, 'PIEZOs mediate neuronal sensing of blood pressure and the baroreceptor reflex', *Science*, vol. 362, no. 6413, pp. 464–467, Oct. 2018, doi: 10.1126/science.aau6324.

[90] J. B. Fitzgerald, M. Jin, D. Dean, D. J. Wood, M. H. Zheng, and A. J. Grodzinsky, 'Mechanical Compression of Cartilage Explants Induces Multiple Time-dependent Gene Expression Patterns and Involves Intracellular Calcium and Cyclic AMP *', *Journal of Biological Chemistry*, vol. 279, no. 19, pp. 19502–19511, May 2004, doi: 10.1074/jbc.M400437200.

[91] W. Lee *et al.*, 'Synergy between Piezo1 and Piezo2 channels confers high-strain mechanosensitivity to articular cartilage', *Proceedings of the National Academy of Sciences*, vol. 111, no. 47, pp. E5114–E5122, Nov. 2014, doi: 10.1073/pnas.1414298111.

[92] I. P. Uray and K. Uray, 'Mechanotransduction at the Plasma Membrane-Cytoskeleton Interface', *Int J Mol Sci*, vol. 22, no. 21, p. 11566, Oct. 2021, doi: 10.3390/ijms222111566.

[93] W. Lee, 'The Cytoskeleton and Its Binding Proteins as Mechanosensors, Transducers, and Functional Regulators of Cells', *Int J Mol Sci*, vol. 25, no. 1, p. 172, Dec. 2023, doi: 10.3390/ijms25010172.

[94] Z. Kechagia and P. Roca-Cusachs, 'Cytoskeletal safeguards: Protecting the nucleus from mechanical perturbations', *Current Opinion in Biomedical Engineering*, vol. 28, p. 100494, Dec. 2023, doi: 10.1016/j.cobme.2023.100494.

[95] T. J. Kirby and J. Lammerding, 'Emerging views of the nucleus as a cellular mechanosensor', *Nat Cell Biol*, vol. 20, no. 4, pp. 373–381, Apr. 2018, doi: 10.1038/s41556-018-0038-y.

[96] J. M. Ross, 'Chapter II. 1 - Cell-Extracellular Matrix Interactions', in *Frontiers in Tissue Engineering*, C. W. Patrick, A. G. Mikos, L. V. McIntire, and R. S. Langer, Eds., Oxford: Pergamon, 1998, pp. 15–27. doi: 10.1016/B978-008042689-1/50004-2.

[97] K. A. DeMali and J. C. Adams, 'Cell–cell and cell–matrix interactions', *MBoC*, vol. 23, no. 6, pp. 965–965, Mar. 2012, doi: 10.1091/mbc.e11-12-0967.

[98] C. Underhill, 'CD44: The hyaluronan receptor', *Journal of Cell Science*, vol. 103, no. 2, pp. 293–298, Oct. 1992, doi: 10.1242/jcs.103.2.293.

[99] J. D. Johnson, J. C. Edman, and W. J. Rutter, 'A receptor tyrosine kinase found in breast carcinoma cells has an extracellular discoidin I-like domain.', *Proceedings of the National Academy of Sciences*, vol. 90, no. 22, p. 10891, Nov. 1993, doi: 10.1073/pnas.90.22.10891.

[100] S.-H. Kim, J. Turnbull, and S. Guimond, 'Extracellular matrix and cell signalling: the dynamic cooperation of integrin, proteoglycan and growth factor receptor', *J Endocrinol*, vol. 209, no. 2, pp. 139–151, May 2011, doi: 10.1530/joe-10-0377.

[101] S. R. Goodman, Ed., 'Cell Adhesion and the Extracellular Matrix', in *Goodman's Medical Cell Biology (Fourth Edition)*, Academic Press, 2021, pp. 203–247. doi: 10.1016/B978-0-12-817927-7.00007-7.

[102] D. E. Ingber, 'Cellular mechanotransduction: putting all the pieces together again', *FASEB J*, vol. 20, no. 7, pp. 811–827, May 2006, doi: 10.1096/fj.05-5424rev.

[103] E. Armingol, A. Officer, O. Harismendy, and N. E. Lewis, 'Deciphering cell–cell interactions and communication from gene expression', *Nat Rev Genet*, vol. 22, no. 2, pp. 71–88, Feb. 2021, doi: 10.1038/s41576-020-00292-x.

[104] K. Goodwin, E. E. Lostchuck, K. M. L. Cramb, T. Zulueta-Coarasa, R. Fernandez-Gonzalez, and G. Tanentzapf, 'Cell–cell and cell–extracellular matrix adhesions cooperate to organize actomyosin networks and maintain force transmission during dorsal closure', *Mol Biol Cell*, vol. 28, no. 10, pp. 1301–1310, May 2017, doi: 10.1091/mbc.E17-01-0033.

[105] I. Valiente-Alandi, A. E. Schafer, and B. C. Blaxall, 'Extracellular matrix-mediated cellular communication in the heart', *J Mol Cell Cardiol*, vol. 91, pp. 228–237, Feb. 2016, doi: 10.1016/j.yjmcc.2016.01.011.

[106] C. M. Howard and T. A. Baudino, 'Dynamic cell–cell and cell–ECM interactions in the heart', *Journal of Molecular and Cellular Cardiology*, vol. 70, pp. 19–26, May 2014, doi: 10.1016/j.yjmcc.2013.10.006.

[107] E. Evans and P. Williams, 'Dynamic Force Spectroscopy', in *Physics of bio-molecules and cells. Physique des biomolécules et des cellules*, F. Flyvbjerg, F. Jülicher, P. Ormos, and F. David, Eds., Berlin, Heidelberg: Springer, 2002, pp. 145–204. doi: 10.1007/3-540-45701-1_4.

[108] M. Evstigneev and P. Reimann, 'Dynamic force spectroscopy: Optimized data analysis', *Phys. Rev. E*, vol. 68, no. 4, Art. no. 4, Oct. 2003, doi: 10.1103/PhysRevE.68.045103.

[109] E. Evans, 'Looking inside molecular bonds at biological interfaces with dynamic force spectroscopy', *Biophys Chem*, vol. 82, no. 2–3, Art. no. 2–3, Dec. 1999, doi: 10.1016/s0301-4622(99)00108-8.

[110] C. Kasper, D. Egger, and A. Lavrentieva, Eds., *Basic Concepts on 3D Cell Culture*. in Learning Materials in Biosciences. Cham: Springer International Publishing, 2021. doi: 10.1007/978-3-030-66749-8.

[111] H. Clausen-Schaumann, M. Seitz, R. Krautbauer, and H. E. Gaub, 'Force spectroscopy with single bio-molecules', *Current Opinion in Chemical Biology*, vol. 4, no. 5, pp. 524–530, Oct. 2000, doi: 10.1016/S1367-5931(00)00126-5.

[112] R. Merkel, P. Nassoy, A. Leung, K. Ritchie, and E. Evans, 'Energy landscapes of receptor-ligand bonds explored with dynamic force spectroscopy', *Nature*, vol. 397, no. 6714, Art. no. 6714, Jan. 1999, doi: 10.1038/16219.

[113] T. Strunz, K. Oroszlan, R. Schäfer, and H. J. Güntherodt, 'Dynamic force spectroscopy of single DNA molecules', *Proc Natl Acad Sci U S A*, vol. 96, no. 20, Art. no. 20, Sep. 1999, doi: 10.1073/pnas.96.20.11277.

[114] J. T. Bullerjahn, S. Sturm, and K. Kroy, 'Theory of rapid force spectroscopy', *Nat Commun*, vol. 5, p. 4463, Jul. 2014, doi: 10.1038/ncomms5463.

[115] J. Hristov, 'Energies of Mechanical Fractional-Order Elements: Causal Concept and Kernel Effects', *Applied Sciences*, vol. 14, no. 1, Art. no. 1, Jan. 2024, doi: 10.3390/app14010197.

[116] D. B. Staple, F. Hanke, and H. J. Kreuzer, 'Dynamics of single-molecule force-ramp experiments: The role of fluctuations', *Phys. Rev. E*, vol. 77, no. 2, p. 021801, Feb. 2008, doi: 10.1103/PhysRevE.77.021801.

[117] M. Schlierf, H. Li, and J. M. Fernandez, 'The unfolding kinetics of ubiquitin captured with single-molecule force-clamp techniques', *Proc Natl Acad Sci U S A*, vol. 101, no. 19, pp. 7299–7304, May 2004, doi: 10.1073/pnas.0400033101.

[118] A. Taninaka, Y. Hirano, O. Takeuchi, and H. Shigekawa, 'Force Measurement Enabling Precise Analysis by Dynamic Force Spectroscopy', *Int J Mol Sci*, vol. 13, no. 1, Art. no. 1, Dec. 2011, doi: 10.3390/ijms13010453.

[119] K. C. Neuman and A. Nagy, 'Single-molecule force spectroscopy: optical tweezers, magnetic tweezers and atomic force microscopy', *Nat Methods*, vol. 5, no. 6, Art. no. 6, Jun. 2008, doi: 10.1038/nmeth.1218.

[120] L. Ju, 'Dynamic Force Spectroscopy Analysis on the Redox States of Protein Disulphide Bonds', *Methods Mol Biol*, vol. 1967, pp. 115–131, 2019, doi: 10.1007/978-1-4939-9187-7_7.

[121] O. Takeuchi *et al.*, 'Dynamic-force spectroscopy measurement with precise force control using atomic-force microscopy probe', *Journal of Applied Physics*, vol. 100, no. 7, Art. no. 7, Oct. 2006, doi: 10.1063/1.2355432.

[122] S. M. Altmann and P. F. Lenne, 'Forced unfolding of single proteins', *Methods Cell Biol*, vol. 68, pp. 311–335, 2002, doi: 10.1016/s0091-679x(02)68016-1.

[123] C. Gourier, A. Jegou, J. Husson, and F. Pincet, 'A Nanospring Named Erythrocyte. The Biomembrane Force Probe', *Cel. Mol. Bioeng.*, vol. 1, no. 4, pp. 263–275, Dec. 2008, doi: 10.1007/s12195-008-0030-x.

[124] H. Wang *et al.*, 'Fluorescence-coupled micropipette aspiration assay to examine calcium mobilization caused by red blood cell mechanosensing', *Eur Biophys J*, vol. 51, no. 2, pp. 135–146, Mar. 2022, doi: 10.1007/s00249-022-01595-z.

[125] C. J. Bustamante, Y. R. Chemla, S. Liu, and M. D. Wang, 'Optical tweezers in single-molecule biophysics', *Nat Rev Methods Primers*, vol. 1, no. 1, pp. 1–29, Mar. 2021, doi: 10.1038/s43586-021-00021-6.

[126] R. Tapia-Rojo, M. Mora, and S. Garcia-Manyes, 'Single-molecule magnetic tweezers to probe the equilibrium dynamics of individual proteins at physiologically relevant forces and timescales', *Nat Protoc*, vol. 19, no. 6, pp. 1779–1806, Jun. 2024, doi: 10.1038/s41596-024-00965-5.

[127] Y. Cao and H. Li, 'Single-Molecule Force-Clamp Spectroscopy: Dwell Time Analysis and Practical Considerations', *Langmuir*, vol. 27, no. 4, pp. 1440–1447, Feb. 2011, doi: 10.1021/la104130n.

[128] G. Sitters, D. Kamsma, G. Thalhammer, M. Ritsch-Marte, E. J. G. Peterman, and G. J. L. Wuite, 'Acoustic force spectroscopy', *Nat Methods*, vol. 12, no. 1, pp. 47–50, Jan. 2015, doi: 10.1038/nmeth.3183.

[129] D. Yang, A. Ward, K. Halvorsen, and W. P. Wong, 'Multiplexed single-molecule force spectroscopy using a centrifuge', *Nat Commun*, vol. 7, no. 1, p. 11026, Mar. 2016, doi: 10.1038/ncomms11026.

[130] S. V. Plotnikov, B. Sabass, U. S. Schwarz, and C. M. Waterman, 'Chapter 20 - High-Resolution Traction Force Microscopy', in *Methods in Cell Biology*, vol. 123, J. C. Waters and T. Wittman, Eds., in Quantitative Imaging in Cell Biology, vol. 123. , Academic Press, 2014, pp. 367–394. doi: 10.1016/B978-0-12-420138-5.00020-3.

[131] M. R. Pawlak *et al.*, 'RAD-TGTs: high-throughput measurement of cellular mechanotype via rupture and delivery of DNA tension probes', *Nat Commun*, vol. 14, no. 1, Art. no. 1, Apr. 2023, doi: 10.1038/s41467-023-38157-6.

[132] D. Kamsma, R. Creyghton, G. Sitters, G. J. L. Wuite, and E. J. G. Peterman, 'Tuning the Music: Acoustic Force Spectroscopy (AFS) 2.0', *Methods*, vol. 105, pp. 26–33, Aug. 2016, doi: 10.1016/j.ymeth.2016.05.002.

[133] D. Kamsma *et al.*, 'Single-Cell Acoustic Force Spectroscopy: Resolving Kinetics and Strength of T Cell Adhesion to Fibronectin', *Cell Rep*, vol. 24, no. 11, Art. no. 11, Sep. 2018, doi: 10.1016/j.celrep.2018.08.034.

[134] H. Tanaka, K. Funayama, and Y. Tadokoro, 'Periodic switching of acoustic radiation force with beat created by multitone field', *Sci Rep*, vol. 12, no. 1, Art. no. 1, Sep. 2022, doi: 10.1038/s41598-022-19077-9.

[135] A. Lenshof and T. Laurell, 'Acoustic Contrast Factor', in *Encyclopedia of Nanotechnology*, B. Bhushan, Ed., Dordrecht: Springer Netherlands, 2012, pp. 30–31. doi: 10.1007/978-90-481-9751-4_425.

[136] K. Dholakia, B. W. Drinkwater, and M. Ritsch-Marte, 'Comparing acoustic and optical forces for biomedical research', *Nat Rev Phys*, vol. 2, no. 9, Art. no. 9, Aug. 2020, doi: 10.1038/s42254-020-0215-3.

[137] O. A. Sapozhnikov and M. R. Bailey, 'Radiation force of an arbitrary acoustic beam on an elastic sphere in a fluid', *J Acoust Soc Am*, vol. 133, no. 2, Art. no. 2, Feb. 2013, doi: 10.1121/1.4773924.

[138] Y. J. Wang *et al.*, 'Combining DNA scaffolds and acoustic force spectroscopy to characterize individual protein bonds', *Biophys J*, vol. 122, no. 12, pp. 2518–2530, Jun. 2023, doi: 10.1016/j.bpj.2023.05.004.

[139] K.-K. H. Taris, D. Kamsma, and G. J. L. Wuite, 'Single-Cell Measurements Using Acoustic Force Spectroscopy (AFS)', *Methods Mol Biol*, vol. 2694, pp. 467–477, 2024, doi: 10.1007/978-1-0716-3377-9_22.

[140] R. Sorkin *et al.*, 'Probing cellular mechanics with acoustic force spectroscopy', *MBoC*, vol. 29, no. 16, pp. 2005–2011, Aug. 2018, doi: 10.1091/mbc.E18-03-0154.

[141] E. L. Upp and P. J. LaNasa, 'CHAPTER 2 - Basic Flow Measurement Laws', in *Fluid Flow Measurement (Second Edition)*, E. L. Upp and P. J. LaNasa, Eds., Woburn: Gulf Professional Publishing, 2002, pp. 24–34. doi: 10.1016/B978-088415758-8/50003-X.

[142] T. Tél and Y.-C. Lai, 'Chaotic transients in spatially extended systems', *Physics Reports*, vol. 460, no. 6, Art. no. 6, May 2008, doi: 10.1016/j.physrep.2008.01.001.

[143] B. E. Rapp, 'Chapter 9 - Fluids', in *Microfluidics: Modelling, Mechanics and Mathematics*, B. E. Rapp, Ed., in Micro and Nano Technologies. , Oxford: Elsevier, 2017, pp. 243–263. doi: 10.1016/B978-1-4557-3141-1.50009-5.

[144] S. A. J. Watkin, A. Hashemi, D. R. Thomson, F. G. Pearce, R. C. J. Dobson, and V. M. Nock, 'Chapter Three - Laminar flow-based microfluidic systems for molecular interaction analysis—Part 1: Chip development, system operation and measurement setup', in *Methods in Enzymology*, vol. 682, A. K. Shukla, Ed., in Integrated Methods in Protein Biochemistry: Part C, vol. 682. , Academic Press, 2023, pp. 53–100. doi: 10.1016/bs.mie.2022.12.001.

[145] Z. Li, A. Venkataraman, M. A. Rosenbaum, and L. T. Angenent, 'A laminar-flow microfluidic device for quantitative analysis of microbial electrochemical activity', *ChemSusChem*, vol. 5, no. 6, pp. 1119–1123, Jun. 2012, doi: 10.1002/cssc.201100736.

[146] F. Meng, H. Cheng, J. Qian, X. Dai, Y. Huang, and Y. Fan, 'In vitro fluidic systems: Applying shear stress on endothelial cells', *Medicine in Novel Technology and Devices*, vol. 15, p. 100143, Sep. 2022, doi: 10.1016/j.medntd.2022.100143.

[147] N. Korin *et al.*, 'Shear-activated nanotherapeutics for drug targeting to obstructed blood vessels', *Science*, vol. 337, no. 6095, pp. 738–742, Aug. 2012, doi: 10.1126/science.1217815.

[148] J. Su *et al.*, 'Cell–cell communication: new insights and clinical implications', *Sig Transduct Target Ther*, vol. 9, no. 1, pp. 1–52, Aug. 2024, doi: 10.1038/s41392-024-01888-z.

[149] J. Fares, M. Y. Fares, H. H. Khachfe, H. A. Salhab, and Y. Fares, 'Molecular principles of metastasis: a hallmark of cancer revisited', *Sig Transduct Target Ther*, vol. 5, no. 1, p. 28, Mar. 2020, doi: 10.1038/s41392-020-0134-x.

[150] D. R. Bielenberg and B. R. Zetter, 'The Contribution of Angiogenesis to the Process of Metastasis', *Cancer J*, vol. 21, no. 4, pp. 267–273, 2015, doi: 10.1097/PPO.0000000000000138.

[151] A. Labani-Motlagh, M. Ashja-Mahdavi, and A. Loskog, 'The Tumor Microenvironment: A Milieu Hindering and Obstructing Antitumor Immune Responses', *Front. Immunol.*, vol. 11, p. 940, May 2020, doi: 10.3389/fimmu.2020.00940.

[152] LUMICKS, 'z-Movi® Cell Avidity Analyzer'. 2022. Accessed: May 05, 2023. [Online]. Available: https://lumicks.com/products/z-movi-cell-avidity-analyzer/

[153] LUMICKS, *Analyzing Cell Avidity | LUMICKS z-Movi*, (Jan. 26, 2022). Accessed: May 05, 2023. [Online Video]. Available: https://www.youtube.com/watch?v=tgpGWM4AOsY

[154] R. C. Sterner and R. M. Sterner, 'CAR-T cell therapy: current limitations and potential strategies', *Blood Cancer J.*, vol. 11, no. 4, pp. 1–11, Apr. 2021, doi: 10.1038/s41408-021-00459-7.

[155] C. Y. Slaney, M. H. Kershaw, and P. K. Darcy, 'Trafficking of T Cells into Tumors', *Cancer Research*, vol. 74, no. 24, pp. 7168–7174, Dec. 2014, doi: 10.1158/0008-5472.CAN-14-2458.

[156] J. Seigner *et al.*, 'Solving the mystery of the FMC63-CD19 affinity', *Sci Rep*, vol. 13, no. 1, p. 23024, Dec. 2023, doi: 10.1038/s41598-023-48528-0.

[157] W. Wels, I. M. Harwerth, M. Mueller, B. Groner, and N. E. Hynes, 'Selective inhibition of tumor cell growth by a recombinant single-chain antibody-toxin specific for the erbB-2 receptor', *Cancer Res*, vol. 52, no. 22, pp. 6310–6317, Nov. 1992.

[158] R. Mao, W. Kong, and Y. He, 'The affinity of antigen-binding domain on the antitumor efficacy of CAR T cells: Moderate is better', *Front. Immunol.*, vol. 13, Oct. 2022, doi: 10.3389/fimmu.2022.1032403.

[159] Y. Wang, J. Jin, H. J. Wang, and L. A. Ju, 'Acoustic Force-Based Cell–Matrix Avidity Measurement in High Throughput', *Biosensors*, vol. 13, no. 1, p. 95, Jan. 2023, doi: 10.3390/bios13010095.

[160] M. B. Leick *et al.*, 'Non-cleavable hinge enhances avidity and expansion of CAR-T cells for acute myeloid leukemia', *Cancer Cell*, vol. 40, no. 5, pp. 494-508.e5, May 2022, doi: 10.1016/j.ccell.2022.04.001.

[161] B. Salzer *et al.*, 'Engineering AvidCARs for combinatorial antigen recognition and reversible control of CAR function', *Nat Commun*, vol. 11, no. 1, p. 4166, Aug. 2020, doi: 10.1038/s41467-020-17970-3.

[162] L. Lee *et al.*, 'Limited efficacy of APRIL CAR in patients with multiple myeloma indicate challenges in the use of natural ligands for CAR T-cell therapy', *J Immunother Cancer*, vol. 11, no. 6, p. e006699, Jun. 2023, doi: 10.1136/jitc-2023-006699.

[163] P. Wang, J. Li, and Q. Wei, 'Understanding the interplay between cell force and cell adhesion processes', *Engineered Regeneration*, vol. 4, no. 3, pp. 277–288, Sep. 2023, doi: 10.1016/j.engreg.2023.04.002.

[164] K. D. Sumigray and T. Lechler, 'Chapter Twelve - Cell Adhesion in Epidermal Development and Barrier Formation', in *Current Topics in Developmental Biology*, vol. 112, A. S. Yap, Ed., in Cellular Adhesion in Development and Disease, vol. 112. , Academic Press, 2015, pp. 383–414. doi: 10.1016/bs.ctdb.2014.11.027.

[165] L. Borsig and H. Läubli, 'Cell Adhesion During Tumorigenesis and Metastasis', in *Encyclopedia of Cancer (Third Edition)*, P. Boffetta and P. Hainaut, Eds., Oxford: Academic Press, 2019, pp. 307–314. doi: 10.1016/B978-0-12-801238-3.64991-7.

[166] A. Ahmad Khalili and M. R. Ahmad, 'A Review of Cell Adhesion Studies for Biomedical and Biological Applications', *Int J Mol Sci*, vol. 16, no. 8, pp. 18149–18184, Aug. 2015, doi: 10.3390/ijms160818149.

[167] M. Yao *et al.*, 'Force- and cell state–dependent recruitment of Piezo1 drives focal adhesion dynamics and calcium entry', *Sci. Adv.*, vol. 8, no. 45, Art. no. 45, Nov. 2022, doi: 10.1126/sciadv.abo1461.

[168] M. Yao *et al.*, 'Force-dependent recruitment of Piezo1 drives adhesion maturation and calcium entry in normal but not tumor cells', Mar. 09, 2020. doi: 10.1101/2020.03.09.972307.

[169] D. Cheng, J. Wang, M. Yao, and C. D. Cox, 'Joining forces: crosstalk between mechanosensitive PIEZO1 ion channels and integrin-mediated focal adhesions', *Biochemical Society Transactions*, vol. 51, no. 5, Art. no. 5, 2023, doi: 10.1042/BST20230042.

[170] D. Jetta, M. R. Bahrani Fard, F. Sachs, K. Munechika, and S. Z. Hua, 'Adherent cell remodeling on micropatterns is modulated by Piezo1 channels', *Sci Rep*, vol. 11, no. 1, p. 5088, Mar. 2021, doi: 10.1038/s41598-021-84427-y.

[171] Y. Pan *et al.*, 'Mechanosensor Piezo1 mediates bimodal patterns of intracellular calcium and FAK signaling', *EMBO J*, vol. 41, no. 17, p. e111799, Jul. 2022, doi: 10.15252/embj.2022111799.

[172] C. Hogan, 'Impact of interactions between normal and transformed epithelial cells and the relevance to cancer', *Cell Mol Life Sci*, vol. 69, no. 2, pp. 203–213, Aug. 2011, doi: 10.1007/s00018-011-0806-3.

[173] Y. Gu and C. Gu, 'Physiological and pathological functions of mechanosensitive ion channels', *Mol Neurobiol*, vol. 50, no. 2, pp. 339–347, Oct. 2014, doi: 10.1007/s12035-014-8654-4.

[174] J. K. Kirklin *et al.*, 'Eighth annual INTERMACS report: Special focus on framing the impact of adverse events', *The Journal of Heart and Lung Transplantation*, vol. 36, no. 10, pp. 1080–1086, Oct. 2017, doi: 10.1016/j.healun.2017.07.005.

[175] C. R. Bartoli, D. J. Restle, D. M. Zhang, M. A. Acker, and P. Atluri, 'Pathologic von Willebrand factor degradation with a left ventricular assist device occurs via two distinct mechanisms: Mechanical demolition and enzymatic cleavage', *The Journal of Thoracic and Cardiovascular Surgery*, vol. 149, no. 1, pp. 281–289, Jan. 2015, doi: 10.1016/j.jtcvs.2014.09.031.

[176] A. Blaeser, D. F. Duarte Campos, U. Puster, W. Richtering, M. M. Stevens, and H. Fischer, 'Controlling Shear Stress in 3D Bioprinting is a Key Factor to Balance Printing Resolution and Stem Cell Integrity', *Adv Healthcare Materials*, vol. 5, no. 3, pp. 326–333, Feb. 2016, doi: 10.1002/adhm.201500677.

[177] B. Coste *et al.*, 'Piezo1 and Piezo2 Are Essential Components of Distinct Mechanically Activated Cation Channels', *Science*, vol. 330, no. 6000, pp. 55–60, Oct. 2010, doi: 10.1126/science.1193270.

[178] S. S. Ranade *et al.*, 'Piezo1, a mechanically activated ion channel, is required for vascular development in mice', *Proc. Natl. Acad. Sci. U.S.A.*, vol. 111, no. 28, pp. 10347–10352, Jul. 2014, doi: 10.1073/pnas.1409233111.

[179] K. Saotome, S. E. Murthy, J. M. Kefauver, T. Whitwam, A. Patapoutian, and A. B. Ward, 'Structure of the mechanically activated ion channel Piezo1', *Nature*, vol. 554, no. 7693, pp. 481–486, Feb. 2018, doi: 10.1038/nature25453.

[180] R. Syeda *et al.*, 'Piezo1 Channels Are Inherently Mechanosensitive', *Cell Reports*, vol. 17, no. 7, pp. 1739–1746, Nov. 2016, doi: 10.1016/j.celrep.2016.10.033.

[181] C. D. Cox *et al.*, 'Removal of the mechanoprotective influence of the cytoskeleton reveals PIEZO1 is gated by bilayer tension', *Nat Commun*, vol. 7, no. 1, p. 10366, Jan. 2016, doi: 10.1038/ncomms10366.

[182] L. O. Romero *et al.*, 'Dietary fatty acids fine-tune Piezo1 mechanical response', *Nat Commun*, vol. 10, no. 1, p. 1200, Mar. 2019, doi: 10.1038/s41467-019-09055-7.

Appendix A: Code for TDMS File Conversion

```
pip install nptdms[hdf,pandas,thermocouple_scaling]
```

```
Collecting nptdms[hdf,pandas,thermocouple_scaling]
  Downloading nptdms-1.10.0.tar.gz (181 kB)
     ━━━━━━━━━━━━━━━━━━━━━━━━━━━━━━━━━━━━━━━━ 181.5/181.5 kB 6.8 MB/s eta 0:00:00
  Installing build dependencies ... done
  Getting requirements to build wheel ... done
  Preparing metadata (pyproject.toml) ... done
Requirement already satisfied: numpy in /usr/local/lib/python3.11/dist-packages (from
Requirement already satisfied: pandas in /usr/local/lib/python3.11/dist-packages (fro
Requirement already satisfied: pyarrow in /usr/local/lib/python3.11/dist-packages (fr
Requirement already satisfied: h5py>=2.10.0 in /usr/local/lib/python3.11/dist-package
Requirement already satisfied: python-dateutil>=2.8.2 in /usr/local/lib/python3.11/di
Requirement already satisfied: pytz>=2020.1 in /usr/local/lib/python3.11/dist-package
Requirement already satisfied: tzdata>=2022.7 in /usr/local/lib/python3.11/dist-packa
Requirement already satisfied: six>=1.5 in /usr/local/lib/python3.11/dist-packages (f
Building wheels for collected packages: nptdms
  Building wheel for nptdms (pyproject.toml) ... done
  Created wheel for nptdms: filename=nptdms-1.10.0-py3-none-any.whl size=108457 sha25
  Stored in directory: /root/.cache/pip/wheels/1b/4b/17/21e8b03b37ea51ce7ec9f5570cdf0
Successfully built nptdms
Installing collected packages: nptdms
Successfully installed nptdms-1.10.0
```

```
from google.colab import drive
drive.mount('/content/gdrive')
```

```
Mounted at /content/gdrive
```

```
import os
import struct
from nptdms import TdmsFile
import numpy as np

def get_tdms_filepaths(rootdir=None, recursive=False):
    tdms_filepaths = []
    for dirpath, dirnames, filenames in os.walk(rootdir):
        tdms_filepaths.extend([
            os.path.join(dirpath, filename)
            for filename in filenames
            if (filename.endswith(".tdms"))
        ])
    if recursive == True:
        for dirname in dirnames:
            tdms_filepaths.extend(get_tdms_filepaths(os.path.join(rootdir, dirnam
    return tdms_filepaths

def print_experiment_notes(tdms_filename):
    print(f"Notes of file '{tdms_filename}':")
    with TdmsFile.open(tdms_filename) as tdms_file:
        notes = tdms_file.properties["Notes"]
        print(f"{notes}")
```

```
def print_tdms_info(tdms_filename, verbose=False):
    print("{:s}".format(tdms_filename))
    if verbose:
        with TdmsFile.open(tdms_filename) as tdms_file:
            for group in tdms_file.groups():
                print(f"  {group.name}:")
                for key, value in group.properties.items():
                    print(f"      {key}: {value}")
                for channel in group.channels():
                    print(f"    {channel.name}:")
                    for key, value in channel.properties.items():
                        print(f"      {key}: {value}")

def get_roi_ids(tdms_filename, groupname=None):
        groupname = 'Tracking Data' if groupname is None else groupname

        with TdmsFile.open(tdms_filename) as tdms_file:
            group = tdms_file[groupname]
            channels = group.channels()

        roi_ids = [
            channel.properties['ROI ID']
            for channel in channels
            if 'Microsphere Center X' in channel.name
        ]

        return roi_ids

def get_tfa(tdms_filename, groupname=None):
    groupname = 'Tracking Data' if groupname is None else groupname

    with TdmsFile.open(tdms_filename) as tdms_file:
        group = tdms_file['Tracking Data']

        time = group['Time (s)'][:]
        time = (time - time[0]) * 1e3  # ms
        frequency = group['Frequency (MHz)'][:]
        power = group['Power (%)'][:]
        amplitude = np.sqrt(power * 100)

    tfa = {
        'time': time,
        'frequency': frequency,
        'amplitude': amplitude
    }
    r  e  t  u  r  n    t  f  a

def create_roi_data_array(tdms_filename, roi_id, tfa, groupname=None):
    """
    Create a data array, which is compatible with the old AFS analysis
    software.

    Create the data array consists of the following steps:
    - correct for time offset (property start_time_s)
    - Convert Power (%) into Amplitude (%): sqrt(P x 100) "Convert Power to Volta
```

```
    - fill minLUT with NaN values, as these are not used anywhere
    - assemble ['Time (s)', 'X (nm)', 'Y (nm)', 'Z (nm)', 'Frequency (MHz)', 'Pow

    Parameters --------
    --  tdms_filename  :
    str
        The filename of the TDMS file with the data.
    roi_id : int
        The ROI ID.
    tfa : dict
        A dict with time, frequency, and amplitude.
    groupname : str
        The name of the group to get the data from.

    Returns ------- np.array with columns Time (ms), x (nm),
    y (nm), z (nm),

        Filling (NaN), Frequenzy (MHz), Amplitude (%), Filling (NaN)
    """
    groupname = 'Tracking Data' if groupname is None else groupname

    with TdmsFile.open(tdms_filename) as tdms_file:
        group = tdms_file[groupname]

        x = group[f'ROI {roi_id:04d} Microsphere Center X (m)'][:] * 1e9 y# nm
        = group[f'ROI {roi_id:04d} Microsphere Center Y (m)'][:] * 1e9 z =
        group[f'ROI {roi_id:04d} Microsphere Center Z (m)'][:] * 1e9

        start = group[f'ROI {roi_id:04d} Microsphere Center X (m)'].properties['S

    size = x.size
    stop = start + size

    t  =  tfa['time'][start:stop]  f  =
    tfa['frequency'][start:stop]  a  =
    tfa['amplitude'][start:stop]
    nan = np.full(size, np.nan)  # minLUT & last row

    roi_data = np.vstack([t, x, y, z, nan, f, a, nan]).T

    return roi_data

def write_binary_data(filename, array, dtype='d', endianness='<'):
    fmt = endianness + dtype * array.size
    data = struct.pack(fmt, *array.flatten())

    with open(filename, 'wb') as f:
        f.write(data)

def convert_afs_data(tdms_filename, dirname=None):
    dirname = os.path.splitext(tdms_filename)[0] if dirname is None else dirname
    try:
        os.makedirs(dirname)
    except FileExistsError:
        print(f'Folder {dirname} does already exist. Conversion canceled.')
```

```
    else:
        # Conversion can proceed
        print_tdms_info(tdms_filename, verbose=False)

        # Get global Time (ms), Frequency (MHz), and Amplitude (%)
        tfa = get_tfa(tdms_filename, groupname=groupname)

        # Get all ROI IDs that have data in the TDMS file
        roi_ids = get_roi_ids(tdms_filename, groupname=groupname)

        # Get the data of all ROI IDs and write binary file
        for roi_id in roi_ids:
            data = create_roi_data_array(tdms_filename, roi_id, tfa, groupname=gr
            data_filename = os.path.join(dirname, f'data_#001_#{roi_id:02d}txyz')
            write_binary_data(data_filename,  data,  dtype='d',  endianness='<')
            print("Converted {group_name:s} of ROI ID {roi_id:04d} with size {siz
        print()


rootdir = '/content/gdrive/MyDrive/AFSData'
tdms_filenames = get_tdms_filepaths(rootdir=rootdir, recursive=True)
groupname = 'Tracking Data'

for tdms_filename in tdms_filenames:
    convert_afs_data(tdms_filename)
```

```
Folder /content/gdrive/MyDrive/AFSData/20240312-160628 does already exist. Conversion
Folder /content/gdrive/MyDrive/AFSData/20240315-120209 does already exist. Conversion
Folder /content/gdrive/MyDrive/AFSData/20240315-145809 does already exist. Conversion
/content/gdrive/MyDrive/AFSData/20250318-111235.tdms
Converted Tracking Data of ROI ID 0001 with size 9828
Converted Tracking Data of ROI ID 0002 with size 9828
Converted Tracking Data of ROI ID 0003 with size 9828
Converted Tracking Data of ROI ID 0004 with size 9828
Converted Tracking Data of ROI ID 0005 with size 9828
Converted Tracking Data of ROI ID 0006 with size 9828
Converted Tracking Data of ROI ID 0007 with size 9828
Converted Tracking Data of ROI ID 0008 with size 9828
Converted Tracking Data of ROI ID 0009 with size 9828
Converted Tracking Data of ROI ID 0010 with size 9828
Converted Tracking Data of ROI ID 0011 with size 9828
Converted Tracking Data of ROI ID 0012 with size 9828
Converted Tracking Data of ROI ID 0013 with size 9828
Converted Tracking Data of ROI ID 0014 with size 9828
Converted Tracking Data of ROI ID 0015 with size 9828
Converted Tracking Data of ROI ID 0016 with size 9828
Converted Tracking Data of ROI ID 0017 with size 9828
Converted Tracking Data of ROI ID 0018 with size 9828
Converted Tracking Data of ROI ID 0019 with size 9828
Converted Tracking Data of ROI ID 0020 with size 9828
Converted Tracking Data of ROI ID 0021 with size 9828
Converted Tracking Data of ROI ID 0022 with size 9828
Converted Tracking Data of ROI ID 0023 with size 9828
Converted Tracking Data of ROI ID 0024 with size 9828
```

```
tdms_filename    "/content/gdrive/MyDrive/AFSData/20250318111235.tdms"

print_experiment_notes(tdms_filename)
```

```
Notes of file '/content/gdrive/MyDrive/AFSData/20250318-111235.tdms':
```

Appendix B: Experimental Standard Operational Procedures (SOPs)

---

z-Movi Chip Handling SOP

Chip Glass Surface Coating with Poly-L-Lysine (PLL):

1. Clean the chip and dry for **1 hour at 37°C** in a dry incubator.
2. Prepare a **0.002% PLL** solution in PBS.
3. Pull **100 µL of fresh PLL solution** into the microfluidic channel using a **3 mL syringe**.
    - Leave ~10 µL in the reservoir to avoid bubble formation.
4. Incubate the PLL in the chip at **room temperature for 10 minutes**.
5. Introduce **400 µL of PBS** into the flow cell **three times**.
6. If using the chip **the same day**:
    - Pull out remaining PBS via syringe.
    - Pull air through the chip **several times**.
    - Incubate at **37°C with reservoir capped** for at least 1 hour.
7. If using the chip **within 72 hours**:
    - Leave PBS in the channel and cap the reservoir.
8. Use PLL-coated chips **within 3 days** of coating.
9. Before cell seeding:
    - Rehydrate the chip with **100 µL of warm PBS**, leaving ~10 µL in the reservoir.
    - Repeat with **100 µL of warm complete culture medium**

Chip Glass Surface Coating with Fibronectin (FN):

1. Clean and dry the chip for **1 hour at 37°C** in a dry incubator.
2. Using a **3 mL syringe**, rehydrate the glass surface with:
    - **200 µL of 1M NaOH** (5 min incubation).
    - **400 µL of Milli-Q water** (twice).
    - **200 µL of 1M HCl** (twice; second time incubate for 2 min).
    - **400 µL of Milli-Q water** (three times).

- **400 µL of PBS** (once).

3. Prepare **30 µL of 50 µg/mL FN solution** in PBS (1:20 dilution from 1 mg/mL stock).
4. Pull FN solution into channel with ~10 µL remaining in reservoir.
5. Wash inlet with **200 µL of PBS** (three times), then reload with **200 µL of PBS**.
6. Cap and store chips in dry incubator **overnight at 37°C**.
7. Use FN-coated chips **within 3 days**.
8. Before cell seeding:
   - Wash chip **three times with 400 µL of PBS**.
   - Introduce **400 µL of complete culture medium** into flow cell.

Target Cell Monolayer Formation:

1. Accept chips with **≥80% confluency**.
2. Wash adherent cells with **3–5 mL of PBS**.
3. Trypsinize with **200–500 µL TrypLE** for 3 min at **37°C**.
   - Volume depends on flask size (T25 vs T75).
4. Collect cells in **5 mL of complete medium**.
5. Determine cell density:
   - Dilute **10 µL stock + 90 µL PBS**.
   - Use automatic cell counter.
6. For each chip:
   - Seed **20 µL of MCF-7 or A2780 cells** at optimal density via syringe.
   - Leave ~10 µL in reservoir to avoid bubbles.
   - Maintain **37°C** throughout seeding.
7. Clean inlet with **400 µL complete medium** (three times).
8. Reload inlet with **200 µL of complete medium**.
9. Cap and incubate chips at **37°C for 1–4 hours**, depending on cell line.

Cell Viability Measurement of Target Cell Monolayer:

1. Dilute **10 µL Trypan Blue** in **50 µL complete medium**.
2. Flush dilution into the reservoir.
3. Incubate cells with dye for **30 seconds**.

4. Wash out with **200 µL complete medium**.
5. Assess viability using **brightfield imaging**.
    - Confirm monolayer is moderately healthy.
    - If fully stained, the majority of cells are dead.

Effector Cell Staining:

1. Rinse adherent cells with **3–5 mL PBS**.
2. Trypsinize with **200–500 µL TrypLE** for 3 min at **37°C**.
3. Wash cells into suspension using **5 mL complete medium**.
4. Count cell density:
    - Dilute stock 1:20 in PBS (100 µL sample).
5. For each run:
    - Prepare **20 µL of 15×10^6 cells/mL** (0.3×10^6 total).
6. Perform wash step:
    - Buffer/medium exchange.
    - Centrifuge at **1000 rpm for 4 min**.
7. Wash cells with **5 mL PBS**.
8. Stain cells:
    - Use **1×CellTrace Far Red Dye** in **2 mL PBS at 1×10^6 cells/mL**.
    - Incubate for **15 min in dark**.
    - Re-suspend every 5 min by pipetting.
9. Inhibit staining:
    - Add **5 mL complete medium**.
10. Final wash with **5 mL PBS**.
11. Re-suspend in medium to **15×10^6 cells/mL**.
12. Transfer to a **round-bottom 96-well plate**.

Effector Beads Coating with Fibronectin (FN):

1. Wash step:
    - Buffer/medium exchange.
    - Centrifuge at **1000 rpm for 4 min**.
2. Wash beads **three times** with **500 µL PBS**.

3. Wash once with **500 µL complete medium**.
4. Incubate beads:
    - Coat with **10 µg/mL FN** in **200 µL complete medium**.
    - Rotate at room temp for **1 hour**.
5. Wash beads **three times** with **500 µL complete medium**.
6. Re-suspend in medium at required volume.
7. Use at least **10 µL of Effector bead solution** per run.

Chip Cleaning:

1. Introduce **5% bleach** (A1727, Sigma-Aldrich) into the microfluidic channel.
2. Incubate for **10 min–4 hrs at room temperature**.
3. Rinse channel **twice with 400 µL Milli-Q water**, using air bubbles to scrub glass surface.
4. Scrub surface **twice with 200 µL of 5% bleach**.
5. Sequentially pull through:
    - **400 µL of 5% bleach**
    - **400 µL Milli-Q water (two rounds)**
    - **200 µL of 12M HCl (two rounds)** (H1758, Sigma-Aldrich)
    - **400 µL Milli-Q water (two rounds)**
    - **400 µL of 1M NaOH**
6. Rinse with **400 µL of 1M NaOH**, scrub with air bubbles.
7. Incubate with **200 µL of 1M NaOH for up to 1 hour** to reset glass surface.
8. Scrub again with **200 µL of 1M NaOH**.
9. Final rinse with **400 µL Milli-Q water (twice)**.
10. Using a **10 mL syringe**, remove residual liquid by pulling through air several times.
11. Store cleaned chips in dry incubator at **37°C**.

z-Movi Experimental SOP

Cell Binding Avidity Measurement:

1. Place the chip on the **z-Movi stage**.
2. Validate monolayer quality using an **acoustic force of 1000 pN for 10 seconds**.
3. Level cell culture medium in the inlet to **~10 µL**.
4. Add **20 µL stained effector cell solution** into the reservoir and pull into the microfluidic channel.
5. Incubate cells with the target monolayer for a designated period.
6. Wash inlet and reservoir **three times with 200 µL complete medium**.
7. Reload inlet with **100 µL complete medium**.
8. Apply a **linear acoustic force ramp of 0–1000 pN over 2.5 minutes**.
9. Determine **percentage of bound cells** during force ramp for statistical analysis.
10. To inhibit FN binding:
    - Treat tumour cells with **FN antibody (MA5-11981, Thermo Fisher)**.
11. To eliminate non-specific binding:
    - Use **2% BSA (A3311, Sigma-Aldrich)** diluted in complete medium.

Avidity Data Analysis:

1. Analyse data offline using **Oceon 1.4.1 software** (LUMICKS).
2. Upload two-channel images:
    - **Brightfield** (monolayer + effector events)
    - **Fluorescence** (effector location and detachment)
3. Software automatically directs **field of view (FOV)** based on chip calibration.
4. Within FOV:
    - Track **monolayer via brightfield**
    - Track **effectors via fluorescence**
5. System designates each effector's **region of interest (ROI)**:
    - **12 pixel-wide circle** using cell centre.
6. Detect ~**400 ROIs** per FOV:
    - Detached effectors = events that left ROIs.
7. **Automatic tracking**, then **manual selection** to validate:

    - Exclude: clumped effectors, covered nodes, adherent to coatings or monolayer clumps.
    - Include: **hinged effectors** (partial escape but still attached).
8. Simulate tracking of lifted cells across **0–1000 pN force ramp**.
9. Note: manual selection impacts the avidity curve.
    - Omission leads to substantial differences.
    - **Consistent manual selection is essential** for reliable experimental comparison.

Acoustic Force Spectroscopy (AFS) Experimental SOP

Initial Hardware Setup:

1. Turn on the **Acoustic Force Field Generator.**
2. Turn on the **Nikon Inverted microscope**.
3. Select the **LEFT camera port** on the microscope.
4. Toggle the z-position to approximately **8500 µm** on the microscope.
5. Toggle the Nikon Collimation Adaptor to **MAX**.
6. Secure z-Movi Chip on to the chip holder.

Launch AFS Software:

1. Initiate the AFS software.
2. Set the temperature feedback to **37˚C**.
3. Set the ***Power Percentage*** to **0 %**.
4. Set the ***Frequency*** to **7.970 MHz**.
5. Turn on the ***Signal Generator***.

Particle Imaging Setup:

1. Adjust the ***Region of Interest (ROI)*** from 50 to **75**.
2. Attune the ***Focal Plane Position*** to **3**.

Power Sequence Configuration:

1. Input the desired power in the ***power*** **column**.

2. Input the desired force duration respective to the power in the ***wait* column**.
3. Drag each transition into the ***sequence of power transitions* column**.
4. Drag the sequence to the ***command* column**.
5. Initiate the desired power sequence by clicking ***Execute Commands***.

Frequency Calibration:

1. Initiate ***frequency sweep*** at the beginning of the force application.
2. Set the **resonant frequency** determined by the frequency sweep.

Particle Tracking:

1. Seed particles into the z-Movi chip.
2. Select particles to begin the tracking in the **x-, y- and z-position**.